HARVARD UNIVERSITY
Graduate School of Arts and Sciences

DISSERTATION ACCEPTANCE CERTIFICATE

The undersigned, appointed by the

Department of Physics

have examined a dissertation entitled

Quantum Dots for Conventional and Topological Qubits

presented by Andrew Higginbotham

candidate for the degree of Doctor of Philosophy and hereby certify that it is worthy of acceptance.

Signature _____

Typed name: Professor Robert Westervelt, Chair

Signature _____

Typed name: Professor Charles Marcus (Niels Bohr Institute), Co-Chair

Signature _____

Typed name: Professor Amir Yacoby

Date: September 4, 2015

Quantum Dots for Conventional and Topological Qubits

A DISSERTATION PRESENTED
BY
ANDREW HIGGINBOTHAM
TO
THE DEPARTMENT OF PHYSICS

IN PARTIAL FULFILLMENT OF THE REQUIREMENTS
FOR THE DEGREE OF
DOCTOR OF PHILOSOPHY
IN THE SUBJECT OF
PHYSICS

HARVARD UNIVERSITY
CAMBRIDGE, MASSACHUSETTS

SEPTEMBER 2015

Professor Charles M. Marcus
Professor Robert M. Westervelt

Andrew Higginbotham

Quantum Dots for Conventional and Topological Qubits

Abstract

This thesis presents a series of quantum dot studies, performed with an eye towards improved conventional and topological qubits. Chapters 1-3 focus on improved conventional (spin) qubits; Chapters 4-6 focus on the topological Majorana qubits.

Chapter 1 presents the first investigation of Coulomb peak height distributions in a spin-orbit coupled quantum dot, realized in a Ge/Si nanowire. Strong spin-orbit coupling in this hole-gas system leads to antilocalization of Coulomb blockade peaks, consistent with theory. In particular, the peak height distribution has its maximum away from zero at zero magnetic field, with an average that decreases with increasing field. Magnetoconductance in the open-wire regime places a bound on the spin-orbit length ($l_{so} < 20$ nm), consistent with values extracted in the Coulomb blockade regime ($l_{so} < 25$ nm).

Chapters 2 & 3 demonstrate operation ofimproved spin qubits. Chapter 2 continues the investigation of Ge/Si nanowires, demonstrating a qubit with tenfold-improved dephasing time compared to the standard GaAs case. The combination oflong dephasing time and strong spin-orbit coupling suggests that Ge/Si nanowires are promising for a spin-orbit qubit. In Chap. 3, multi-electron spin qubits are operated in GaAs, and improved resilience to charge noise is found compared to the single-electron case.

Chapters 4 & 5, present a series of studies on composite superconductor/semiconductor Al/InAs quantum dots. Detailed study of transport cycles and Coulomb blockade peak spacings in zero magnetic field are presented in Chap. 4, and the parity lifetime of a bound state in the nanowire is inferred to exceed 10 milliseconds. Next, in Chap. 5, finite magnetic field behavior is investigated while varying quantum dot length. Coulomb peak spacings are consistent with the emergence of Majorana modes in the quantum dot. The robustness of Majorana modes to magnetic-field perturbations is measured, and is found to be exponential with increasing nanowire length. Coulomb peak heights are also investigated, and show signatures of electron teleportation by Majorana fermions.

Finally, Chap. 6 outlines some schemes to create topological Majorana qubits. Using experimental techniques similar to those in Chap.'s 2 & 3, it may be possible to demonstrate Majorana initialization, readout, and fusion rules.

Contents

0 Introduction 1

0.1 Qubit considerations . . . 2
0.2 Coulomb blockade basics . . . 4

1 Antilocalization in Coulomb blockade 7

1.1 Introduction . . . 7
1.2 Theory of Coulomb blockade peak heights with spin-orbit coupling . . . 9
1.3 Experiment parameters . . . 11
1.4 Coulomb blockade measurements . . . 13
1.5 Open regime measurement . . . 15
1.6 Discussion . . . 20

2 Hole dephasing in a Ge/Si nanowire 21

2.1 Introduction . . . 21
2.2 Theoretical expectation for T_2^* . . . 22
2.3 Setup and charge readout . . . 23
2.4 Spin readout . . . 25
2.5 Spin relaxation . . . 27
2.6 Spin dephasing . . . 30
2.7 Discussion . . . 32

3 Multi-electron spin qubit in GaAs 33

3.1 Introduction . . . 33
3.2 Setup and Operation . . . 35
3.3 Noise analysis . . . 37
3.4 Full decoherence model and parameters . . . 42
3.5 Dephasing in the small-J limit . . . 45
3.6 Justification of Gaussian envelopes . . . 46
3.7 Multi-electron operation in a second device . . . 48
3.8 Charge sensing and single-shot readout of a multi-electron singlet-triplet qubit . . . 49
3.9 Measurement of $T_{2,\mathrm{n}}^*$ for (1,1) and (7,5) dot occupations . . . 51
3.10 Conclusion . . . 52

4 Quasiparticles in an Al-InAs quantum dot 53
4.1 Introduction . . . 53
4.2 Experimental Setup . . . 54
4.3 Coulomb blockade . . . 56
4.4 Zero-bias data . . . 61
4.5 Number of quasiparticles . . . 64

5 Majorana quantum dot 67
5.1 Introduction . . . 67
5.2 Experiment . . . 68
5.3 Discusion . . . 74

6 Majorana fusion rules proposal 75
6.1 Fusion rule setup . . . 76
6.2 Discussion . . . 78

Appendix A Thermodynamics of even-odd effect 80
A.1 General thermodynamics . . . 80
A.2 Number of quasiparticles . . . 82

Appendix B Approximations in Chapter 4 85
B.1 Comparison of free energy approximations . . . 85
B.2 Effect of the bound state on the free energy . . . 86
B.3 Comparison of thermodynamic and rate models . . . 87

References 99

List of figures

1 General quantum dots energetics 5

1.1 Antilocalization device overview 12
1.2 Coulomb peak height decreasing in magnetic field 14
1.3 Gate perturbation the quantum dot 15
1.4 Coulomb peak distribution 16
1.5 Antilocalization in the open regime 17
1.6 Example open-regime fits 19

2.1 Ge/Si double quantum dot device 24
2.2 Spin readout using Pauli blockade 26
2.3 Reversed T_1 pulse sequence 27
2.4 Spin relaxation 28
2.5 Spin dephasing 30

3.1 Multi-electron device overview 36
3.2 Exchange profiles for different charge states 38
3.3 Extracting detuning-equivalent noise 40
3.5 Small-exchange behavior of Rabi pulse sequence 46
3.6 Justification of Gaussian envelope 47
3.7 Operation of second device 48
3.8 Single-shot readout of multi-electron qubit 50
3.9 Nuclear-noise dephasing of multi-electron qubit 52

4.1 Al-InAs quantum dot 55
4.2 Al-InAs Coulomb diamonds 56
4.3 Subgap state bias spectroscopy, experiment and model 57
4.4 Interpreting conductance thresholds 59
4.5 Effect of quasiparticle relaxation 60
4.6 Single quasiparticle relaxation bound 60
4.7 Even-odd Coulomb peak spacings 61
4.8 Temperature and magnetic field dependence of the even-odd peak spacings 65

5.1 Long Al-InAs quantum dot 68

5.2 Splitting Coulomb peak in $L = 0.9$ μm device 69
5.3 Critical field of $L = 0.9$ μm device 70
5.4 Critical field of $L = 0.9$ μm device 71
5.5 Exponential dependence of oscillation amplitude on length 72
5.6 Supression of Coulomb peak heights for $B^* < B < B^{**}$ 73
5.7 Excitation gap in $1e$ Coulomb diamonds for $L = 1.5$ μm 74

6.1 Single-dot parity qubit 76
6.2 Double-dot parity qubit 78

B.1 Comparison of free energy approximations 86
B.2 Effect of bound state on free energy 87
B.3 Even-odd peak spacings compared with rate model 88

Acknowledgments

This PhD was a wild ride, and one of the few constants was being surrounded by amazing people. To everyone who helped me get through this process: thank you.

First, I want to thank my advisor, Prof. Charlie Marcus, for making this experience possible. Both at Harvard and in Copenhagen, Charlie worked tirelessly to make the lab an easy place to do research, constantly searching for and removing bottlenecks along the way. Working in Charlie's lab is about doing all things — big and small — the right way. That includes the nitty gritty of lab organization: labeled drawers (clear label, white text, BIG font, please), sorted tools, electronics on wheels, and clean desks. It also includes experimental techniques, like minimizing noise and optimizing data acquisition time. Most importantly, it includes thinking like a true experimentalist. Charlie taught me that data can't be wrong, and the power of qualitative, empirical observations. The attitude he imparted changed the way that I approach problems, and made me a better, more productive scientist.

I'd also like to thank my defense committee, Prof. Amir Yacoby and Prof. Bob Westervelt for forming the rest of my defense/qualifying committees. Bob also graciously agreed to be my on-campus advisor at a point when we had hardly, if ever, met.

I owe additional thanks to Prof. Amir Yacoby, as well as Prof. Raffi Budakian, whose advice on picking problems, being creative, and finding time to be *in*efficient were very influential when I was trying to synthesize the research from my PhD, and figure out how to take the next steps.

To the Boston guys, Rishabh, Vikram, and Toby: thanks for being my only connection to reality the first few years of my PhD.

From the old lab, I thank Patrick Herring for patiently getting me through the first rounds of nanofab, Hugh Churchill many questions answered and general wisdom, Jim Medford for being an inspiringly productive, yet possibly insane, coworker, Maja Cassidy for keeping the lab from falling apart, and Dough McClure for not getting annoyed when I played Nintendo at my desk.

From the new lab, I thank Thorvald Larsen for quickly becoming such a great scientist and friend, Mattias Fitzpatrick for outstanding bro-ness, as well as physics skill, Giulio Ungaretti for generating constant, hilarious, disagreements and food/drink education, Henri Suominen for good times hanging out, and for programming that giant red button I so desparately needed, Morten Madsen for being explomatic, Sven Albrecht for being a great collaborator and for reminding me that its possible to have fun in lab. I thanks Karsten Flensberg, Gediminas, Kirsanskas, and Jason Alicea for many productive yet stress-free physics discussions. I also thank Mark Rudner for the occasional physics discussion, the more frequent 90s pop culture reference, and lots of good times hanging out.

The lead up and aftermath of moving from Boston to Copenhagen was hard, and I don't think I could

have made it through without the support ofthe some very special people. First, I thank my family for phone calls, visits, and support during the hard times. Willy Chang, thanks for becoming my friend in Boston, and all the good times we spent hanging out, complaining, and occasionally enjoying the first few years in Copenhagen. Angela Kou, thanks for teaching me a lot of physics, lots offun conversation in the office, and keeping the Boston crew alive and active with constant food adventures, especially that last summer in Boston. Mikey Shulman, thanks for sharing your infectuous enthusiasm, but not your other infectous attributes, your positive vibes, and for convincing me to go for a workout even when I really don't feel like it. Herr Professor Ferdinand Kuemmeth who trained me to be a physicist, and shared this crazy adventure with me from start to end, thanks for being an amazing friend and mentor. Johannes Beil, thanks for being a rock of sanity during the dark days, and for many interesting, hilarious, and inspiring discussions in the office. Morten Kjærgaard, thanks for helping me make it in Copenhagen, and for being an example of how to live right.

Finally, I thank Marina Hesselberg for sharing these last few happy years with me, and for many more to come.

0 Introduction

Quantum dots have been explored in a wide range of materials, such as GaAs and Si 2DEGs[1, 2], graphene [3], nanotubes [4], and nanowires [5]. Understanding and controlling the rich physics of quantum dots has allowed qubits to be created in many of these materials [6–10].

The work contained herein follows the trend of materials exploration and qubit development, reporting the characterization of quantum dots in new materials and the realization of new qubits. Two qubit approaches are explored: conventional and topological. The work on conventional qubits focuses on improving operation in spin qubits by finding systems with large spin-orbit coupling (Chap. 1), weak nuclear dephasing (Chap. 2), and improved resilience to electrical noise (Chap. 3). The work on topological qubits focuses on Majorana modes at the ends of superconductor/semiconductor nanowires. The topological qubit lifetime, set by quasiparticle poisoning, is bounded in Chap. 4. Chapter 5 experimentally demonstrates exponential robustness of the Majorana modes. Chapter 6 outlines a proposal for experimentally testing nontrivial Majorana fusion rules.

0.1 Qubit considerations

A qubit is a controlled, quantum mechanical two-level system. The two level system can be natural, such as a single spin, or a part of a larger Hilbert space, as for S/T_0 spin qubits and superconducting qubits. Qubits are interesting because, if properly controlled, they are a resource for computation that exceeds classical limits. Even as the general computing power of qubits is still being explored in theory, the identification of a few quantum "killer apps" — in areas such as cryptography and chemistry — has motivated experimental effort to develop practical technology.

0.1.1 Conventional qubits

A wide range of qubit architectures are currently being explored, such as trapped ions, superconducting, and spin qubits. Qubit operations in these systems are generally diabatic, meaning the Hamiltonian is changed quickly to control dynamical phases acquired by the qubit. As a concrete example of diabatic control, consider a single spin aligned with an external magnetic field in the z-direction. Diabatically changing the field to the x-direction causes the spin to precess. Alternatively, one can apply a drive field, diabatic with respect to the qubit splitting ($B_x \cos(\omega t)$, $\omega \approx B_z$) to induce Rabi oscillations, as is commonly performed in trapped ion and superconducting qubits. Coupling between qubits is also required for computation, which is not discussed here.

In addition to the intentional control fields (e.g. B_x), inevitably there are uncontrolled fields, $\delta\vec{B}$. The uncontrolled field causes dephasing, which is the central problem of qubit development. There is no general route to mitigate dephasing; work must proceed separately on each qubit architecture. However, once certain dephasing thresholds are reached, there are proposed, general methods for constructing improved logical qubits from collections of individual faulty ones [11, 12].

Chapters 1-3 present work to improve coherence in conventional (spin) qubits. Spin qubits in Ge/Si nanowires are appealing because their strong spin-orbit coupling, which is investigated in Chap. 1, might facilitate fast manipulation, and because the uncontrolled hyperfine interaction is weak, as shown in Chap. 2. Chapter 3 shifts to the traditional GaAs spin qubit system, and shows that the collective spin state of many electrons has improved electric-field dephasing properties compared to the single electron case.

0.1.2 Topological qubits

Topological qubits represent an entirely different approach to overcoming the decoherence problem. Whereas conventional qubits rely on diabatic operation to control dynamical phases, topological qubits rely on adiabatic braiding operations to control topological phases. Qubits are encoded into quasiparticle occupation numbers of non-Abelian anyons, which have several special properties [13]. First, the N-quasiparticle ground state is degenerate, which is an essential requirement for cyclic evolution to result in non-Abelian rotations [14]. Second, the unitary transformation resulting from braiding depends only on the topology of the braid. This distinguishes the topological system from non-topological systems with degenerate ground states, which can conceivably exhibit arbitrary non-Abelian, geometric phases [14]. Finally, the degeneracy of the anyons must be robust, meaning that it is insensitive to small perturbations.

Majorana modes are a useful example of this paradigm, and are particularly interesting because of possibilities for experimental realization [15–18]. For concreteness, consider a superconductor hosting four Majorana modes γ_1, γ_2, γ_3, γ_4. Each pair of Majoranas combines to form a zero-energy fermionic state, so there are two fermionic states that can be empty or full — the ground-state is fourfold degenerate . Grouping the Majoranas into pairs (γ_1, γ_2) and (γ_3, γ_4) the degenerate states can be labeled by the superconducting quasiparticle parity $|P_{12}, P_{34}\rangle$; they are are $|00\rangle$, $|10\rangle$, $|01\rangle$, $|11\rangle$. Suppose the system starts out in the state $|\psi\rangle = |00\rangle$. Adiabatically exchanging (braiding) Majoranas 2 and 3 maps the ground state to $|\psi\rangle \to 1/\sqrt{2}(|00\rangle + i\,|11\rangle\,)$ [19]. This operation constitutes a nontrivial rotation within the fixed-total-parity degenerate subspace. Specifically, the braid gives a $\pi/2$ rotation about the x-axis on a Bloch sphere with $|00\rangle$ and $|11\rangle$ at the poles.

What are the failure modes for the topological qubit? The qubits are encoded in occupation numbers, which are only approximately conserved at finite temperature. In the Majorana example, a quasiparticle located in the superconductor can relax into the Majorana state, changing its parity. This process, referred to as quasiparticle poisoning, is an uncorrectable error on the Majorana qubit [20]. Chapter 4 shows that the characteristic time for poisoning events exceeds 10 ms in a particular Majorana system.

Another potential failure mode of topological qubits is that Majoranas separated by finite L are only approximately degenerate, with energy splitting predicted to scale as $e^{-L/\xi}$. Chapter 5 experimentally measures this exponential dependence.

0.2 Coulomb blockade basics

From an experimental point of view, work in this thesis centers around quantum dots. Many excellent reviews of quantum dot physics are available in the literature [1, 21, 22]. This section introduces the main concepts.

A quantum dot, as referred to in this thesis, is a confined portion of semiconductor with two leads. Work in this thesis is focused on dots in the isolated regime ($g < e^2/h$, conductance g) and in Coulomb blockade ($kT < E_c$, charging energy C) [1, 21]. Due to the large charging energy, the quantum dot has a fixed number of electrons, causing Coulomb blockade of transport. At fine-tuned points, where two charge states are degenerate, Coulomb blockade conductance peaks occur.

0.2.1 Peak spacings

The energy of a quantum dot with N electrons is

$$E(N) = \frac{e^2N^2}{2C} + eNV_g\frac{C_g}{C} + \sum_n \varepsilon_n \tag{1}$$

for gate voltage V_g with capacitance C_g, and total dot capacitance C. The single-particle energies, ε_N, have a typical spacing $\delta = E_F/N$ for a semiconductor quantum dot, and are simply added to the Coulomb term, which is valid for weak interactions [21].

At zero temperature the energy is minimized, so Coulomb peaks occur at degeneracies, $E(N) = E(N+1)$. It is common to add an N-independent term to make $E(N)$ parabolic,

$$\tilde{E}(N) = \frac{e^2}{2C}(N-n)^2 + \sum_n \varepsilon_n = E(N) - n^2 \tag{2}$$

where $n = -C_GV_G$. The additional term does not change results for ground-state occupation, that is, $E(N) = E(N+1)$ iff $\tilde{E}(N) = \tilde{E}(N+1)$.

In the metallic limit, $\varepsilon_n \to 0$, Coulomb peaks are evenly spaced, as shown in Fig. 1a. Finite single-particle energies can make Coulomb peaks irregular; evenly spaced, spin-degenerate levels, for example, result in even-odd peak spacings (Fig. 1b). The presence of superconductivity, which results in parity-

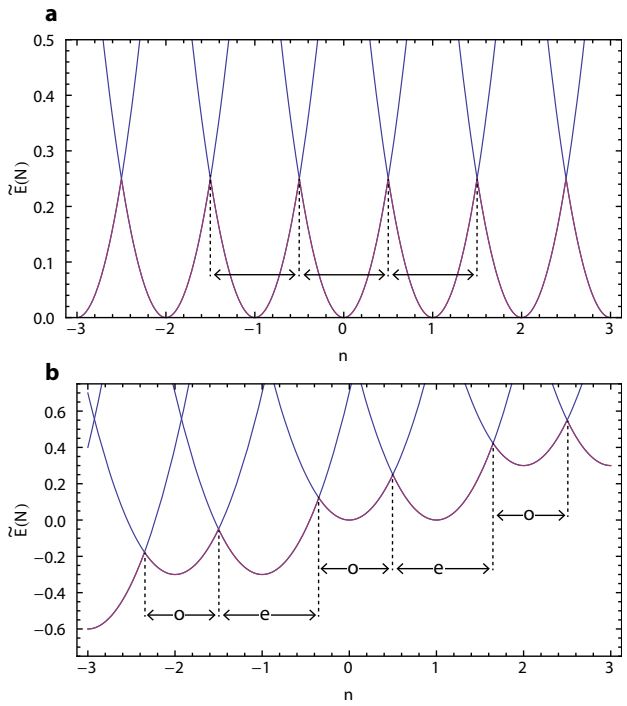

Figure 1: **a**, Parabolic energies $\tilde{E}(N)$ versus gate-charge n, for $N = -3, -2, -1, 0, 1, 2, 3$ for zero level spacing case. Coulomb peak spacings, labeled with arrows, are all the same. **b**, Same as **a**, but with evenly spaced, spin-degenerate levels. Coulomb peak spacings, labeled with arrows, show an even-odd effect.

dependent single-particle energies, can also give even-odd structure, as discussed in Chap. 4.

At finite temperature, the free energy, $F = E - TS$, as opposed to the energy, is minimized. An additional peak shift can then be caused by the entropic contribution to the free energy. For example, the free energy of a spin-degenerate state is lowered by $kT\ln(2)$, shifting Coulomb peaks associated with spin-degenerate levels at finite temperature, which can be verified explicitly by solving rate equations for the Coulomb peaks [22].

Experiments on gate-defined GaAs quantum dots do not show the expected even-odd structure in peak spacing [23], and neither do the Coulomb peaks in Ge/Si nanowires (Chap. 4), naively pointing to the breaking of spin degeneracy at zero field. However, Coulomb peak heights, both in GaAs [24] and Ge/Si (Chap. 4), are, consistent with the presence of spin-rotation symmetry at zero magnetic field. Even-odd peak spacings have been observed for metallic superconductors [25], and for superconductor-semiconductor systems (Chap. 4). Shell filling, closely related to the even-odd effect due to spin, has been observed in circular dots and nanowires in the few-electron regime [5, 26], and nanotubes in the many-electron regime

[4].

0.2.2 Wavefunctions

Electrons inside a quantum dot are subject to the periodic lattice potential, plus a weak, smooth confinement potential from electrostatic gates. The confinement potential, small compared to band gap, is a perturbation on the electrostatics of the crystal. Adding in the confinement perturbation, the electron wavefunctions become a product of the $k = 0$ Bloch wavefunction, u_{n0}, and an envelope function, $F_n(r)$. The envelope function satisfies the Schrödinger equation for a free particle with the effective mass m^* and confinement potential U_{gate}: $(\frac{\hat{p}^2}{2m^*} + U_{\text{gate}}) \cdot F_n(r) = E \cdot F_n(r)$, where energy E is measured from the band edge [21]. Due to the analogy with a free particle, the envelope function is usually referred to simply as the wavefunction, and the presence of the Bloch prefactor is ignored.

In the low-temperature limit, transport occurs through single wavefunction, and Coulomb peak heights give information on wavefunction weight at the leads. This physics is explored in Chap. 1, for a Ge/Si nanowire and Chap. 6 for a superconductor-semiconductor Al/InAs nanowire.

1

Antilocalization in Coulomb blockade

This chapter describes experiments on Ge/Si core/shell-nanowire single quantum dots. The bulk of the chapter was published as Ref. [27], with some extra discussion added to Sec.'s 1.1,1.2 for clarity. The devices were fabricated and measured under the supervision of Charles Marcus, with assistance from Ferdinand Kuemmeth, Thorvald Larsen, and Mattias Fitzpatrick during measurement and manuscript preparation. The nanowires were grown in the group of Charles Lieber by Jun Yao and Hao Yan. Discussions with Igor Aleiner were important for clarifying nuances of the theory.

1.1 Introduction

Antilocalization is a quantum-interference correction to the Drude conductivity, resulting in enhanced conductance at zero magnetic field. It is commonly observed in mesoscopic conductors with strong spin-orbit coupling [28, 29], and has been well studied in low-dimensional systems over the past two decades [30–35]. In quantum wires (1D) and dots (0D), the combination of coherence and spin-orbit coupling is a

topic of renewed interest in part due to numerous quantum information processing proposals—from spin qubits to Majorana modes—where these ingredients play a fundamental role [15, 16, 36, 37]. Antilocalization in 1D systems has been investigated in detail both theoretically [38–40] and experimentally [41–44]. In 0D systems, antilocalization in both the opened and nearly-isolated Coulomb blockade regime has been studied theoretically [45, 46], but to date experiments have only addressed the open-transport regime, where Coulomb effects play a minor role [47, 48].

This chapter summarizes an investigation of full distributions of Coulomb blockade peak height as a function of magnetic field in a gated Ge/Si core/shell nanowire. The hole gas formed in the Ge core of a Ge/Si core/shell nanowire [49] is an attractive system for exploring the coexisting effects of coherence, confinement, and spin-orbit coupling. Tunable quantum dots have been demonstrated in this system [50, 51], and antilocalization has been demonstrated in the open-transport regime [52]. Band structure calculations indicate that Ge/Si nanowires may have extremely strong spin-orbit coupling [53]. 1D confinement, combined with a symmetry-breaking electric field (generically present due to gating and substrate), splits and mixes the heavy hole states, generating a Rashba-like spin-orbit interaction . Since the mixing occurs within the valence subbands, this effect is much stronger than conventional Rashba spin-orbit, which is due to mixing of s and p states at finite k, and is therefore suppressed by the band gap (scaling as $1/\text{gap}^2$) [53].

The principle experimental result in this Chapter is that distribution of Coulomb peak heights reveals the presence of strong spin-orbit coupling, and allows a bounding on the spin-orbit strength consistent with measurements performed in the same wire in the open regime. The zero-field distribution is found to differ markedly from that measured in GaAs quantum dots, where spin-orbit coupling is relatively weak [24], and are consistent with random matrix theory [46] of Coulomb blockade transport through a 0D system with symplectic symmetry (valid for strong spin-orbit coupling). The high-field peak height distribution is found to be a scaled version of the low-field distribution, as expected from theory. However, the observed scale factor, $\sim$ 2.3, is significantly larger than the theoretical factor of 1.4 [46]. Temperature dependence of the peak-height variance is consistent with theory using a value for orbital level spacing measured independently via Coulomb blockade spectroscopy. Consistent bounds on the spin-orbit length, $l_{so} \lesssim 20 - 25$ nm, are found in the Coulomb blockade and open transport regimes.

We first review random matrix theory results that relate peak statistics to wave function symmetries,

then present experimental results for a gated Ge/Si nanowire sample in the Coulomb blockade and open wire regimes.

1.2 Theory of Coulomb blockade peak heights with spin-orbit coupling

Antilocalization in Coulomb blockade, as studied in this chapter, amounts to a change in the distribution of Coulomb peak heights in a quantum dot. Spin-orbit coupling makes wavefunction nodes less likely, resulting in enhanced Coulomb peak heights. As discussed below, this effect comes from general considerations of the symmetries of the quantum dot.

Consider a quantum dot in the deep Coulomb blockade regime, that is, with temperature, voltage bias, and lifetime broadening small compared to charging energy, $kT, V, \Gamma \ll e^2/C$. When, in addition, kT, V, and Γ are less than the orbital level spacing, Δ, tunneling occurs through a single (ground-state) wave function. In this latter case, Coulomb blockade conductance peaks fluctuate in height from peak to peak (*cf.* Fig. 1.1 bottom trace), depending on the coupling of the ground-state wave function to modes in the leads.

In the large-temperature limit, $\Gamma \ll kT$, the Coulomb peak height, g_p, can be found by solving a system of rate equations [45]. The result is

$$g_p = \frac{2e^2}{\hbar}\frac{\chi_s}{kT}\frac{\Gamma_l\Gamma_r}{\Gamma_l+\Gamma_r} = \frac{e^2}{\hbar}\frac{\overline{\Gamma}}{2kT}\chi_s\alpha, \tag{1.1}$$

The factors $\chi_{s=1} = 1/8$ and $\chi_{s=2} = 3-2\sqrt{2}$ arise from the presence ($s=1$) or absence ($s=2$) Kramers degeneracy [22]. The factor $\alpha = 4\Gamma_l\Gamma_r/[\overline{\Gamma}(\Gamma_l+\Gamma_r)]$ with $\Gamma = \Gamma_l+\Gamma_r$, encodes the dependence of peak height on wavefunctions. For a wavefunction ψ inside the quantum dot, the couplings are proportional to norms evaluated at the device leads, $\Gamma_{l,r} \propto |\psi_{l,r}(0)|^2$, so

$$\alpha \propto \frac{|\psi_l|^2|\psi_r|^2}{|\psi_l|^2+|\psi_r|^2} \tag{1.2}$$

For a quantum dot lacking any specially designed spatial symmetries, the classical trajectories are chaotic, and the quantum system is quantum chaotic. The general technique for dealing with quantum chaotic systems, employed both in mesoscopic and nuclear physics, is to assume that the Hamiltonian is made of up

random, independent, Gaussian-distributed elements. It is not *a priori* obvious that such an assumption is valid, although it is known to hold in the specific case of a disordered metallic grain [54]. The implication for wavefunctions is surprisingly simple: each wavefunction degree of freedom is Gaussian distributed [55]. Without spin-orbit coupling and at $B = 0$ wavefunctions are real*, and thus have one degree of freedom; then $|\psi|^2$ is chi-square distributed with one degree of freedom (χ_1^2). Breaking time-reversal symmetry makes wavefunctions complex-valued; then there are two degrees of freedom and $|\psi|^2$ is χ_2^2 distributed. Finally, in the presence of spin-orbit coupling (at any magnetic field) the wavefunction is complex-valued and spin-dependent; then there are four degrees of freedom and $|\psi|^2$ is χ_4^2 distributed. The distribution of $|\psi|^2$ determines the distribution of α, and thus g_p [Eq.'s (1.1-1.2)].

Before giving the explicit formulae for $P(\alpha)$, it is useful to introduce the formal terminology for symmetry classes of disordered and chaotic dots. They are: orthogonal ($\beta = 1$) for time-reversal symmetric systems, unitary ($\beta = 2$) for systems with broken time-reversal symmetry, and symplectic ($\beta = 4$) for time-reversal symmetric systems with broken spin rotation symmetry. Including spin-orbit and Zeeman coupling yields an extended random matrix theory with two more parameters, s and Σ, in addition to the usual Dyson parameter, β [45].

At zero magnetic field, the distribution of α for weak spin-orbit coupling is given by [22, 46, 55]

$$P_{\beta=1,\Sigma=1,s=2}(\alpha) = \sqrt{\frac{1}{\pi\alpha}} e^{-\alpha}, \tag{1.3}$$

whereas for strong spin-orbit coupling it is given by

$$P_{\beta=4,\Sigma=1,s=2}(\alpha) = 16\alpha^3 e^{-2\alpha} \left(K_0(2\alpha) + \left(1 + \frac{1}{4\alpha}\right) K_1(2\alpha) \right), \tag{1.4}$$

where K_0 and K_1 are modified Bessel functions. The distributions have $\overline{\alpha} = 1/2$ and $\overline{\alpha} = 4/5$ for weak and strong spin-orbit coupling, respectively. As discussed above, breaking time-reversal symmetry does not alter the statistics of α, so

$$P_{\beta=2,\Sigma=2,s=1}(\alpha) = P_{\beta=4,\Sigma=1,s=2}(\alpha). \tag{1.5}$$

Note that breaking time reversal symmetry does in fact change χ_s so that, for strong spin-orbit coupling,

*This can be shown by time-reversing the Schrödinger equation

the peak height distribution at high field is expected to be a scaled version of the zero-field distribution, *decreased* by the ratio $\chi_{s=2}/\chi_{s=1} \sim 1.4$ [46] due to lifting of Kramers degeneracy. This is in contrast to the weak spin-orbit case, where the high-field distribution differs markedly in shape from the zero-field distribution, and the high-field mean height is *increased* by a factor of 4/3 compared to zero field [55], consistent with experiment [24, 56].

1.3 Experiment parameters

The measured device was formed from a Ge/Si core/shell nanowire (10 nm Ge core, 2 nm Si shell)[†] placed on an array of Cr/Au bottom gates (2 nm/20 nm thick, 20 nm wide, 60 nm pitch) patterned by electron beam lithography on a lightly doped Si wafer, then covered with 25 nm of HfO_2 (grown by atomic layer deposition at 180°C) before depositing the wires. Patterned Ti/Pd ohmic contacts were deposited following a 3 s buffered HF etch. Conductance was measured in a dilution refrigerator with electron temperature $T \sim 100$ mK using standard lock-in techniques with ac excitation $V_{ac} = 100$ μV, except where noted. The lock-in excitation was chosen to be as large as possible without altering the peak height distribution. An in-line resistance of 4.2 kΩ was subtracted from all data.

A typical orbital level spacing of $\Delta \sim 0.2$ meV was measured from Coulomb blockade spectroscopy, as shown in Fig. 1.1, inset. The number of holes, N_H, in the Coulomb blockade regime was estimated to be roughly 600, based on counting Coulomb oscillations. The length of the quantum dot was in the range $L = 200 - 600$ nm, corresponding to the length of the middle segment and the wire. For wire width $w = 10$ nm, this gives $M = 4w/\lambda_F = 4 - 6$ occupied transverse modes, using a 3D estimate for the Fermi wavelength, $\lambda_F = (2\pi^2 L w^2/3N_H)^{1/3} \sim 6 - 9$ nm. The elastic scattering length $l = h\mu/\lambda_F e = 35 - 50$ nm and mobility $\mu \sim 800$ cm^2/Vs were extracted from the slope of the pinch-off curve (Fig. 1.5, inset) using $g = (\pi w^2/4L)\mu ne$ [49, 52]. Values in the open regime differ somewhat, as discussed in Sec. 1.5.

It is worth noting from the outset, that the requirements of Eqs. (1.3-1.5) are satisfied in this experiment. These equations require $\Gamma < kT < \Delta$. $\Gamma, kT < \Delta$ ensures transport through single energy levels, and $\Gamma < kT$ ensures that the rate equations apply [46, 57]. The temperature of the quantum dot is $kT = 60$ μeV, determined from Coulomb blockade thermometry. Note that $T > T_{\text{base}}$ because of the large lock-in excita-

[†]The device shown in Fig. 1.1 is lithographically identical to the one studied here. However, in the measured device the nanowire forms a smaller angle with B of 31° determined from optical microscopy.

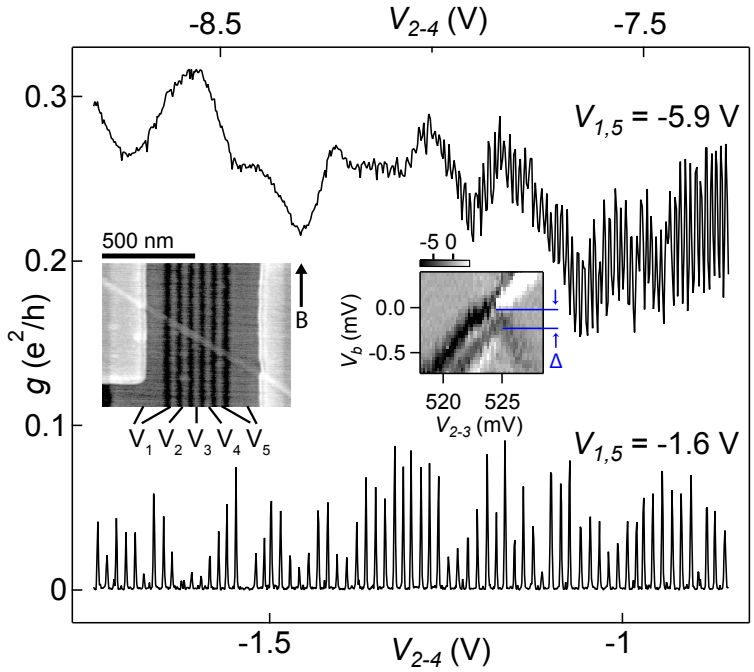

Figure 1.1: Device conductance, g, as a function of gate voltages, V_{2-4} [notation indicates $V_2 = V_3 = V_4$], with $V_{ac} = 50\ \mu\text{V}$. The device can be configured as an open wire (top trace), or an isolated quantum dot (bottom trace). *Left inset:* SEM micrograph of lithographically identical device. Direction of magnetic field B indicated by vertical arrow. *Right inset:* dg/dV_B in $(\text{e}^2/h)/\text{mV}$ as a function of dc bias, V_b, and gate voltages, V_{2-3}, yield orbital energy spacing $\Delta \sim 0.2$ meV.

tions used when gathering Coulomb peak statistics. The average tunnel rate is $\overline{\Gamma} = 7$ μeV, determined from the zero-field average Coulomb peak height at zero field using $\overline{g}_p = \chi_{s=2}\frac{e^2}{h}\frac{\overline{\Gamma}}{2kT}\overline{\alpha}$. The mean level spacing is $\Delta = 0.2$ meV, determined from Coulomb blockade spectroscopy and confirmed by temperature dependence [Fig. 1.1, Fig. 1.2(c)]s. The requirement $\Gamma < kT < \Delta$ is therefore squarely satisfied in this experiment.

Equations (1.3-1.5) also require the quantum dot to be diffusive or chaotic. The quantum dot studied here is diffusive. There are at least $N_H = 600$ holes in the dot, determined from counting Coulomb oscillations. The length of the quantum dot lies in the range $L = 200 - 600$ nm, corresponding to the length of the middle segment and the entire wire. This implies $M = 4w/\lambda_F = 4 - 6$ occupied transverse modes. Here we have used the three-dimensional expression to estimate the Fermi wavelength $\lambda_F = 2L(\pi w)^2(3N_H)^{-1/3} \sim 6 - 9$ nm (justified when $M \gg 1$). The Drude elastic scattering length is $l = h\mu/\lambda_F e = 35 - 50$ nm. The mobility $\mu = 800$ cm^2/Vs, determined from the slope of the pinch-off curve in Fig. 1.5 inset and the Drude relation $g = \pi w^2 \mu n e/(4L)$, is consistent with previous estimates under similar conditions [49, 52]. The dot therefore satisfies $l < L$ and is diffusive.

1.4 Coulomb blockade measurements

Figure 1.1 shows the two-terminal conductance of the nanowire as a function of a common voltage on gates 2, 3 and 4, denoted V_{2-4}, for a common voltage on gates 1 and 5, $V_{1,5}$, corresponding to open regime (top trace) and tunneling regime (bottom trace). V_{2-4} tune the hole density, while V_1 tunes the left barrier and V_5 tunes the right barrier. Coulomb blockade peaks appear when left and right barriers have conductance less than $2e^2/h$. The open regime shows weak dependence on gate voltage, with an onset of Coulomb oscillations as conductance decreases; the tunneling regime showed well defined Coulomb blockade peaks with fluctuating heights. The heights of neighboring peaks appear correlated over roughly two peaks, even at the lowest temperatures, similar to [24], which decreases the effective ensemble size.

Representative sets of Coulomb blockade peaks at $B \sim 0$ and 6 T [Figs. 1.2(a,b)] show a decrease in average peak height at high field, as expected for strong spin-orbit coupling. As temperature was increased above Δ, fluctuations in peak height decreased rapidly, consistent with a simple model that assumes resonant transport through multiple, uniformly spaced levels [Fig. 1.2(c)] (see "picket fence" model in Ref. [58]). Note that the same ensemble was used for each temperature. This presumably accounts for the

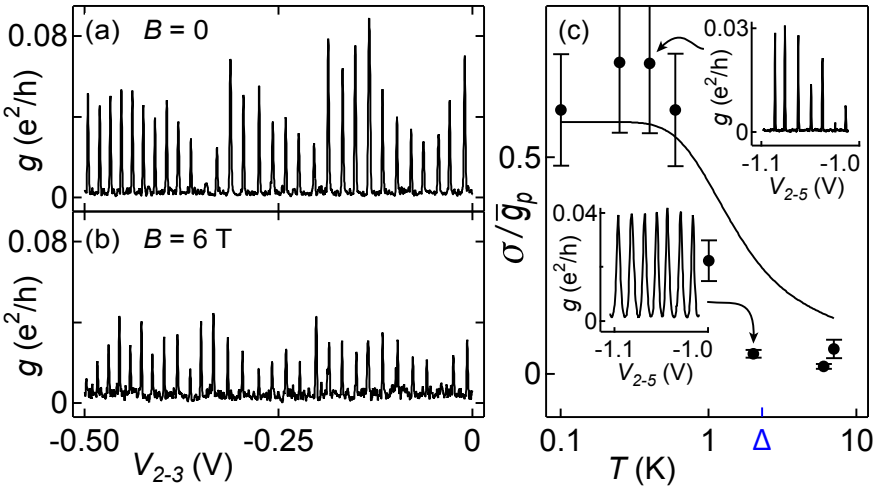

Figure 1.2: Conductance, g, as a function of gate voltages V_{2-3} with the device configured as a quantum dot for (a) $B = 0$ and (b) $B = 6$ T. The application of a magnetic field reduces the average peak height. (c) Peak height standard deviation normalized by the ensemble-averaged peak height, $\sigma/\bar{g}_p$, versus temperature T at $B = 0$ ($V_{ac} = 10$ μV), based on ~ 50 peaks per point. Fluctuations of peak heights decrease for $kT \sim \Delta$. Theory curve has no free parameters (see text). Insets: sample of peaks showing diminished fluctuations at higher temperature.

correlated departures from theory at low temperature. The discrepancy with theory at high temperature is unexplained, and is reminiscent of [59].

We now turn to an examination of the statistical properties of the Coulomb peaks. To increase the number of statistically independent Coulomb peaks, the gate V_4 was swept until Coulomb peaks became uncorrelated, as shown in Fig. 1.3. The number of peaks that can be acquired using this technique is eventually limited by the fact that large excursions in V_4 change the tunnel rates to the leads. Two families of Coulomb peaks, at $V_4 = 0.2$ V and $V_4 = -0.1$ V were selected and their height distributions examined.

Peak height histograms for all $m = 142$ Coulomb peaks show the evolution of the distribution as a function of magnetic field [Fig. 1.4(a)]. The observed decreasing average peak height at higher fields—Coulomb blockade antilocalization—as well as the maximum in the distribution away from zero height at all fields, are both signatures of strong spin-orbit coupling.

Figures 1.4(b,c) show peak height distributions, $P(g_p) = (\overline{\alpha}/\bar{g}_p)P_{\beta,\Sigma,s}(\overline{\alpha}g_p/\bar{g}_p) = N/(mW)$, where W is the bin width and N is the bin count in Fig. 1.4(a), at low and high magnetic fields.

The low-field data in Fig. 1.4(b) agree with the theoretical distribution for strong spin-orbit coupling ($\beta = 4$), with the mean peak height taken from Fig. 1.4(a), and are inconsistent with the theoretical distri-

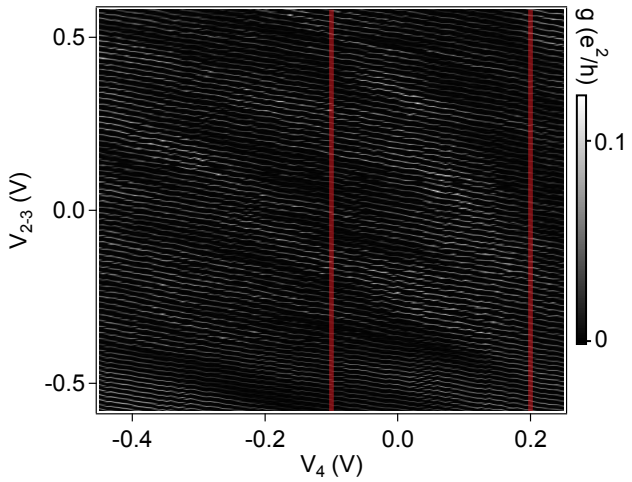

Figure 1.3: Device conductance g as a function of gate voltages V_{2-3} and V_4. Red lines indicate the values of V_4 used for the Coulomb peak ensemble in Fig. 1.4.

bution for weak spin-orbit coupling ($\beta = 1$). The high-field data in Fig. 1.4(c) are consistent with a scaled version of the low-field theoretical distribution, as expected for strong spin-orbit coupling, but with a scale factor of $\sim$ 2.3 rather than the theoretically predicted factor of 1.4. The reason for this discrepancy—qualitative scaling, but not by the predicted factor—is not understood, but may result from changes in tunnel rates out of the dot or changes in density of states in the leads, which are also likely segments of the nanowire.

The distribution of Coulomb peak spacings, another statistical property that in principle contains information about symmetries of wave functions, have also been examined [60]. The measured distributions appear Gaussian with similar widths for zero and higher magnetic fields, with a standard deviation of 0.5 meV. This width is comparable to the single-particle level spacing, as seen in previous experimental studies [23, 60]. Peak spacing distributions are more susceptible to experimental noise than peak height distributions, so it is not surprising that peak height distributions show field dependence while spacing distributions do not. Symplectic statistics associated with strong spin-orbit coupling have been measured in the spacings between excited states in metallic quantum dots [61].

1.5 Open regime measurement

To compare antilocalization in the Coulomb blockade regime to the open-wire regime, we tuned the device to more negative gate voltages, where Coulomb blockade oscillations were absent [see Fig. 1.1(a)]. The

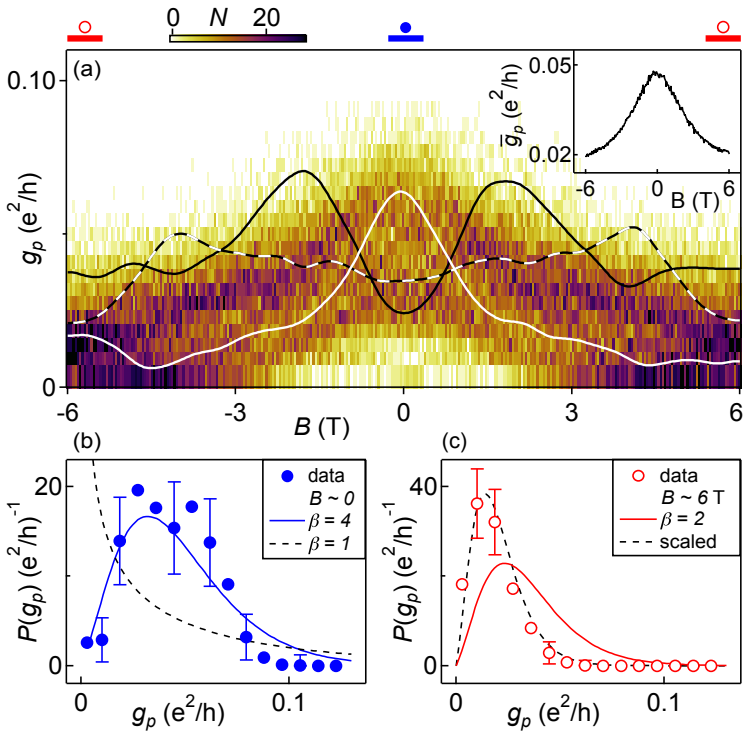

Figure 1.4: (a) Histograms of Coulomb blockade peak heights (color scale) as a function of magnetic field, B. Line traces show the smoothed conductance of three individual Coulomb peaks. Average peak height decreases with B, while individual peak heights fluctuate. *Inset:* Measured mean peak height, $\bar{g}_p$, as a function of B, extracted from data in main figure. (b) Peak height distribution, $P(g_p)$, for $B \sim 0$ (range shown as blue band at the top of (a)). Theory curves from Eq. (1.4) (solid) and Eq. (1.3) (dashed). (c) Peak height distribution, $P(g_p)$, for $|B| \sim 6$ T (range shown as red bands at the top of (a)). Theory curves from Eq. (1.5) (solid), which is the same as Eq. (1.4) scaled by $8(3-2\sqrt{2}) \sim 1.4$ and Eq. (1.4) scaled by a factor of 2.3 (dashed). The single experimental parameter $\overline{\Gamma}/(kT)$ is fixed using $\bar{g}_p$ at $B = 0$ from (a) inset.

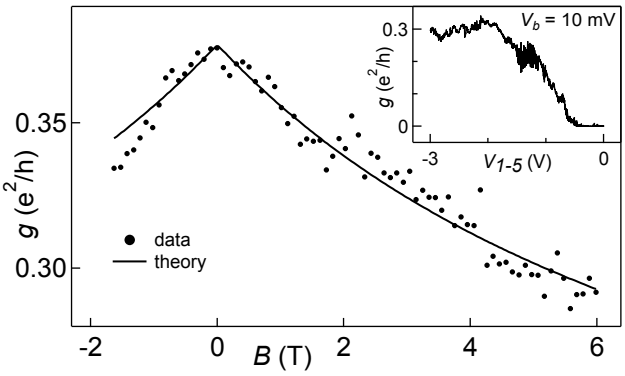

Figure 1.5: Two-terminal conductance, g, in the open-wire regime as a function of magnetic field, B, (points) along with theory, based on Eq. (1.6), including contact resistance. Fit bounds spin-orbit length, $l_{so} < 20$ nm. *Inset:* Pinch-off curve at bias $V_b = 10$ mV. Saturation at $g \sim 0.3$ e^2/h indicates decreasing mobility in the open regime (see text).

number of holes was larger in the open regime, $N_H \sim 1700$ and $\lambda_F \sim 6$ nm, again determined by counting Coulomb oscillations and assuming the device is depleted at pinch-off. The inset of Fig. 1.5 shows that high-bias conductance saturates at larger negative gate voltages, indicating a decreasing mobility with increasing density. Similar behavior has been reported in Ge/Si nanowires [49], Ge nanowires [62], and Si heterostructures [63]. In Si heterostructures, this decrease in mobility was explained as resulting from carriers being pulled toward the rough heterointerface, as well as an increase in phase space for scattering as more transverse subbands are occupied [63, 64]. Presumably, comparable effects occur in wires.

Magnetoconductance, $g(B)$, measured in the open-wire regime, is shown in Fig. 1.5 along with a theory curve that includes contributions from the wire, $g_w(B)^{-1}$, as well as from the two contacts, each set to $g_c^{-1} = 2e^2/h$ near the onset of Coulomb blockade, $g(B) = [2g_c^{-1} + g_w(B)^{-1}]^{-1}$. Following Ref. [39], we use the expression

$$
\begin{aligned}
g_w(B) = g_\infty - \frac{2e^2}{h}\frac{1}{L}\Bigg[&\frac{3}{2}\left(\frac{1}{D\tau_\varphi}+\frac{4}{3D\tau_{so}}+\frac{1}{D\tau_B}\right)^{-1/2} \\
&-\frac{1}{2}\left(\frac{1}{D\tau_\varphi}+\frac{1}{D\tau_B}\right)^{-1/2} \\
&-\frac{3}{2}\left(\frac{1}{D\tau_\varphi}+\frac{4}{3D\tau_{so}}+\frac{1}{D\tau_e}+\frac{1}{D\tau_B}\right)^{-1/2} \\
&+\frac{1}{2}\left(\frac{1}{D\tau_\varphi}+\frac{1}{D\tau_e}+\frac{1}{D\tau_B}\right)^{-1/2}\Bigg],
\end{aligned}
\tag{1.6}
$$

for the magnetoconductance of the wire, where g_∞ is the classical (background) conductance, $L \sim 600$ nm is the length of the occupied region of the nanowire, D is the diffusion constant, and τ_φ, τ_{so}, τ_B, τ_e are the dephasing, spin relaxation, magnetic, and impurity-impurity scattering times. In the present study, where $l_e \ll l_\varphi$, the last two terms of Eq. (1.6) do not play an important role, and in principle could be dropped. We retain these terms, though they have no discernible effect on the fits, for consistency with the existing literature [41, 44, 52, 65] for $w < l_e$.

The transport scattering length, $l_t = 2D/v_f$, where v_f is the Fermi velocity, the dephasing length, l_φ, and the spin precession length, l_{so}, then appear as [38, 40] $D\tau_\varphi = l_\varphi^2/2$, $D\tau_e = l_t l_e/2$, $D\tau_B = C_1 l_t l_B^4/w^3 + C_2 l_t l_e l_B^2/w^2$, and $D\tau_{so} = C_3 l_t l_{so}^4/w^3$, where $l_B^2 = \hbar/eB$. Constants $C_1 = 4\pi\,(9.5)$, $C_2 = 3\,(24/5)$ apply for diffusive (specular) boundary scattering [38], and we interpolate between these values for specularity, ε, between zero (fully diffusive) and one (fully specular). We use the specular value $C_3 = 130$ [40], lacking a theoretical value for diffusive boundary scattering. The ratio of scattering lengths depends on specularity and sample width, $l_t/l_e = F(w/l_e, \varepsilon)$, with $F(\cdot\,, 1) = 1$ [‡]. These expressions require $\lambda_F < w$ and $w < l_e$, the former barely satisfied for $\lambda_F = 6$ nm.

Four free parameters, l_{so}, g_∞, l_e, and l_φ, are used to fit theory to data. The transport scattering length is found from $l_t = (4L/\pi w^2) h g_\infty/\lambda_F n e^2$, where $n = 4N_H/\pi w^2 L$ is the 3D hole density (a reasonable model, given six occupied transverse modes). Specularity can then be found by inverting $l_t/l_e = F(w/l_e, \varepsilon)$, and the Fermi wavelength can be found from the 3D density, $\lambda_F = (8\pi/3n)^{1/3}$. As seen in Fig. 1.5, the model fits the data very well, and gives the following ranges for transport parameters, $g_\infty = 0.2 - 0.7\ e^2/h$, $l_e < 10$ μm, $l_t = 15$-25 nm $l_\varphi = (0.2 - 1.2)$ μm, specularity in the range $\varepsilon = 0.4 - 1$, and $l_{so} < 20$ nm. (Allowing $l_{so} > 20$ nm gives good fits only with $l_e > 10$ μm, which we rule out as unphysical.)

To give a better sense for the dependence of the conductance $g(B)$ on the four fit parameters, some sample curves are shown in Fig. 1.6, with parameter values summarized in Table 1.1. Calculating a normalized

[‡] F is given by [66]

$$F(\kappa, \varepsilon) = 1 - \frac{12}{\pi}(1 - \varepsilon^2) \sum_{\nu=1}^{\infty} \nu \varepsilon^{\nu-1} \int_0^1 dx \sqrt{1 - x^2} S_4(\nu\kappa x),$$

where $S_4(\lambda) = \int_0^{\pi/2} d\theta e^{-\lambda/\sin\theta} \cos^2\theta \sin\theta$.

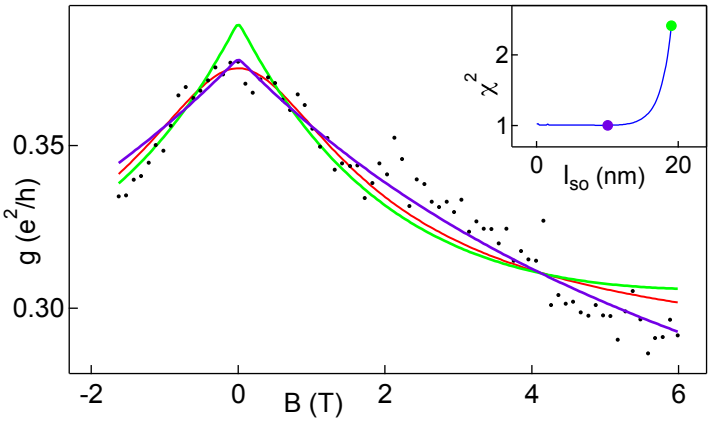

Figure 1.6: Device conductance, g, as a function of magnetic field, B, identical to Fig. 1.5 . The green and purple curves correspond to $l_{so} = 19$ nm and $l_{so} = 10$ nm with g_∞, l_e, and l_φ treated as fit parameters. The red curve is a fit assuming perfectly specular boundary scattering with l_{so}, g_∞, l_φ treated as fit parameters. Fit parameters for all curves are given in Table 1.1. *Inset:* Goodness of fit, χ^2, as a function of l_{so} with g_∞, l_e, and l_φ treated as fit parameters. The dots correspond to the l_{so} values of the curves in the main portion of the figure.

description	color	l_{so} (nm)	g_∞ (e^2/h)	l_e (nm)	l_φ (nm)
$l_{so} = 10$ nm	purple	fixed	0.25	10^4	610
$l_{so} = 19$ nm	green	fixed	0.67	10^4	1250
specular	red	1.4	0.39	15	190

Table 1.1: Parameters for curves in Fig. 1.6.

χ^2 statistic for a series of spin-orbit lengths while leaving the other three parameters g_∞, l_e, and l_φ free, reveals that χ^2 is essentially flat for sufficiently small spin-orbit lengths. We interpret this as as indicating that the data are consistent with $l_{so} < 20$ nm, although the presence of correlated errors due to $1/f$ device noise excludes the use of a formal χ^2 analysis. The roll of specularity was also explored; fixing perfectly specular reflection gives an extremely short spin-orbit lengths, of order 1 nm.

For meaningful fits, it was important to constrain a maximum elastic scattering length, here $l_e < 10$ μm. This constraint is generous; high mobility GaAs samples typically have scattering lengths of order microns, and the mobility of nanowires is many orders of magnitude lower. Tightening the constraint on l_e would lower the bound on l_{so}.

1.6 Discussion

As a comparison between open and nearly isolated regimes, we note that the observation of antilocalization in Coulomb blockade implies $\varepsilon_{so} > \Delta$ where ε_{so} is the spin-orbit energy in the dot [46]. To convert this into a spin-orbit length we assume the simple relation $\varepsilon_{so} = \hbar^2/(2m^* l_{so}^2)$ [53] and the bulk heavy-hole effective mass $m^* = 0.28m_e$. This gives $l_{so} < 25$ nm, consistent with the open regime measurement of $l_{so} < 20$ nm.

It is interesting to consider the reason for the large magnetic field scale associated with antilocalization in both regimes. Flux cancellation due to boundary scattering is known to enhance the effective magnetic length [38]. For Rashba type spin-orbit interactions, which are expected in Ge-Si, flux cancellations of the effective spin-orbit magnetic field can also occur [40]. These effects roughly cancel out, and the field scale for antilocalization is then $l_B = l_{so}$, or $B^* = \hbar/(el_{so}^2) = 3$ T for $l_{so} = 15$ nm.

In summary, this chapter presented an experimental study of Coulomb blockade peak height statistics in a Ge/Si nanowire quantum dot. Peak height distributions as well as the field dependence of average peak height (antilocalization) are consistent with the effects of strong spin-orbit coupling. However, the observed decrease in average peak height with applied magnetic field is larger than expected. Magnetoconductance of the same device configured as an open wire yields consistent results. Further investigation of the spin-orbit strength in this system could come from spectroscopic measurements of orbital anticrossings in a quantum-dot, or from electric-dipole spin resonance measurements in a Ge/Si double quantum dot. Combined with the expectation of long spin dephasing times in Ge/Si quantum dots, the strong spin-orbit coupling found in this work makes Ge/Si nanowire quantum dots attractive for spin qubit applications. A Ge/Si spin qubit is demonstrated in Chap. 2.

2

Hole dephasing in a Ge/Si nanowire

This chapter describes a measurement of the hole dephasing time in a Ge/Si core/shell nanowire spin qubit. The bulk of the chapter was published as Ref. [67], which Thorvald Larsen helped write. Experiments were carried out under the supervision of Charles Marcus and Ferdinand Kuemmeth, with experimental assistance from Patrick Herring. Nanowires were grown by Jun Yao and Hao Yan, under the supervision of Charles Lieber. Discussions with Félix Beaudoin, Bill Coish, Jeroen Danon, Xuedong Hu, Christoph Kloeffel, Franziska Maier and Mark Rudner were very helpful while writing up the data.

2.1 Introduction

Realizing qubits that simultaneously provide long coherence times and fast control is a key challenge for quantum information processing. Spins in III-V semiconductor quantum dots can be electrically manipulated, but lose coherence due to interactions with nuclear spins [6, 68, 69]. While dynamical decoupling and feedback have greatly improved coherence in III-V qubits [70–72], the simple approach of eliminat-

ing nuclear spins using group IV materials remains favorable. Carbon nanotubes have been investigated for this application [8, 73–75], but are difficult to work with due to uncontrolled, chirality-dependent electronic properties. So far, coherence has not been improved over III-V spin qubits.

Si devices have shown improved coherence for gate-defined electron quantum dots [10, 76–78], and for electron and nuclear spins of phosphorous donors [79–82]. The Ge/Si core/shell heterostructure nanowire is an example of a predominantly zero-nuclear-spin system that is particularly tunable and scalable [49, 83–86]. As discussed in Chapter 1 holes in Ge/Si nanowires exhibit large spin-orbit coupling [27, 52, 53], a useful resource for fast, all-electrical control of single spins [9, 75, 87–89]. Moving to holes should also improve coherence because the contact hyperfine interaction, though strong for electrons associated with *s*-orbitals, is absent for holes associated with *p*-orbitals [90]. Indeed, a suppression of electron-nuclear coupling in hole conductors was recently demonstrated in InSb [91].

Here, we measure spin coherence times of gate-confined hole spins in a Ge/Si nanowire double quantum dot using high bandwidth electrical control and read out of the spin state. We find inhomogeneous dephasing times T_2^* up to 0.18 μs, twenty times longer than in III-V semiconductors. This timescale is consistent with dephasing due to sparse ^{73}Ge nuclear spins (see Sec. 2.2). The observed exponential coherence decay suggests a dephasing source with high-frequency spectral content, and we discuss a few candidate mechanisms. These results pave the way towards improved spin-orbit qubits and strong spin-cavity coupling in circuit quantum electrodynamics [92].

2.2 Theoretical expectation for T_2^*

In this section we present a theoretical estimate of the timescale of hole spin dephasing due to dipolar hyperfine coupling. The dephasing time is set by the dipolar coupling constant for the ^{73}Ge isotope, A_h^{Ge}, which is not well known. We estimate its magnitude using the contact hyperfine constant in GaAs, A_e^{GaAs}, determined by spin qubit dephasing times in these systems.

$T_2^* = \sqrt{2}h/\sigma$ is related to the nuclear hyperfine coupling constants by [90]

$$\sigma^2 = \frac{1}{4N}\sum_j \nu_j I^j (I^j+1)(A^j)^2, \tag{2.1}$$

where the sum is over the nuclear species with abundance ν_j and spin I^j, and N is the total number of nuclei overlapped by the hole wavefunction. The wavefunction amplitude is assumed to be homogeneous at each nuclear site. Because all isotopes of Ga and As have $I^j = I^{\mathrm{GaAs}} = 3/2$, Eq. (2.1) can be rewritten as

$$\sigma^2 = \frac{1}{4N} I^{\mathrm{GaAs}}(I^{\mathrm{GaAs}}+1)\sum_j \nu_j (A_e^j)^2 = \frac{1}{4N} I^{\mathrm{GaAs}}(I^{\mathrm{GaAs}}+1)(A_e^{\mathrm{GaAs}})^2, \tag{2.2}$$

where the last equality defines A_e^{GaAs}. In GaAs $T_2^* = 10-30$ ns [6, 68, 93, 94], implying $A_e^{\mathrm{GaAs}} = 200-600$ μeV assuming 10^6 nuclei.

We assume that $A_e^{\mathrm{GaAs}} \approx A_e^{\mathrm{Ge}}$ because both result from contact hyperfine interaction in 4*s* orbitals, and use the approximate scaling factor from Fischer et al [90] to estimate A_h^{Ge}:

$$\frac{A_h}{A_e} = \frac{1}{5}\left(\frac{Z_{\mathrm{eff}}(Ge,4p)}{Z_{\mathrm{eff}}(Ge,4s)}\right)^3. \tag{2.3}$$

The ratio of effective nuclear charges is $\frac{Z_{\mathrm{eff}}(Ge,4p)}{Z_{\mathrm{eff}}(Ge,4s)} = 0.84$ [95]. $A_e^{\mathrm{Ge}} = 200-600$ μeV then implies $A_h^{\mathrm{Ge}} = 20-70$ μeV. Eq. (2.3) agrees with experimental measurements in III/V semiconductor dots to within 10-20 % [91, 96]. σ is then calculated using Eq. (2.1), assuming $N = 3\times10^5$ (dot length 80 nm) and the natural abundance values 0.92 for $I = 0$ (^{70}Ge, ^{72}Ge, ^{74}Ge) and 0.08 for I=9/2 (^{73}Ge). This gives $\sigma = 25-90$ neV.

The expected dephasing time for holes confined in the germanium core of our devices is therefore $T_2^* = \frac{\sqrt{2}h}{\sigma} = 65-230$ ns, in agreement with the experimental value $T_2^* = 180$ ns, found below. We emphasize that this estimate is rough. In particular the actual size of both GaAs and Ge dots are not well known, which introduces uncertainty in the estimate for *N*.

2.3 Setup and charge readout

Ge/Si core/shell nanowires host a tunable hole gas in the Ge core [Fig. 2.1(a)] with typical mobility $\mu \sim 1000\ \mathrm{cm}^2/(\mathrm{V}\cdot\mathrm{s})$. In the presence of realistic external electric fields, the 1D hole gas is expected to occupy a single Rashba-split subband with ~ 1 meV spin-orbit splitting, based on theory [53] and previous experiments [27, 52]. Fabrication of double dots with discrete hole states, and measurements of spin relaxation have been reported [50, 97].

The device, diagrammed in Fig. 2.1(b), is fabricated on a lightly doped Si substrate. The substrate, in-

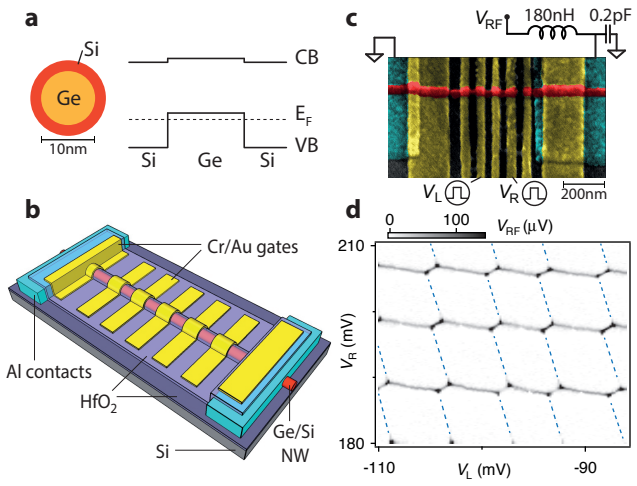

Figure 2.1: Ge/Si double quantum dot device. **a**, Cross section and energy diagram of conduction band (CB) and valence band (VB). The quantum well supporting the hole gas forms in the VB of Ge. **b**, Device schematic. **c**, False color scanning electron micrograph. High-bandwidth plunger gates V_L and V_R are labeled. V_{RF} is reflected from the LC circuit attached on the right lead. **d**, Demodulated V_{RF} versus V_L and V_R at $B = 1$ T. Negatively sloped gray lines correspond to single-hole transfers between the right dot and right lead. Positive slopes are due to hole transfers directly between dots. Guides to the eye (dashed lines) indicate hole transfers between the left dot and lead, too faint to be visible in the data because the resonator is on the right side.

sulating at $T < 10$ K, is covered with HfO_2 using atomic layer deposition. Nanowires are deposited from methanol solution and contacted by evaporating Al following a buffered hydrofluoric acid dip. A second layer of HfO_2 covers the wire, and Cr/Au electrostatic gates are placed on top. These gates tune the hole density along the length of the wire. All data are obtained at temperature $T < 100$ mK in a dilution refrigerator with external magnetic field $B = 0$, unless otherwise noted.

Gate voltages are tuned to form a double quantum dot in the nanowire with control over charge occupancy and tunnel rates. High-bandwidth (400 MHz) plunger gates V_L and V_R, labeled in Fig. 2.1(c), control hole occupation in the left and right dots. The readout circuit is formed by wire bonding a 180 nH inductor directly to the source electrode of the device. Combined with a total parasitic capacitance of 0.2 pF, this forms an LC resonance at 830 MHz with bandwidth 15 MHz. Tunneling of holes between dots or between the right dot and lead results in a capacitive load on the readout circuit, shifting its resonant frequency. [98, 99]. The circuit response is monitored by applying near-resonant excitation to the readout circuit and recording changes in the reflected voltage, V_{RF}, after amplification at $T = 4$ K and demodulation using a 90° power splitter and two mixers at room temperature [*].

[*] S. Weinreb LNA SN68. Minicircuits ZP-2MH mixers. Tektronix AWG5014 waveform generator used on V_L and

The charge stability diagram of the double dot is measured by monitoring V_{RF} at fixed frequency while slowly sweeping V_L and V_R [Fig. 2.1(d)]. To reject low-frequency electrical noise the RF carrier (frequency $\approx$ 830 MHz) is turned on and off at a rate of 157 Hz, and the reflected RF signal, demodulated by homodyne mixing, is fed into a SR830 lock-in amplifier. This lock-in technique was used only for Fig. 2.1(d), although conceptually similar differential methods are employed below. In addition to the lock-in technique, the plunger gates are pulsed in a square wave along the detuning axis on a microsecond timescale. These fast pulses, designed to search for Pauli blockade, result in a "negative copy" of the stability diagram, which are not shown.

Lines are observed whenever single holes are transferred to or from the right dot. Transitions between the left dot and left lead are below the noise floor (not visible) because the LC circuit is attached to the right lead. Enhanced signal is observed at the triple points, where tunneling is energetically allowed across the entire device. The observed "honeycomb" pattern is consistent with that of a capacitively-coupled double quantum dot [100]. The charging energies for the left and right dots are estimated 1.7 meV and 2.7 meV from Fig. 2.1(d), using a plunger lever arm of 0.3 eV/V, determined from finite bias measurements on similar devices [50]. The few-hole regime was accessible only in the right dot, identified by an increase in charging energy. Based on the location of the few-hole regime in the right dot, we estimate the left and right hole occupations to be 70 and 10 at the studied tuning. We found that operating in the many-hole regime improved device stability, facilitating gate tuning and readout. We do not know if this affects the quality of the qubit, as recently found for electron spins in GaAs [101].

2.4 Spin readout

The spin state of the double dot is read out by mapping it onto a charge state using the Pauli blockade pulse sequence diagrammed in Fig. 2.2. At the points E1 and E2 ("empty") the double dot is in the (m+2, n+1) charge state, assuming that m (n) paired holes occupy lower orbitals in the left (right) dot. Pulsing to P ("prepare") in (m+1, n+1) discards one hole from the left dot, leaving the spin state of the double dot in a random mixture of singlet and triplet states. Moving to M ("measure") adjusts the energy detuning between the dots, making interdot tunneling favorable. When M is located at zero detuning, $\varepsilon = 0$, tunneling is

V_R. Coilcraft 0603CS chip inductor.

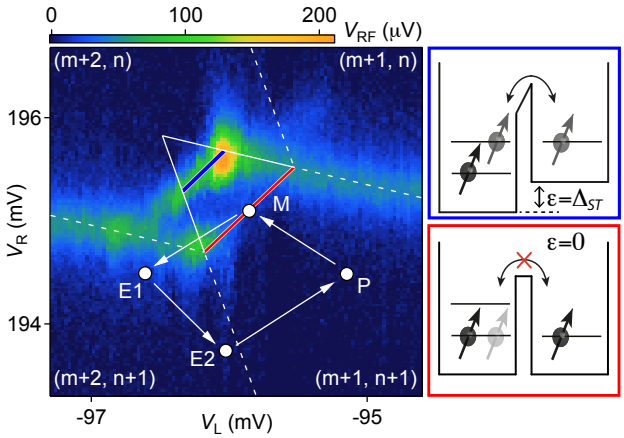

Figure 2.2: Spin readout using Pauli blockade. V_{RF} at the measurement point $M = (V_L, V_R)$ of the pulse sequence indicated by white arrows. Dashed lines estimate changes in double dot hole occupancy (m, n), where m (n) denotes the occupancy of the left (right) dot. Large solid triangle outlines the region over which direct interdot charge transitions occur. The interdot transition at $\varepsilon = 0$ (marked by a red line) is weak due to Pauli blockade of triplet states, illustrated in the red diagram. The interdot transition at $\varepsilon = \Delta_{ST}$ (marked by a blue line) is strong due to tunneling of triplet states, illustrated in the blue diagram.

allowed for singlet but Pauli-blocked for triplet states. When M is at the singlet-triplet splitting, $\varepsilon = \Delta_{ST}$, triplet states can tunnel. The location of the interdot charge transition therefore reads out the spin state of the double dot. We expect this picture to be valid for multi-hole dots with an effective spin-$\frac{1}{2}$ ground state [97, 101–103]. We use singlet-triplet terminology for clarity, but note that strong spin-orbit coupling changes the spin makeup of the blockaded states without destroying Pauli blockade [104].

The fast pulse sequence E1→E2→P→M→E1 is repeated continuously while rastering the position of $M = (V_L, V_R)$ near the (m+1, n+1)-(m+2, n) charge transition (Fig. 2.2). The RF carrier is applied only at the measurement point, M. As shown in Fig. 2.1(d), features with negative slope are observed corresponding to transitions across the right barrier. We interpret the weak interdot transition at zero detuning accompanied by a relatively strong interdot feature at large detuning as Pauli blockade of the ground-state interdot transition ($\varepsilon = 0$), and lifting of blockade at the singlet-triplet splitting ($\varepsilon = \Delta_{ST}$). The strength of the $\varepsilon = 0$ interdot transition thus measures the probability of loading a singlet at point P, while the strength at $\varepsilon = \Delta_{ST}$ measures the probability of loading a triplet.

As a control, the Pauli blockade pulse sequence was run in the opposite direction, where it is not expected to result in the appearance of a triplet trunneling feature. The reasoning is that the reverse sequenc initializes an (m+2, n) at point P, which can always be separated into the (m+1, n+1) charge state at the

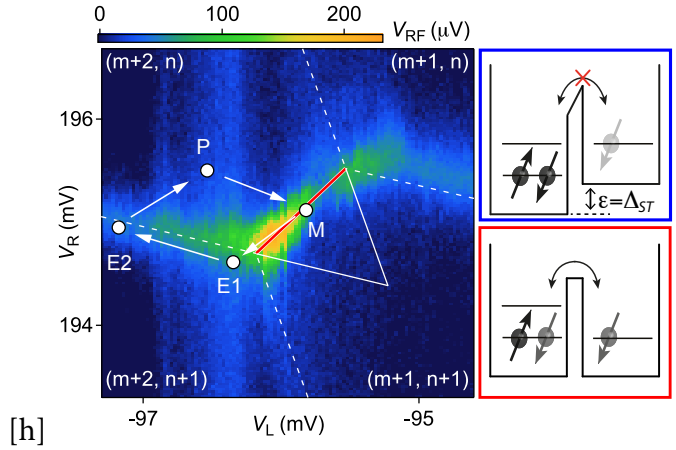

[h]

Figure 2.3: Reversed T_1 pulse sequence. V_{RF} at the measurement point $M = (V_L, V_R)$ of the reversed, cyclical Pauli blockade pulse sequence, indicated by white arrows. The pulse diagram has been scaled by a factor of 0.8 to fit on the plot. Dashed lines estimate changes in double dot hole occupancy (m, n), where m (n) denotes the occupancy of the left (right) dot. Large solid triangle outlines the region over which direct interdot charge transitions can occur.

interdot transition. The reversed sequence initializes only singlets, so no blockade signal is expected. Running the reversed sequence, only the singlet-singlet interdot transition is observed (Fig. 2.3), as expected for Pauli blockade.

2.5 Spin relaxation

Spin relaxation is measured by varying the dwell time τ_M at the measurement point for the counterclockwise Pauli-blockade sequence. As τ_M increases the triplet transition weakens and the singlet transition strengthens [Fig. 2.4(a,b)] due to triplet-to-singlet spin relaxation. Note that these relaxation processes have different charge characters at different measurement points. For example, at $\varepsilon = 0$ the initial charge state is (m+1, n+1), whereas at $\varepsilon = \Delta_{ST}$ the initial charge state is hybridized with (m+2, n).

The T_1 spin relaxation time is measured by analyzing a cut along the V_ε axis [shown in Fig. 2.4(b)] and varying τ_M. Two example cuts are shown in Fig. 2.4(c) The cuts were obtained in software post-processing in three steps. First, the colorscale of the 2D images [e.g. Fig. 2.4(a,b)] are scaled to take into account the duty cycles of the different pulse sequences, by multiplying each pixel by τ_Σ/τ_M where τ_Σ is the total pulse sequence length. Second, a constant voltage is subtracted from each image such that $V_{RF} = 0$ corresponds to Coulomb blockade. Finally, we removed a small glitch due to a time-constant effect in the dc DAC

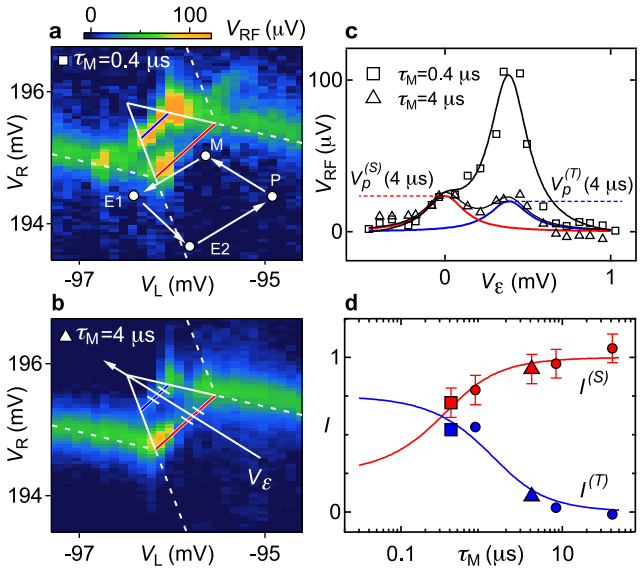

Figure 2.4: Spin relaxation. **a**, V_{RF} at the measurement point $\mathrm{M} = (\mathrm{V_L}, \mathrm{V_R})$ of T_1 pulse sequence (arrows). The dwell time at M is $\tau_{\mathrm{M}} = 0.4$ μs. **b**, Same as (**a**), but with $\tau_{\mathrm{M}} = 4$ μs. **c**, Cuts along the V_ε region indicated in (**b**) for $\tau_{\mathrm{M}} = 0.4$ μs (□) and $\tau_{\mathrm{M}} = 4$ μs (△). Each cut is fit with the sum of two Lorentzians, the left of height $V_p^{(S)}$ and right of height $V_p^{(T)}$. The center of the left Lorentzian defines zero detuning, $V_\varepsilon = 0$. **d**, Readout visibility $I^{(S,T)} = V_p^{(S,T)}/V_0^{(S,T)}$ as a function of τ_{M}. Fits are to Eqs. (2.4,2.5) and have characteristic decay times $T_1^{(S)} = 200$ ns and $T_1^{(T)} = 800$ ns for singlet and triplet states. Normalization factors are $V_0^{(S)} = 25$ μeV and $V_0^{(T)} = 200$ μeV.

$V_R \approx 196$ mV by subtracting a suitable background near $V_R = 196$ mV. This glitch occurred whenever the DC component of V_R crossed 196 mV, independent of V_L. At this plunger gate voltage, data acquisition briefly paused while new calibrated plunger voltage values were loaded into the DC voltage source. This lookup process caused a small voltage spike in V_{RF} that does not represent any properties of the device itself. Software post-processing is done in three steps. First, the colorscale of images in Figures 2-4 are scaled to take into account different duty cycles of the different pulse sequences, by multiplying each pixel by τ_Σ/τ_M where τ_Σ is the total pulse sequence length. Second, a constant voltage is subtracted from each image such that $V_{RF} = 0$ corresponds to Coulomb blockade. Finally, we removed a glitch due to a time-constant effect in the dc voltage source occurring near $V_R = 196$ mV, independent of V_L. At this plunger gate voltage, data acquisition briefly paused while new values were loaded into the DC voltage source. The additional settling time caused a small voltage spike in V_{RF} that does not represent any properties of the device itself. Cuts along the V_ε axis are taken in software and numerically smoothed to remove pixelation errors.

For each τ_M, the cut is fit to the sum of two Lorentzians with equal widths and constant spacing, as shown in Fig. 2.4(c). The Lorentzian heights, $V_p^{(T)}$ for the triplet peak and $V_p^{(S)}$ for the singlet peak, are fit to the exponential forms

$$V_p^{(S)}(\tau_M) = \tfrac{1}{4} V_0^{(S)} \left[4 - 3p\left(\tau_M, T_1^{(S)}\right)\right], \tag{2.4}$$

$$V_p^{(T)}(\tau_M) = \tfrac{3}{4} V_0^{(T)} p\left(\tau_M, T_1^{(T)}\right), \tag{2.5}$$

where $p(\tau_M, T_1) = (1/\tau_M)\int_0^{\tau_M} e^{-t/T_1} dt$ is the exponential decay averaged over the measurement time. Figure 3(d) plots the readout visibility, $I^{(S,T)} = V_p^{(S,T)}/V_0^{(S,T)}$, extracted from the V_ε cuts. The fit relaxation time is $T_1^{(T)} = 800$ ns at the triplet position [blue line in Figs. 3(a,b)], and $T_1^{(S)} = 200$ ns at the singlet position [red line in Figs. 3(a,b)]. We note that these spin relaxation times are three orders of magnitude shorter than those previously measured in a similar device in a more isolated gate configuration and away from interdot transitions [97]. Detuning dependence of spin relaxation has been observed previously and attributed to detuning-dependent coupling to the leads as well as hyperfine effects (presumably the former dominate here) [105, 106]. Relaxation due to the spin-orbit interaction is expected to take microseconds

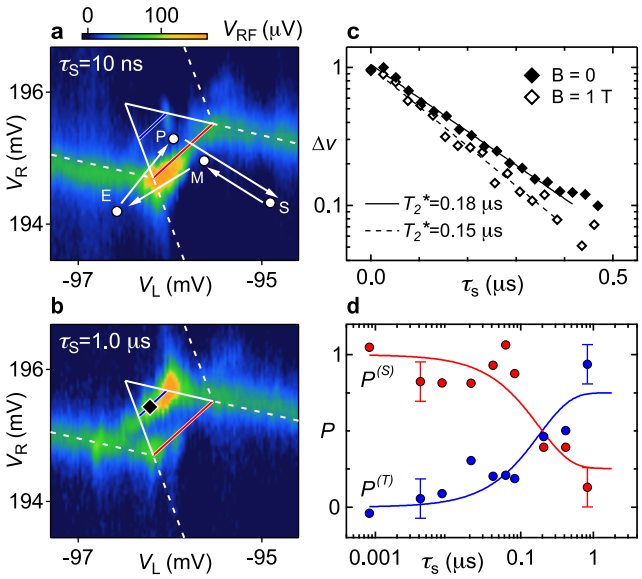

Figure 2.5: Spin dephasing. **a**, V_{RF} at the measurement point $M = (V_L, V_R)$ of T_2^* pulse sequence (arrows). The dwell time at S is $\tau_S = 10$ ns. **b**, Same as (**a**), but with $\tau_s = 1$ μs. **c**, Normalized differential voltage at the triplet line $\Delta v \equiv [V(\tau_S) - V_\infty]/[V(0) - V_\infty]$ as a function of τ_S. The $B = 0$ T data are measured at (V_L, V_R) indicated in (**b**), yielding a T_2^* dephasing time of 0.18 μs. The $B = 1$ T data are obtained at a different dot occupancy and tuning using the same method, yielding $T_2^* = 0.15$ μs. The normalization factor is $V_{RF}(0) - V_\infty = 35$ μV. Solid and dashed lines are fits to exponentials. **d**, Probability $P^{(S,T)} = V_p^{(S,T)}/V_0^{(S,T)}$ obtained from data as in (**a**,**b**), analyzed as in Fig. 2.4(c). Fits are to Eqs. (2.6,2.7) with $T_2^* = 0.18$ μs fixed from (**c**). Normalization factors are $V_0^{(S)} = 60$ μeV and $V_0^{(T)} = 130$ μeV.

or longer [107]. The difference between $V_0^{(S)}$ and $V_0^{(T)}$ can possibly be attributed to differences in singlet-singlet and triplet-triplet tunnel couplings or enhanced coupling near the edges of the pulse triangle. The separation between Lorentzian peaks by 0.38 mV can be interpreted as $\Delta_{ST} = 160$ μeV, using a plunger lever arms of 0.3 eV/V.

2.6 Spin dephasing

To investigate spin dephasing, an alternate pulse sequence is used that first initializes the system into a singlet state in (m+2, n) at point P, then separates to point S ("separate") in (m+1, n+1) for a time τ_S [Fig. 2.5(a)]. The spin state of the double dot is measured at M by pulsing back towards (m+2, n). For short τ_S [Fig. 2.5(a)] a strong singlet return feature is observed, consistent with negligible spin dephasing. For long τ_S [Fig. 2.5(b)], a strong triplet return feature is observed, consistent with complete spin dephasing.

The T_2^* dephasing time is found by measuring $V_{RF}(\tau_S)$ at the triplet transition, and plotting the normal-

ized differential voltage $\Delta v \equiv [V_{\mathrm{RF}}(\tau_S) - V_\infty]/[V_{\mathrm{RF}}(0) - V_\infty]$ as a function of separation time [Fig. 2.5(c)]. Here, $V_\infty \equiv V_{\mathrm{RF}}(500\ \mathrm{ns})$ is the demodulated voltage for a pulse sequence with long dephasing time. The quantity $[V_{\mathrm{RF}}(\tau_S) - V_\infty]$ is directly measured by alternating between the T_2^* sequence and a reference sequence with long dephasing time, and feeding the demodulated voltage into a lock-in amplifier. Fitting the $B = 0$ data to $\exp[-(\tau_S/T_2^*)^\alpha]$ yields $\alpha = 1.1 \pm 0.1$. Figure 4(c) shows exponential fits ($\alpha = 1$) for both data sets. The $B = 0$ data decays exponentially on a timescale $T_2^* = 0.18$ µs. Data acquired at $B = 1$ T at a different double-dot occupation give a similar timescale and functional form.

Although this timescale is approaching the limit expected for dephasing due to random Zeeman gradients from sparse ^{73}Ge nuclear spins (see Sec 2.2), the observed exponential loss of coherence is by and large unexpected for nuclei. A low-frequency-dominated nuclear bath is expected to yield a Gaussian fall-off of coherence with time [108], in contrast to the observed exponential dependence, which instead indicates a rapidly varying bath [109]. Nuclei can produce high-bandwidth noise in the presence of spatially varying effective magnetic fields, for example due to inhomogeneous strain-induced quadrupolar interactions [110]. The similarity of data at $B = 0$ and $B = 1$ T in Fig. 2.5(c), however, would indicate an unusually large energy-scale for nuclear effects. Electrical noise, most likely from the sample itself, combined with spin-orbit coupling is a plausible alternative. For electrons, the ubiquitous $1/f$ electrical noise alone does not result in pure dephasing [111], but can add high-frequency noise to the low-frequency contribution from the nuclear bath. It is conceivable that the behavior is different for holes, but this has not been studied to our knowledge. The relative importance of nuclei versus electrical noise could be quantified in future experiments by studying spin coherence in isotopically pure Ge/Si nanowires.

Cuts along the V_ε axis in Fig. 2.5(b) as a function of τ_S provide a second method for obtaining T_2^*, following analysis along the lines of Fig. 2.4(c). The resulting probability $P^{(S,T)} = V_p^{(S,T)}/V_0^{(S,T)}$ versus τ_S is shown in Fig. 2.5(d), along with exponential curves

$$V_p^{(S)}(\tau_S) = P_\infty V_0^{(S)} \left[1 - (1 - 1/P_\infty) e^{-\tau_S/T_2^*}\right], \tag{2.6}$$

$$V_p^{(T)}(\tau_S) = (1 - P_\infty) V_0^{(T)} \left[1 - e^{-\tau_S/T_2^*}\right], \tag{2.7}$$

using $T_2^* = 0.18$ µs, with P_∞ and $V_0^{(S,T)}$ as fit parameters. Depending on the nature of the dephasing, the

singlet probability settling value, P_∞, is expected to range from 1/3 for quasi-static Zeeman gradients to 1/4 for rapidly varying baths [112–114]. We find $P_\infty = 0.25 \pm 0.08$. Equations (2.6,2.7) do not take into account spin relaxation at the measurement point, meaning that the fitted P_∞ systematically overestimates the true settling value [†]. Therefore, we conclude that the data weakly support $P_\infty = 1/4$ rather than $P_\infty = 1/3$, consistent with our inference of a rapidly varying bath.

2.7 Discussion

Unexplained high-frequency noise has recently been observed in other strong spin-orbit systems, such as InAs nanowires [9], InSb nanowires [89], and carbon nanotubes [75]. In these systems slowly varying nuclear effects were removed using dynamical decoupling, revealing the presence of unexplained high-frequency noise. In our system the effect of nuclei is reduced by the choice of material, and an unexplained high-frequency noise source appears directly in the T_2^*. These similarities suggest the existence of a shared dephasing mechanism that involves spin-orbit coupling.

Future qubits based on Ge/Si wires could be coupled capacitively [115, 116] or through a cavity using circuit quantum electrodynamics [92, 106]. In the latter case, the long dephasing times measured here suggest that the strong coupling regime may be accessible.

[†]We do not correct for T_1 effects in Eqs. (2.6,2.7), as $V_{\max}^{(S,T)}$ differed significantly from those observed in Fig. 2.4.

3

Multi-electron spin qubit in GaAs

This chapter describes experiments demonstrating operation of a multi-electron spin qubit, performed under the supervision of Ferdinand Kuemmeth and Charles Marcus. The bulk of the chapter was published as Ref. [101], with Sec. 3.5 added to discuss dephasing in the small exchange limit. GaAs wafers were grown by M. P. Hanson and A. C. Gossard, and the device was fabricated by Christian Barthel.

3.1 Introduction

Spin-1/2 quantum dots with controlled exchange coupling form a potentially powerful platform for manipulating quantum information [36]. Single electrons confined by electrostatic gates in semiconductors are a well-developed realization of this system, and meet many of the basic requirements of quantum information processing. A broad research effort has emerged under this approach, focused on materials such as GaAs [6, 70, 116], carbon nanotubes [117], InAs [9, 106], InSb [89], and Si [10, 79]. In each system, producing large numbers of single-electron quantum dots places severe demands on materials and device de-

sign, and is a considerable obstacle to scalability. [*] Moving from single confined electrons to multi-electron qubits alleviates these difficulties, and, as we show, can also improve performance.

Requirements for conventional spin qubits include a spin-1/2 ground state, and a gap to excited states larger than temperature and the energy scales associated with control and coupling. For realistic densities, interactions are relatively weak, typically (though not always) resulting in a spin-1/2 ground state for odd occupancy [118]. Multi-electron dots can have higher-spin ground states and smaller-than-average gaps to the first excited state, due for instance to accidental degeneracies in their excitation spectrum. This concern may partially explain why there have been relatively few studies of their use as spin qubits. In practice, however, such degeneracies are typically lifted by desymmetrizing the confining potential or changing the applied magnetic field [102, 119].

Previous experimental work on multi-electron quantum dots has demonstrated Pauli blockade [73, 74, 97, 103, 120–122] and coherent operation [106]. In single-electron dots, both nuclear [71, 123] and electrical [124, 125] dephasing have been characterized, with electrical noise modeled as a fluctuating detuning between double-dot levels. Multi-electron quantum dots have also received theoretical attention due to ease of realization as well as possibly improved performance [102, 119, 126–128].

In this Chapter, we investigate coherent exchange oscillations in coupled multi-electron GaAs quantum dots—this operation was specifically chosen to be sensitive to electrical noise—and compare results to oscillations in the same device operated with single-electron dots. Our primary finding is that multi-electron qubits can be operated analogously to the single-electron case, which alleviates the need for singly-occupied dots. We also find significantly improved coherence in the multi-electron case, consistent with expectations of screening by core electrons [102, 126]. By analyzing the dephasing during the exchange-gate operation, we characterize the electrical noise environment for each occupancy. For both single and multiple occupancies, voltage noise affecting the detuning between dots dominates dephasing for large exchange, and fluctuating hyperfine (Overhauser) fields dominate dephasing for small exchange. For a range of intermediate exchange, an exchange-independent dephasing mechanism of unknown origin is dominant. The upshot of this work is that one can simultaneously relax fabrication requirements and improve qubit performance

[*] Fabrication yield for gate-defined dots is above 0.9 for established recipes. Tuning multi-dot devices to the single-electron regime has lower yield, ∼0.5 per dot, due to disorder and unoptimzed gate designs. Tuning to the few (5-10) electron regime is highly reliable, with yield above 0.9.

by working in the multi-electron regime. We also investigate the effect of multi-electron operation on nuclear dephasing and read-out, finding that both are weakly altered by multi-electron operation.

3.2 Setup and Operation

The double quantum dot has an integrated charge sensor, formed by Ti/Au depletion gates patterned by electron beam lithography on the surface of a GaAs/$Al_{0.3}Ga_{0.7}As$ heterostructure with two-dimensional electron gas (2DEG) of density $\sim 2 \times 10^{15}$ m^{-2} and mobility 20 m^2/Vs, located 100 nm below the wafer surface. The charge configuration of the double dot is detected using a conductance measurement of a proximal quantum dot (Fig. 3.1(a)) [93]. All measurements are performed in a dilution refrigerator with an electron temperature of $\sim$50 mK. A sufficiently large in-plane magnetic field is applied to isolate the $m_S = 0$ subspace of the double dot Hamiltonian. Specific values of field are given for particular data sets, with no observed dependence on the value of field within the range 50 – 200 mT.

Negative voltages were applied to the gate electrodes in order to form two quantum dots with several GHz of tunnel coupling. Plunger gate voltages V_L and V_R control electron occupancy in the left and right dots, denoted (n, m), and also control interdot tunneling via the detuning, $\varepsilon \propto (V_L - V_R)$. When each dot forms a spin-1/2 system, tunneling occurs only between singlet-correlated dots due to Pauli blockade. The result is that the singlet (S) state can lower its energy with respect to the triplet (T_0) by an exchange energy J (cf. Fig. 3.1(b)). When these states are split by J, the device is in a superposition of different charge states, and is therefore susceptible to electrical noise.

To set up the exchange oscillation measurement, an adiabatic ramp to $J = 0$ maps the initialized S state to the lower zero-spin eigenstates of the Overhauser nuclear field (see Fig. 3.1(b)). Next, a square exchange pulse applied to ε turns on exchange $J(\varepsilon)$ for a time τ, accumulating a phase of $2\pi J(\varepsilon)\tau$ between S and T_0. In terms of the $J = 0$ eigenstates, this phase accumulation corresponds to oscillations between the ground and excited state at frequency of J. Finally, the $J = 0$ eigenstates are mapped via a reverse ramp onto S and T_0, which project differently into charge states of the double-dot, resulting in a different sensor dot conductance.

By varying ε and τ, and repeating the cycle for $>$10 minutes to average over the nuclear and electrical fluctuations, we generate a family of oscillating curves for the device configured with single (Fig. 3.1(c))

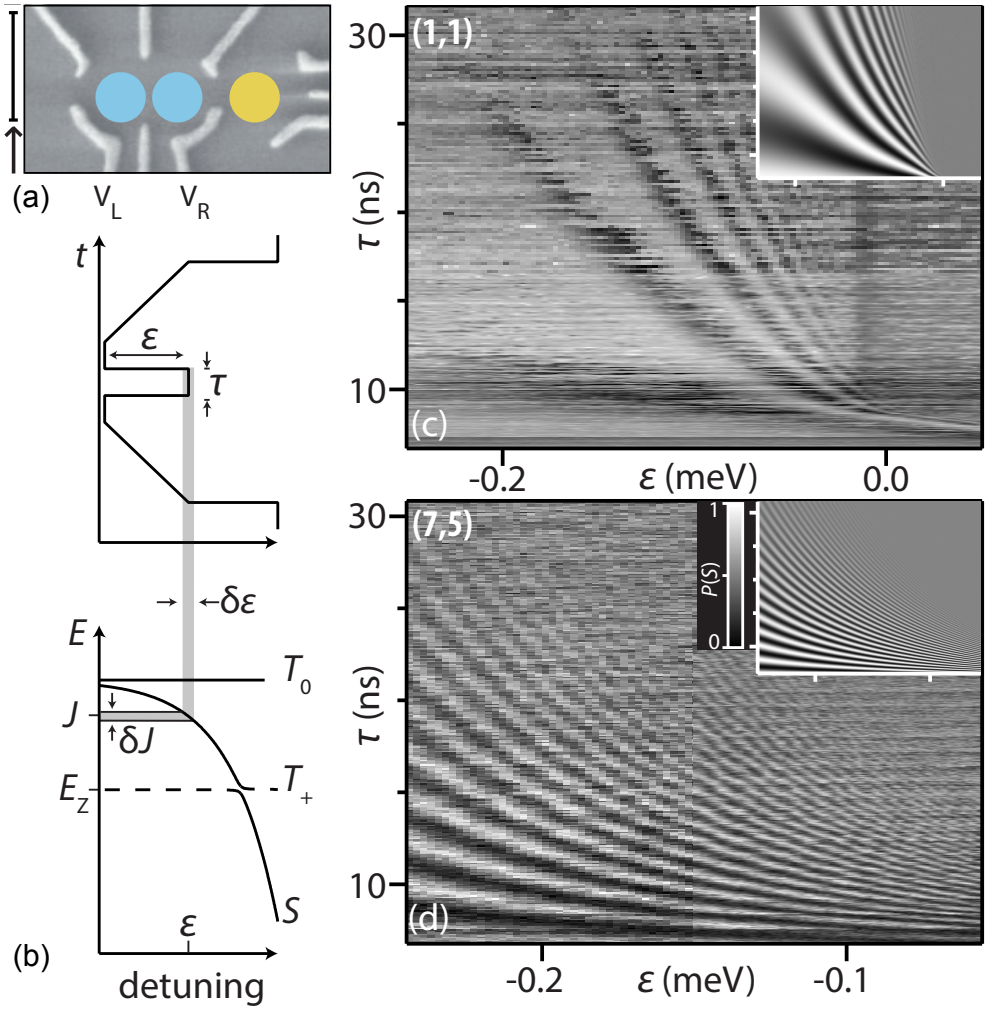

Figure 3.1: (a) Scanning electron micrograph of lithographically identical device, indicating double dot (blue) and charge sensor (yellow). Scale bar indicates 500 nm, arrow indicates magnetic field direction [200 mT for (1,1), 50 mT for (7,5)] and [110] crystal axis. (b) Schematic exchange pulse sequence. An adiabatic ramp to $J = 0$ initializes the system in the lowest energy $m_S = 0$ eigenstate before an exchange pulse of duration τ to detuning ε is applied. Detuning noise, $\delta\varepsilon$, induces exchange fluctuations, δJ, which limits the number of visible exchange oscillations at high detuning. (c) Probability of detecting a singlet, $P(S)$, as a function of detuning and exchange time for single-electron dots. (d) Same as (c) but for multi-electron dots. Coherence is significantly improved for the multi-electron exchange case. *Insets:* Simulated exchange oscillations (see text). Color scale shared for all 2D plots.

and multiple (Fig. 3.1(d)) electrons. The sensor conductance was normalized to 1 at its first maximum and 1/2 at its settling value such that it reflects a singlet return probability, $P(S)$.

The central result is that not only are exchange oscillations observed between multiply-occupied dots, showing that a multi-electron dot forms a good qubit, but that the quality of these oscillations is improved over the singly-occupied case. This is shown in Fig. 3.1, where we observe high-quality exchange oscillations between multi-electron dots that clearly outperform the single-electron case in the same device. We have examined exchange gates between multi-electron dots at different electron-number occupations for three different cool-downs and two different devices with similar results.

3.3 Noise analysis

We now examine the origin of the improvement observed in the multi-electron exchange gate. We consider a model that includes several contributions to the total dephasing rate, Γ, including ε-equivalent noise (Fig. 3.1(b)), which dominates at large J, ε-independent dephasing, which dominates at intermediate J, and dephasing due to random gradients in the Overhauser field in the z-direction, which dominates for small J. We find that this model is sufficient to describe our observations over the entire parameter range of Fig. 3.1 (insets).

Exchange oscillations were fit with a decaying sinusoid of the form

$$\exp[-(\Gamma\tau)^2]\cos(2\pi J\tau+\varphi), \tag{3.1}$$

with fit parameters Γ, J, and φ. A phase shift φ can arise from bandwidth limits in the apparatus. Exchange oscillations are well fit by this Gaussian envelope, and inconsistent with an exponential envelope (see Sec. 3.6), consistent with [125]. The form of this decay envelope has physical implications: an exponential envelope can indicate either Gaussian-distributed white noise or Lorentzian-distributed low-frequency noise in exchange. A Gaussian envelope, on the other hand, reflects Gaussian-distributed low frequency (compared to $1/\tau$) exchange noise [108, 125].

Figure 3.2(a) shows extracted values of $J(\varepsilon)$ from the fits. For single-electron occupation, $J(\varepsilon)$ can be found in regions where oscillations are not visible from the position of the S-T_+ anticrossing. This anti-

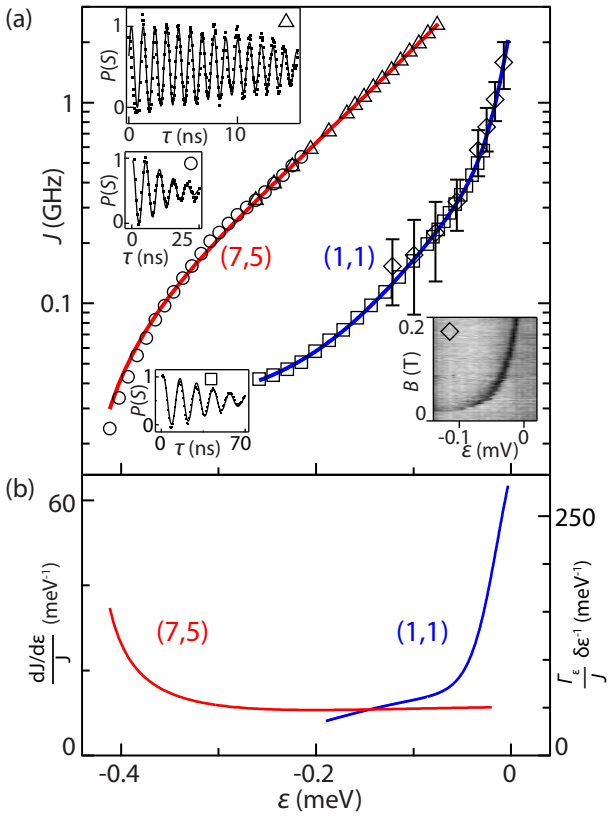

Figure 3.2: (a) Exchange coupling, $J(\varepsilon)$, as a function of detuning, ε, for the single- and multi-electron exchange gate. Data extracted from exchange oscillations (represented in insets) below (square,circle markers) and above (triangle markers) the range of the waveform generator (Tektronix AWG5014), measured by externally stepping the clock, and from the location of the S-T_+ anticrossing ($\Diamond$), where Zeeman and exchange energies are equal. Fits are to bi-exponential models (see text). (b) $(\mathrm{d}J/\mathrm{d}\varepsilon)/J$, obtained numerically from the fits in (a), reflects the dephasing per exchange pulse due to ε-noise. As ε approaches zero, the multi-electron exchange gate should display improved coherence for equal amounts of ε-noise. This is consistent with the observation of improved coherence in the multi-electron case.

crossing occurs when the Zeeman splitting, $E_Z = g\mu_B B$, is equal to the exchange $J(\varepsilon)$ (see Fig. 3.1(b) for $J(\varepsilon) = |E_Z|$), resulting in a change of sensor conductance (color scale of inset $\diamondsuit$, Fig. 3.2(a)) due to leakage into the T_+ state. J is extracted assuming the bulk g-factor $g = -0.44$.

The component of dephasing attributable to fluctuations in detuning, denoted Γ_ε, depends on $dJ/d\varepsilon$, as illustrated in Fig. 3.1(b). For Gaussian low-frequency (compared to $1/\tau$) ε-noise,

$$\Gamma_\varepsilon = \frac{\mathrm{d}J}{\mathrm{d}\varepsilon}\pi\sqrt{2}\delta\varepsilon, \tag{3.2}$$

where $\delta\varepsilon$ is the *rms* ε-equivalent noise [108, 125]. To determine $dJ/d\varepsilon$, exchange profiles [Fig. 3.2(a)] were fit using a bi-exponential form, $A + B\exp[-k_1\varepsilon] + C\exp[-k_2\varepsilon]$. Figure 3.2(b) shows that as ε approaches zero, $(dJ/d\varepsilon)/J$ grows for the single-electron case, but saturates at a small value for the multi-electron case, consistent with the screening of ε-noise by core electrons. Thus, the shape of the exchange profile $J(\varepsilon)$ for the multi-electron dots explains some immunity to ε-equivalent noise. However, at more negative detuning Γ_ε for (1,1) falls below that of (7,5). This is qualitatively inconsistent with our observations in Fig. 3.1(c) and suggests a deviation from the ε-equivalent noise model. The remainder of this Letter is concerned with developing a phenomenological noise model that describes our data.

We quantitatively examine the ε-noise model by extracting $\delta\varepsilon$ from our data. This can be done without assuming a particular functional form for $dJ/d\varepsilon$ by recasting Eq. 3.2 in integral form. Note that in the presence of only ε-noise the number (quality), Q, of observed oscillations satisfies the identity $J = Q \cdot \Gamma_\varepsilon$. Substituting Eq. 3.2 for Γ_ε and integrating both sides of this identity with respect to ε gives

$$\int J d\varepsilon = \pi\sqrt{2}\delta\varepsilon \int Q\frac{dJ}{d\varepsilon}d\varepsilon. \tag{3.3}$$

Considering Q to be a function of J, these integrals can be rewritten

$$\int^{\varepsilon_i} J d\varepsilon = \pi\sqrt{2}\delta\varepsilon \int^{J(\varepsilon_i)} Q dJ. \tag{3.4}$$

In Fig. 3.3(a,b) we numerically compute the integrals in Eq. 3.4 as a function of the upper-bound detuning point ε_i using the J and Q values from exchange oscillations in Fig. 3.2. A linear relationship reflects

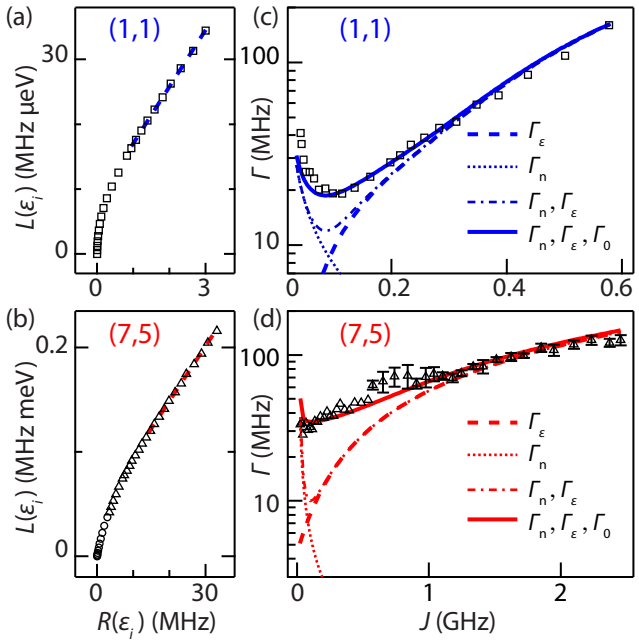

Figure 3.3: Plotting the left side integral, $L(\varepsilon_i)$, versus the right side integral, $R(\varepsilon_i)$, of Eq. 3.4 allows us to extract an *rms* ε-noise of (a) $\delta\varepsilon = 2.0$ μeV for (1,1) and (b) $\delta\varepsilon = 1.2$ μeV for (7,5) dot occupations (dashed lines). Deviations from linear behavior indicate the presence of non-ε-noise. Using the extracted values for $\mathrm{d}J/\mathrm{d}\varepsilon$ and $\delta\varepsilon$, the dephasing rate due to ε-noise, Γ_ε, can be predicted without any free parameters. For both (c) (1,1) and (d) (7,5), the system is dominated by ε-noise at large J, but decoheres due to an unknown source at small J. The excess dephasing rate is not explained by nuclei (Γ_n), but is well captured by a model (Γ_Σ) that includes a constant dephasing rate Γ_0 as its only free parameter (see text).

the dominant ε-equivalent noise, and the slope gives the noise strength. We find that the linear relationship between these integrals holds for large J, but not for intermediate and small J where other sources of dephasing dominate.

The measured dephasing rates, $\Gamma(J)$, are shown in Fig. 3.3(c,d) for single- and multi-electron cases. The deviation of $\Gamma(J)$ from the detuning-noise-only component, $\Gamma_\varepsilon(J)$, is evident for both the single- and multi-electron exchange operation. We next account for contributions to dephasing from fluctuations in the hyperfine field gradient, Γ_n, determined independently from measured dephasing time $T^*_{2,\mathrm{n}}$ in a diabatic singlet-separation measurement, following the analysis in Ref. [129]. The formula we use for Γ_n is valid for $J \gtrsim 1/T^*_{2,\mathrm{n}}$. In the limit of $J \ll 1/T^*_{2,\mathrm{n}}$, Γ_n decreases in proportion to J, as can be verified by explicitly integrating over the nuclear ensemble. This behavior is due to the following physical effect: nuclear fluctuations larger than J stop phase accumulation, but do not cause dephasing. Thus when J becomes small, random Overhauser field gradients cause the visibility of oscillations to go to zero but do not contribute more noise (see Sec. 3.5).

For intermediate values of J, the measured dephasing rate exceeds contributions from Γ_ε and Γ_n for the single- and multi-electron cases. The excess dephasing is well described by including a phenomenological additional dephasing rate, Γ_0, that is independent of detuning. Fits to the data in Fig. 3.3(c,d) yield $\Gamma_0 =$ 14 MHz for the single-electron case and $\Gamma_0 = 34$ MHz for the multi-electron case.

We take the total dephasing rate, $\Gamma_\Sigma = (\Gamma_\varepsilon^2 + \Gamma_\mathrm{n}^2 + \Gamma_0^2)^{1/2}$, as the quadrature sum of these contributions. Strictly speaking, nuclear noise and electrical noise should not be combined in quadrature because the exchange oscillation is not separable into nuclear and electrical contributions. However, we have verified numerically that this introduces a small error. Figure 3.4(a) compares the quality factor, Q, of exchange oscillations with the model value $J \cdot \Gamma_\Sigma$. The agreement between model and experiment is excellent in both the single- and multi-electron regimes. Model calculations shown in the insets of Figs. 3.1(c,d) also use these parameters.

The additional rate Γ_0 cannot be readily explained by higher-frequency electrical noise, as whitening the noise power spectrum would presumably increase dephasing for short exchange pulses. This would tend to increase dephasing at large J, opposite of the observed trend. As in [125] we observed no significant temperature dependence of quality factors when heating the mixing chamber from below 50 mK to 200

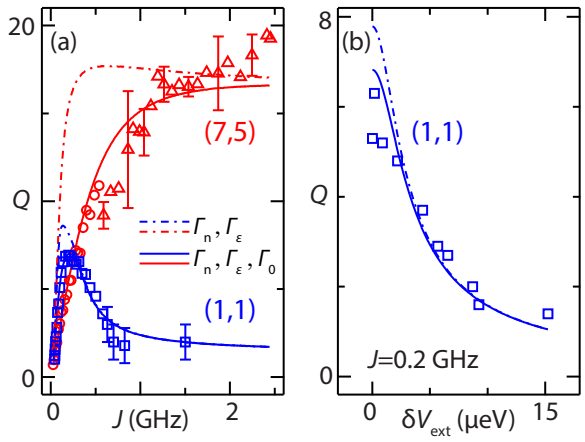

Figure 3.4: (a) Quality of exchange rotations, Q, as a function of J for (7,5) and (1,1). For large J, the multi-electron exchange gate significantly outperforms the single-electron gate. The model (solid lines) includes dephasing due to ε-noise, nuclei, and a constant Γ_0 to account for the unknown noise source discussed in Fig. 3.3. Also shown (dotted lines) are the same models without the contribution from Γ_0. (b) The observed reduction of Q when applying external voltage fluctuations of fixed amplitude δV_{ext} to the detuning axis is in good agreement with the model including Γ_0 (solid line), and is in disagreement with the model excluding Γ_0 (dotted line). All model parameters determined from other measurements. This serves as an independent check of our model parameters.

mK.

As a check of our noise model, we use the plunger gates to artificially expose the quantum dots to a known electrical noise environment and observe its effect on the quality of exchange rotations. A two-channel arbitrary waveform generator (Agilent 33522A) can emulate different noise spectra, as well as different noise correlations between right and left plunger voltages, that can be superimposed to the control voltages during the exchange pulse. To simulate ε-equivalent noise, we add anti-correlated voltage fluctuations of increasing *rms* amplitude to V_{L} and V_{R}, and observe exchange oscillations of decreasing quality factor. Figure 3.4(b) shows the expected decrease in Q for single-dot occupation at $J = 0.2$ GHz [†], in good agreement with the predictions from our noise model (solid line, no free parameters).

3.4 Full decoherence model and parameters

For completeness, we now give more complete details of the full dephasing model. The full decoherence model used, including the effects of Γ_0, Γ_n and Γ_ε, involves integrating over both the nuclear and electrical

[†]For Fig. 3.4(b), the Agilent 33522A waveform generator was programmed to output a 5 MHz sine wave (*i.e.* $\ll J$), phase-modulated at 19 kHz.

noise ensembles.

We begin with the usual Hamiltonian in the S-T_0 subspace [108]

$$H_0 = \frac{J}{2}(1+\tau^z) + \delta h^z \tau^x. \tag{3.5}$$

Here the τ^i are the Pauli matrices defined such that $\tau^z |T_0\rangle = |T_0\rangle$, $\tau^z |S\rangle = -|S\rangle$. J is the exchange energy (assumed to be noiseless for now) and δh^z is a random Overhauser gradient along the direction of the externally applied magnetic field. For the purposes of these calculations, we set $\hbar = 1$ and assume that $|+x\rangle = |S\rangle + |T_0\rangle$ is an eigenstate of the local effective Zeeman field in each dot. This is valid if we neglect transverse components of the Overhauser field, which holds for Zeeman fields due to the external magnetic fields much larger than the typical Overhauser fields (i.e., $\gg$ 5mT).

We are interested in the probability to rotate between $|+x\rangle$ and $|-x\rangle$ when applying H_0 for a time t, which is an experimental relevant quantity because $|+x\rangle$ and $|-x\rangle$ can be mapped to and from S and T_0, respectively, via an adiabatic ramp. In this case the expected oscillations are determined by the probability $P(T_0) = 1 - P(S) = \overline{|\langle -x| e^{-iH_0 t} |+x\rangle|^2}$. Here the overline $\overline{\cdots}$ denotes an average over the nuclear ensemble. Using standard identities we find

$$\langle -x| e^{-iH_0 t} |+x\rangle = e^{iJ/2t} \frac{J/2}{\sqrt{(\delta h^z)^2 + (J/2)^2}} \sin(\sqrt{(\delta h^z)^2 + (J/2)^2}t), \tag{3.6}$$

hence

$$|\langle -x| e^{-iH_0 t} |+x\rangle|^2 = \frac{1}{2}\frac{J^2}{J^2 + (2\delta h^z)^2}(1 - \cos(\sqrt{(2\delta h^z)^2 + J^2}t)). \tag{3.7}$$

Integrating of Gaussian distributed nuclear and exchange ensembles then gives

$$P(T_0) = \int_{-\infty}^{\infty}\int_{-\infty}^{\infty} dJdh P(J,\sigma_J)P(h,\sigma_h)K(J,h,t) \tag{3.8}$$

where

$$P(f,\sigma_f) = \frac{1}{\sqrt{2\pi}\sigma_f} e^{-f^2/2\sigma_f^2} \tag{3.9}$$

	J_0 (GHz)	J_1 (GHz)	J_2 (GHz)	k_1 (meV^{-1})	k_2 (meV^{-1})	$\delta\varepsilon$ (μeV)	Γ_0 (MHz)	σ_h (MHz)	α (e)
(1,1)	0.029	0.61	0.85	15	59	2.0	14	15	0.018
(7,5)	-0.42	0.70	5.5	1.34	12	1.2	33	13	0.012

Table 3.1: Parameters for dephasing model. See text for parameter definitions

and

$$K(J,h,t) = \frac{1}{2}\frac{J^2}{J^2+(2h)^2}(1-\cos(\sqrt{(2h)^2+J^2}2\pi t)) \tag{3.10}$$

Note that we have changed units so that J and h are frequencies (not angular frequencies).

The parameters in this model are σ_h and σ_J which quantify the total amount of exchange and nuclear noise. σ_h is determined from $T^*_{2,n}$ measurements according to

$$\sigma_h = \frac{1}{2\pi\sqrt{2}T^*_{2,n}} \tag{3.11}$$

where $T^*_{2,n}$ is the $1/e$ time from the curves in Fig. 3.9.

σ_J includes the contribution from both ε-noise (Γ_ε) and the unknown noise source (Γ_0) according to

$$\sigma_J = \frac{1}{\pi\sqrt{2}}\left(\Gamma_\varepsilon^2+\Gamma_0^2\right)^{1/2}, \tag{3.12}$$

where

$$\Gamma_\varepsilon = \pi\sqrt{2}\frac{dJ}{d\varepsilon}\delta\varepsilon, \tag{3.13}$$

and $\delta\varepsilon$ is the *rms* ε-equivalent electrical noise extracted from the slopes of Figs. 3(a,b).

Finally, $\frac{dJ}{d\varepsilon}$ is extracted by fitting $J(\varepsilon)$ to the double-exponential form as described in Fig. 3.1

$$J = J_0 + J_1 e^{k_1\varepsilon} + J_2 e^{k_2\varepsilon}. \tag{3.14}$$

All model parameters used in the text are summarized in Table 3.1. In this table α is the lever arm found from bias-triangles in transport.

3.5 Dephasing in the small-J limit

This section discusses dephasing in the small-J limit. The finding is that, even for vanishingly small exchange, electrical noise dominates the long-time behavior of the exchange oscillations.

To see how this arises, consider first the behavior of Eq. 3.8 in the absence of electrical noise. The triplet return probability with $\sigma_J = 0$ is

$$P(T_0) = \int_{-\infty}^{\infty} dh \frac{1}{\sqrt{2\pi}\sigma_h} e^{-h^2/2\sigma_h^2} \frac{1}{2} \frac{J^2}{J^2 + (2h)^2} (1 - \cos(\sqrt{(2h)^2 + J^2}t)). \tag{3.15}$$

To make the behavior of this integral more obvious we issue the change of variables $h \rightarrow h/J$, $\sigma = \sigma_h/J$, $\tau = Jt$. The integral becomes

$$\frac{J}{2\sqrt{2\pi}\sigma_h} \int_{-\infty}^{\infty} dh \frac{1}{1 + 4h^2} e^{-h^2/2\sigma^2} (1 - \cos(\sqrt{1 + 4h^2}\tau). \tag{3.16}$$

In the small-J limit ($\sigma \gg 1$) the integral is dominated by terms of order J ($h \lesssim 1$) because of the Lorentzian term. Physically, this is because large gradients δh^z freeze the system along the transverse axis of the Bloch sphere rather than introducing a random phase. The result is that exchange oscillations, in the absence of J noise, should be a universal function $F(Jt)$ scaled by J/σ_h:

$$P(T_0) = \overline{|\langle -x| e^{-iH_0 t} |+x\rangle|^2} = \frac{J}{\sigma_h} F(Jt) \tag{3.17}$$

where

$$F(Jt) = \frac{1}{2\sqrt{2\pi}} \int_{-\infty}^{\infty} dh \frac{1}{1 + 4h^2} (1 - \cos(\sqrt{1 + 4h^2}Jt) \tag{3.18}$$

is independent of the nuclear distribution.

To verify this reasoning, we numerically compute the integral in Eq. 3.16 for different values of σ. The results are presented in Fig. 3.5. Indeed, when $J \ll \sigma_h$ the exchange oscillations tend towards a zero-visibility function with a universal form (dashed blue line, Fig. 3.5(b)).

Thus, in the limit of arbitrarily large nuclear noise such that $J \ll \sigma_h$, the envelope of the exchange oscillations decays slowly in a universal way (see Fig. 3.5). In a real experiment, J-noise, always finite in practice,

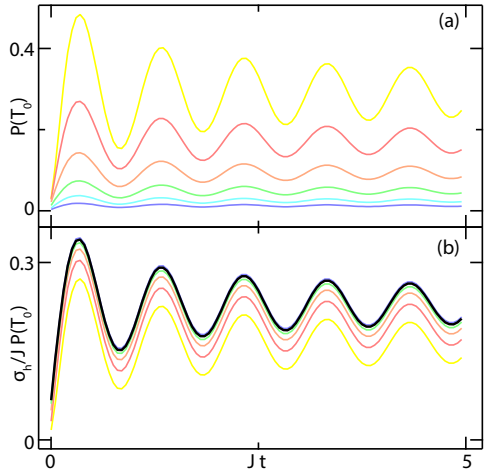

Figure 3.5: (a) Numerically integrated $P(T_0)$ versus Jt for $\sigma_h/J = 1, 2, 4, 8, 16, 32$ from top to bottom. The visibility of oscillations is clearly reduced when $J < \sigma_h$. (b) $\sigma_h/J \cdot P(T_0)$ versus Jt for $\sigma_h/J = 32, 16, 8, 4, 2, 1$ from top to bottom. Black line indicates the mathematical function $F(Jt)$. Scaling $P(S)$ by σ/J reveals that the quality of exchange oscillations tends towards the function $F(Jt)$ when $\sigma_h >> J$. This behavior is consistent with the asymptotic prediction of Eq. 3.17.

will dominate the envelope at long times, even though exchange is a small parameter ($J \ll \sigma_h$).

3.6 Justification of Gaussian envelopes

Here, we discuss our assumption of a Gaussian envelope of exchange oscillations, as given in Eq. 3.1. We consider different envelopes of the form

$$e^{-(\Gamma t)^p}, \tag{3.19}$$

where Γ is the decoherence rate and p is the envelope exponent (e.g., $p = 1$ is an exponential envelope, $p = 2$ is a Gaussian envelope). Figure 3.6(a) shows fits for large and small exchange, J, for single-electron dots, with p treated as a fit parameter. For $J < 0.1$, where nuclear fluctuations play an important role, the data are consistent with $p \lesssim 1$. However, in this regime theory predicts polynomial tails which differ from the form assumed by Eq. 3.19 [108]. The tendency towards small p in the nuclear dominated regime is due to the contribution of these polynomial tails, which result in a slower decay rate. For $J > 0.1$ GHz, where detuning noise dominates, data are consistent with $p = 2$, or a Gaussian envelope. Figure 3.6(b) shows an example of a trace that is well described by a Gaussian envelope.

We also consider the sensitivity of the extracted decoherence rate, Γ, to our choice in p. As shown in Fig. 3.6(c), Γ is essentially independent of p for $p \geq 2$. Since the data are better described by $p = 1$ in

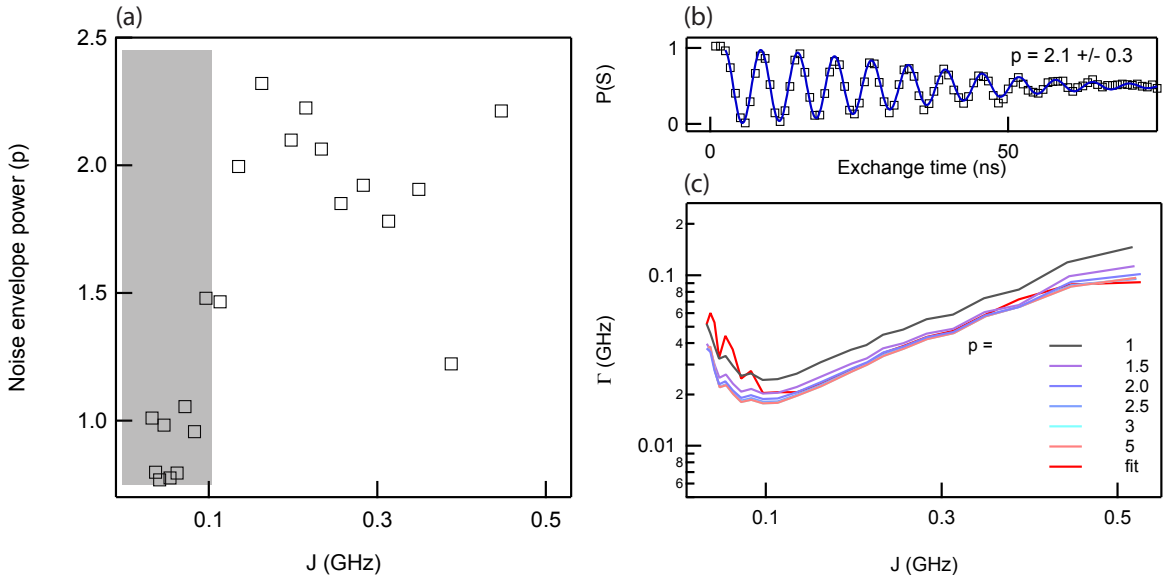

Figure 3.6: (a) Noise envelope power, p, as a function of exchange frequency, J. p is determined from a least-squares fit to exchange oscillations. For $J < 0.1$ GHz (shaded region) nuclear noise plays an important role and the envelopes are altered away from $p = 2$. For $J > 0.1$ GHz, where detuning noise dominates, the data are consistent with $p = 2$, or a Gaussian envelope. (b) Example of a fit for p at $J = 160$ MHz. The fit is consistent with $p = 2$, or a Gaussian envelope. (c) Experimental decoherence rate Γ, as a function of J for different noise envelope powers, p. The values p=1...5 show qualitatively similar behavior. For $J > 0.1$ GHz, where ε-noise dominates, the fit data are consistent with $p = 2$, and Γ is insensitive to the value of p.

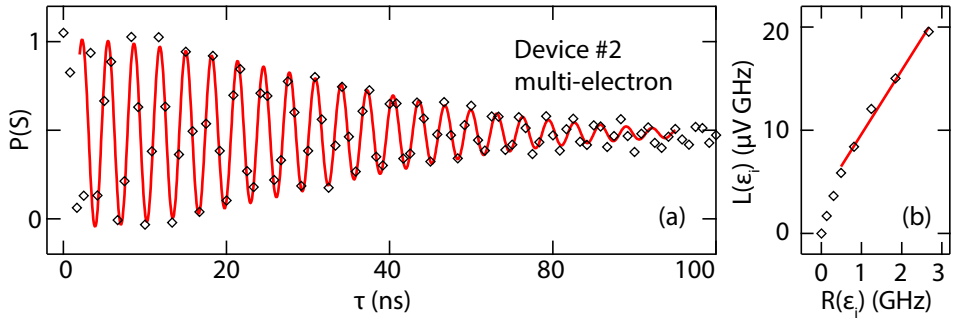

Figure 3.7: (a) Singlet return probability, $P(S)$, versus exchange time, τ, between multi-electron dots for device #2. High quality exchange oscillations are observed. (b) ε-noise extraction using the same method as Figs. 3(a, b). An *rms* ε-noise of 1.4 μeV is found. This is consistent with the values found in device #1, even though the lever-arm, α, in device #2 is almost three times as big. This suggests the ε-noise does not actually arise from voltage fluctuations on the plunger gates.

the nuclear regime, the analysis in the main text may underestimate the nuclear decoherence in the small J regime by roughly 15 MHz. However, these deviations are small and do not alter the conclusions of the paper. Since we only extract the $1/e$ time from our data, the insensitivity to p is expected.

3.7 Multi-electron operation in a second device

High-quality exchange oscillations between multi-electron dots of various occupancies where observed in device #1 in several cool downs. Multi-electron exchange oscillations from an independent device #2, lithographically identical to device #1 that has been discussed so far, are shown in Fig. 3.7. Both the quality of the oscillations, $Q \sim 15$, and the extracted ε-noise are consistent with the results found in device #1. For device #2 the gate lever arm with respect to the detuning axis was found larger than in device #1 (0.031e as opposed to 0.012e), suggesting that the ε-noise does not actually originate from the plunger gates or cryostat. Also, we have observed that the quality factors do not improve when adding attenuators to the output of the waveform generator, indicating that instrumental voltage fluctuations are not the dominating electrical noise source either. We believe that the dominating noise arises from within the GaAs substrate, but observed no significant temperature dependence of quality factors when heating the sample from below 50 mK to 200 mK.

3.8 Charge sensing and single-shot readout of a multi-electron singlet-triplet qubit

We demonstrate that multi-electron spin qubits can be initialized, manipulated, and read-out using the same procedures developed for single-electron spin qubits, including fast single-shot readout with integration times less than 1μs. In the main text we are interested in averaging over a slowly fluctuating ensemble, and so do not make use of single-shot readout. It is important, however, to demonstrate that single-shot readout works in the multi-electron regime.

Fig. 3.8(a) shows the stability diagram near the (4, 4)-(3, 5) transition. The zero-bias conductance g through a sensor quantum dot is measured with a lock-in. The gate voltages of the sensor dot were linearly cross compensated for changes in the right and left plunger gate voltages of the double quantum dot, V_R and V_L, defined as in [130, Fig. 3.1(a)]. The change of sensor conductance due to a charge rearrangement from (4, 4) to (3, 5) is shown in Fig. 3.8(b), and is large enough to allow high-fidelity single-shot readout.

Fig. 3.8(c) shows single-shot traces obtained by radio-frequency reflectometry similar to that described in [131] and employed in [93, 130]. A radio-frequency carrier (195 MHz, -105 dBm) is applied to a tank circuit (1200 nH surface-mount inductor by Coilcraft) connected to the sensor quantum dot. The carrier is only applied during the measurement segment a pulse cycle. The reflected power is preamplified by a low-noise cryogenic amplifier mounted on the still plate of the dilution refrigerator (Quinstar QCA-U230-30HZI), and further amplified at room temperature. Homodyne detection with appropriate low-pass filtering (Picosecond Pulse Labs 5915-100-31.5 MHz low-pass filter) then demodulates the sensor signal to a DC voltage, V_{rf}, that is sampled by a high-impedance input digital storage oscilloscope (Agilent MSO8104A, high-resolution mode, sampling speed 5MS/s). The sampled data shows abrupt changes in V_{rf} when a triplet state (high V_{rf}) decays into a singlet state (low V_{rf}). One such event is shown in Fig. 3.8(d). By averaging an ensemble of such single-shot traces the longitudinal relaxation time in the readout point of the qubit can be determined, here $T_1 = 10$ µs. If the integration subinterval after qubit manipulation is kept short compared to T_1, then a high-fidelity readout of the qubit states can be achieved by simply comparing the integrated V_{rf} to a threshold that separates singlet from triplet outcomes. For an integration time of 200 ns, we obtain a signal-to-noise ratio (SNR) of 217 mV/5.3 $\mathrm{mV_{rms}} = 4.1$. For comparison, using the quantum point contact signal of a (1,1)-(0,2) qubit, SNR ~ 1 for 400 ns of integration in [93]. Using a single quantum dot sensor, a SNR ~ 3 at 100 ns integration time was found using -99 dBm applied rf power

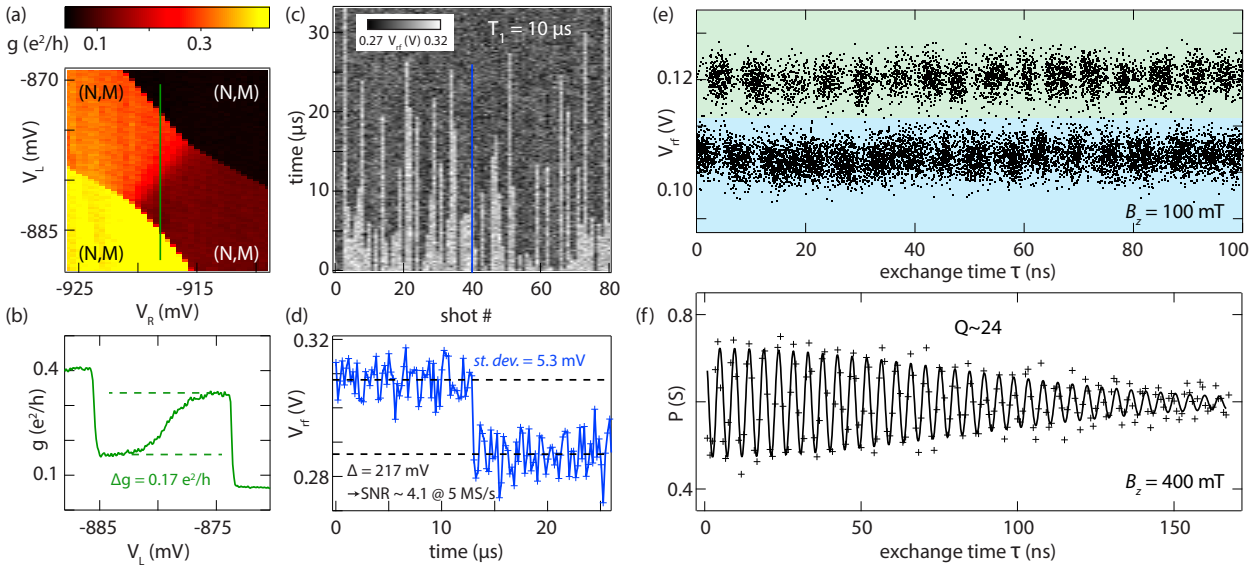

Figure 3.8: Charge sensing of a multi-electron double quantum dot and single-shot qubit readout. (a) Stability diagram near the (4,4)-(3,5) transition acquired by standard locking detection of the zero-bias conductance of the sensor quantum dot (*rms* excitation $\approx 10\ \mu$V). Plunger gate voltages V_{R} and V_{L} are defined as in [130, Fig. 3.1(a)]. (b) Cut along vertical line indicated in (a), revealing the sensitivity of the sensor conductance to the interdot transition. (c) Single-shot traces obtained by radio-frequency reflectometry. Each vertical trace shows the demodulated sensor signal V_{rf} after bringing a triplet-initialized qubit state to its measurement point. (d) Sensor signal when reading out shot #40 indicated in (c), demonstrating a qubit readout signal-to-noise ratio of 4.1 for an integration subinterval of 200 ns. (e) 12100 consecutive single-shot measurements of V_{rf} using the pulse sequence sketched in Fig. 3.1(b) with integration subinterval of 750 ns and exchange time τ incremented every 100 cycles. (f) Thresholding data similar to (e), the singlet return probability $P(S)$ reveals a high-Q exchange oscillation. Each data point was calculated from an ensemble of 1000 single-shot outcomes obtained at B=400 mT. Note: Panel (a) and (b) can be directly compared to analogous, previous work on (1,1) dot occupations in an lithographically identical device [130, Figs. 2(a,c)]. Multi-electron single-shot data in panels (c-e) can be compared with [93, Figs. 1(d), 2(a)].

(∼0.15 mV) [130].

We note that the possibility of single-shot readout may facilitate qubit initialization in multi-electron double quantum dots. Unlike the (1,1) singlet, which can easily be initialized by temporarily emptying the left dot (0,1), and reloading the right dot (0,2), a multi-electron singlet in ($2n$+1, $2m$+1) can be more complicated to achieve: Pulsing into ($2n$, $2m$+1) may result in an excited state of the left dot with high total spin and long relaxation time, resulting in an unknown state even if the right dot is subsequently loaded in a singlet configuration. Single-shot readout alleviates these concerns in two ways. First, because data are only acquired during the readout step, we are are able to initialize for a sufficiently long time without decreasing the signal-to-noise ratio. Second, single-shot data are naturally normalized by counting shot-by-shot, allowing one to accurately detect preparation infidelities.

High quality-factor exchange oscillations measured in single-shot mode are demonstrated in Figs. 3.8(e, f). Panel (e) shows 12100 consecutive single-shot measurements of V_{rf} using the pulse sequence sketched in Fig. 3.8(b). In this sequence τ is varied from 0 to 100 ns, with each τ value repeated 100 times. Each point in Fig. 3.8(e) is identified as either singlet or triplet based on a simple threshold criterion (blue and green regions in Fig. 3.8(e)) [93]. By counting the number of singlet occurrences for each τ value, a singlet return probability can then be determined. This is done in Fig. 3.8(f) for a similar data set with 1000 repetitions to reduce shot noise. A sinusoidal fit with a Gaussian envelope yields a quality factor $Q \sim 24$.

3.9 Measurement of $T^*_{2,\mathrm{n}}$ for (1,1) and (7,5) dot occupations

In order to quantify the amount of nuclear noise for each electron occupation, we employ a dephasing pulse sequence (inset of Fig. 3.9) that directly measures the inhomogeneous dephasing time, $T^*_{2,\mathrm{n}}$. For (1,1), a singlet-correlated pair of spins is initialized in (0,2) and separated quickly (compared to $1/T^*_{2,\mathrm{n}}$) deep into (1,1). During the separation time, τ_S, the two separated spins accumulate a relative phase due to the fluctuating nuclear gradient, δh^z. The singlet return probability, $P(S)$, is found by averaging over many cycles of this pulse sequence, thus many values of δh^z. We find that the strength of nuclear spin fluctuations for (7,5) $1/T^*_{2,\mathrm{n}} = 0.11$ GHz is similar to that of (1,1), $1/T^*_{2,\mathrm{n}} = 0.13$ GHz. These values were used as input parameters for the Γ_Σ and Γ_n fits in Figs. 3(c, d).

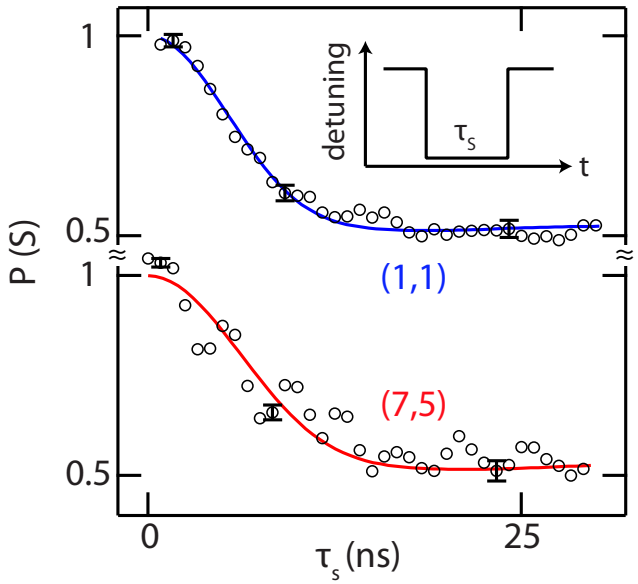

Figure 3.9: Measured singlet return probability $P(S)$ as a function of separation time τ_S (open circles) using a pulse sequence designed to probe the inhomogeneous dephasing time, $T^*_{2,\mathrm{n}}$, due to nuclear spins (inset). Gaussian fits (solid lines) yield $T^*_{2,\mathrm{n}} = 7.5$ ns for (1,1) occupation and a comparable number, $T^*_{2,\mathrm{n}} = 8.7$ ns, for (7,5) occupation. The applied magnetic field was $B = 0.05$ T.

3.10 Conclusion

In conclusion, we have compared noise-sensitive exchange oscillations in single- and and multi- electron spin qubits. The multi-electron dots are subject to less exchange noise than single-electron dots both because of a lowered noise susceptibility, $dJ/d\varepsilon$, and a lower rms noise value, $\delta\varepsilon$. Our observation of high-quality exchange oscillations between multiply-occupied dots suggests a route to simplifying device fabrication while simultaneously improving performance. It is worth emphasizing that the true source of the detuning-equivalent ε noise is not clear, but that is probably does not arise form the gates themselves. In addition, there is a dephasing source, Γ_0, which has both unknown origin and is non-detuning-equivalent. One possibility is that it arises from transverse electric fields effecting the tunnel-coupling of the device. We have also demonstrated single-shot readout and nuclear dephasing in the multi-electron regime, finding similar results to the single-electron case. In general, multi-electron qubits are provide similar functionality to the single-electron case, but with enhanced electrical noise performance.

4

Quasiparticles in an Al-InAs quantum dot

This chapter describes Coulomb blockade experiments on an Al-InAs quantum dot. The bulk of the chapter also appears in Ref. [132], co-written with Sven Albrecht. The devices were fabricated by Sven Albrecht, and measured in collaboration with him under the supervision of Charles Marcus. Willy Chang, Ferdinand Kuemmeth, and Thomas Jespersen assisted with the experiments, and theory work was performed by Gediminas Kiršanskas and Karsten Flensberg. The nanowires were grown by Peter Krogstrup. Leonid Glazman, Bert Halperin, Roman Lutchyn and Jukka Pekola gave helpful comments while the work in this chapter was being prepared for publication.

4.1 Introduction

Quasiparticle excitations can compromise the performance of superconducting devices, causing high frequency dissipation, decoherence in Josephson qubits [133–138], and braiding errors in proposed Majorana-based topological quantum computers [139–141]. Quasiparticle dynamics have been studied in detail in

metallic superconductors [142–146] but remain relatively unexplored in semiconductor-superconductor structures, which are now being intensely pursued in the context of topological superconductivity.

Quantum dots are useful for studying quasiparticles; a large charging energy can make single-quasiparticle occupation energetically favorable, allowing the "injection" of quasiparticles with a gate voltage. At zero bias, the equilibrium properties of quasiparticles can be tested, and at finite bias the dynamics become important.

To study the physics of quasiparticles in a Majorana system, we introduce an Al-InAs quantum dot comprising a gate-confined semiconductor nanowire with an epitaxially grown superconductor layer, yielding an isolated, proximitized nanowire segment. Bound states in the semiconductor are identified via bias spectroscopy, determine the characteristic temperatures and magnetic fields for quasiparticle excitations, and extract a parity lifetime (poisoning time) of the bound state in the semiconductor exceeding 10 ms.

Semiconductor-superconductor hybrids have been investigated for many years [147–151], but recently have received renewed interest in the context of topological superconductivity, motivated by the realization that combining spin-orbit interaction, Zeeman splitting and proximity coupling to a conventional s-wave superconductor provides the necessary ingredients to create Majorana modes at the ends of a one-dimensional (1D) wire. Such modes are expected to show nonabelian statistics, allowing, in principle, topological encoding of quantum information [15, 16, 152] among other interesting effects [153, 154].

Transport experiments on semiconductor nanowires proximitized by a grounded superconductor have recently revealed characteristic features of Majorana modes [18, 155]. Semiconductor quantum dots with superconducting leads have also been explored experimentally [156–159], and have been proposed as a basis for Majorana chains [160–162]. Here, we expand the geometries investigated in this context by creating an isolated semiconductor-superconductor hybrid quantum dot (HQD) connected to normal leads. The device forms the basis of an isolated Majorana system with protected total parity, where both the semiconductor nanowire and the metallic superconductor are mesoscopic [163, 164].

4.2 Experimental Setup

The measured device consists of an InAs nanowire with epitaxial superconducting Al on two facets of the hexagonal wire, with Au ohmic contacts (Figs. 4.1a,b), forming a normal metal-superconductor-normal

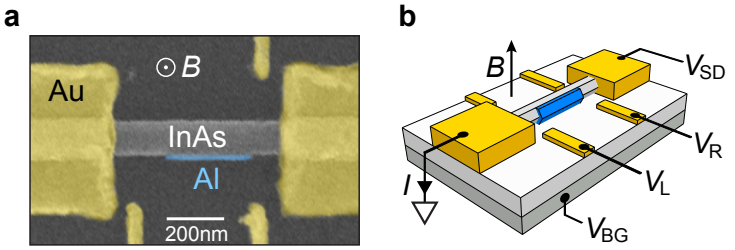

Figure 4.1: **a**, Scanning electron micrograph of the reported device, consisting of an InAs nanowire (gray) with segment of epitaxial Al on two facets (blue) and Ti/Au contacts and side gates (yellow) on a doped silicon substrate. **b**, Device schematic and measurement setup, showing orientation of magnetic field, B.

metal (NSN) device. The nanowires were grown in the [001] direction with wurzite crystal structure and the Al was matched to [111] on two of the six $\{1\bar{1}00\}$ sidefacets. They were then deposited randomly onto a doped silicon substrate with 100 nm of thermal oxide, followed by electron-beam lithographically patterned wet etch of the epitaxial Al shell (Transene Al Etchant D, 55 C, 10 s) resulted in a submicron Al segment (310 nm, Fig. 4.3a). Ti/Au (5/100 nm) ohmic contacts were then deposited on the ends following *in situ* Ar milling (1 mTorr, 300 V, 75 s), with side gates deposited in the same step. For the present device, the end of the upper left gate broke off during processing. However, the device could be tuned well without it. Four devices showing similar behavior have been measured.

Differential conductance, g, was measured in a dilution refrigerator with base electron temperature $T \sim 50$ mK using standard ac lock-in techniques. Local side gates, patterned with electron beam lithography, and a global back gate were adjusted to form an Al-InAs HQD in the Coulomb blockade regime, with gate-controlled weak tunneling to the leads. The lower right gate, V_{R}, was used to tune the occupation of the dot, with a linear compensation from the lower left gate, V_{L}, to keep tunneling to the leads symmetric. We parameterize this with a single effective gate voltage, V_{G}, related to the actual gate voltage V_{L} and V_{R} by

$$V_{\mathrm{R}} = V_{R,0} + \kappa V_{\mathrm{G}},$$
$$V_{\mathrm{L}} = V_{L,0} + \sqrt{1-\kappa^2}V_{\mathrm{G}},$$

with $\kappa = 0.9997$ and offset voltages $V_{R,0} = -2.41$ V, $V_{L,0} = -3.96$ V. These transformation rules ensure that $V_G^2 = (V_R - V_{R,0})^2 + (V_L - V_{L,0})^2$, so that V_G can be interpreted as the distance from $(V_{R,0}, V_{L,0})$ in the $V_R - V_L$ plane. All measurements are performed at backgate voltage $V_{\mathrm{BG}} = 2.39$ V.

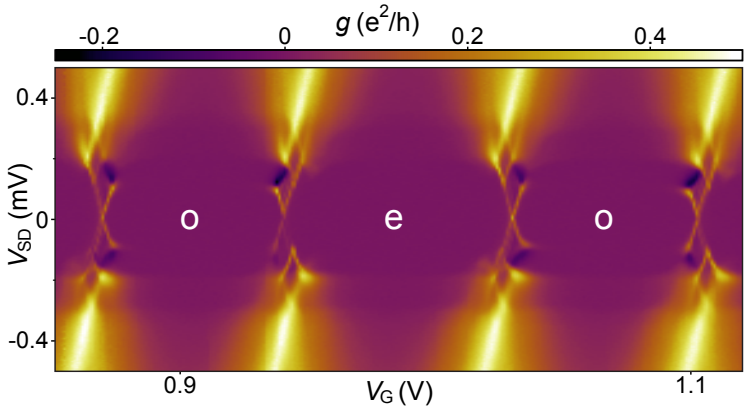

Figure 4.2: Differential conductance, g, as a function of effective gate voltage, V_G, and source-drain voltage, V_{SD}, at $B = 0$. Even (e) and odd (o) occupied Coulomb valleys labeled.

4.3 Coulomb blockade

Differential conductance as a function of V_G and source-drain bias, V_{SD}, reveals a series of Coulomb diamonds, corresponding to incremental single-charge states of the HQD (Fig. 4.2). While conductance features at high bias are essentially identical in each diamond, at low bias, $V_{SD} < 0.2$ mV, a repeating even-odd pattern of left- and right-facing conductance features is observed. This results in an even-odd alternation of Coulomb blockade peak spacings at zero bias, similar to even-odd spacings seen in metallic superconductors [25, 165]. However, the parity-dependent reversing pattern of subgap features at nonzero bias has not been reported before, to our knowledge. The repeating even-odd pattern indicates that a parity-sensitive (but otherwise relatively invariant) bound state is being repeatedly filled and emptied as electrons are added to the HQD.

Measured charging energy, $E_C = 1.1$ meV, and superconducting gap, $\Delta = 180$ μeV, satisfy the condition ($\Delta < E_C$) for single electron charging [166, 167]. Differential conductance at low bias occurs in a series of narrow features symmetric about zero bias, suggesting transport through a bound state, with negative differential conductance (NDC) observed at the border of odd diamonds. NDC arises from slow quasiparticle escape, as discussed below, similar to current-blocking seen in metallic superconducting islands in the opposite regime, $\Delta > E_C$ [168, 169].

To gain quantitative understanding of these features, we present a simple model of transport through a single bound state in the InAs plus a Bardeen-Cooper-Schriffer (BCS) continuum in the Al. The model

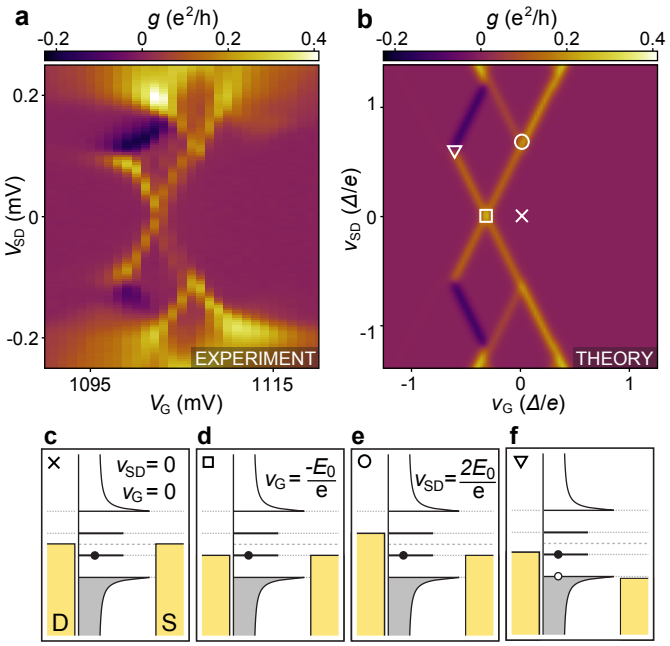

Figure 4.3: **a**, Experimental differential conductance, g, as a function of gate voltage V_{G} and source-drain V_{SD}, shows characteristic pattern including negative differential conductivity (NDC). **b**, Transport model of **a**. $v_{\mathrm{G}} = \alpha V_{\mathrm{G}}$ up to an offset, where α is the gate lever arm. Axis units are $\Delta/e = 180$ μV, where Δ is the superconducting gap. See text for model parameters. **c**, Source and drain (gold) chemical potentials align with the middle of the gap in the HQD density of states. No transport occurs due to the presence of superconductivity. **d**, Discrete state in resonance with the leads at zero bias. Transport occurs through single quasiparticle states. **e**, Discrete state in resonance with the leads at high bias. Transport occurs through single and double (particle-hole) quasiparticle states. **f**, Discrete state and BCS continuum in the bias window. Transport is blocked when a quasiparticle is in the continuum, resulting in NDC.

makes several simplifying assumptions: symmetric coupling of both the bound state and continuum to the leads, motivated by the observed symmetry in V_{SD} of the Coulomb diamonds, and a fixed-energy bound state, motivated by the repetitive pattern observed in the Coulomb diamonds as well as the expectation that the Al dominates the gate-dot capacitance. Transition rates were calculated from Fermi's golden rule and a steady-state Pauli master equation was solved for state occupancies. The master equations consider states with fixed total parity, composed of the combined parity of quasiparticles in the thermalized continuum and the 0, 1, or 2 quasiparticles in the bound state. Conductance was then calculated from occupancies and transition rates (see Ref. [132] supplement for theory details).

Measured and model conductances are compared in Figs. 4.3a,b. The coupling of the bound state to each lead, noting the near-symmetry of the diamonds, was estimated to be $\Gamma_0 = 0.5$ GHz, based on zero-bias conductance (Fig. 4.3d). The energy of the discrete state, $E_0 = 58$ μeV at zero magnetic field, was measured using finite bias spectroscopy (Fig. 4.3e). The normal-state conductance from each lead to the continuum, $g_{\mathrm{Al}} = 0.15\ \mathrm{e}^2/\mathrm{h}$, was estimated by comparing Coulomb blockaded transport features in the high bias regime ($V_{\mathrm{SD}} = 0.4$ mV). The superconducting gap, $\Delta = 180$ μeV, was found from the onset of NDC, which is expected to occur at $eV_{\mathrm{SD}} = \Delta - E_0$ (Fig. 4.3f). While the rate model shows good agreement with experimental data, some features are not captured, including broadening at high bias, with greater broadening correlated with weaker NDC, and peak-to-peak fluctuations in the slope of the NDC feature. These features may be related to heating or cotunneling, not accounted for by the model.

To increase intuition for the rate model, it is useful to interpret each Coulomb diamond conductance threshold, as shown in Fig. 4.4. For example, the highest bias at which NDC is observed occurs is $v_{\mathrm{SD}} = (\Delta + E_0)/e$, at the intersection of black and green lines.

4.3.1 Implications of negative differential conductance

The observation of negative differential conductance places a bound on the relaxation rate of a single quasiparticle in the HQD from the continuum (in the Al) to the bound state (in the InAs nanowire). Negative differential conductance arises when an electron tunnels into the weakly coupled BCS continuum, blockading transport until it exits via the lead. The blocking condition is shown for a hole-like excitation in Fig. 4.3f. Unblocking occurs when the single quasiparticle relaxes into the bound state, followed by a

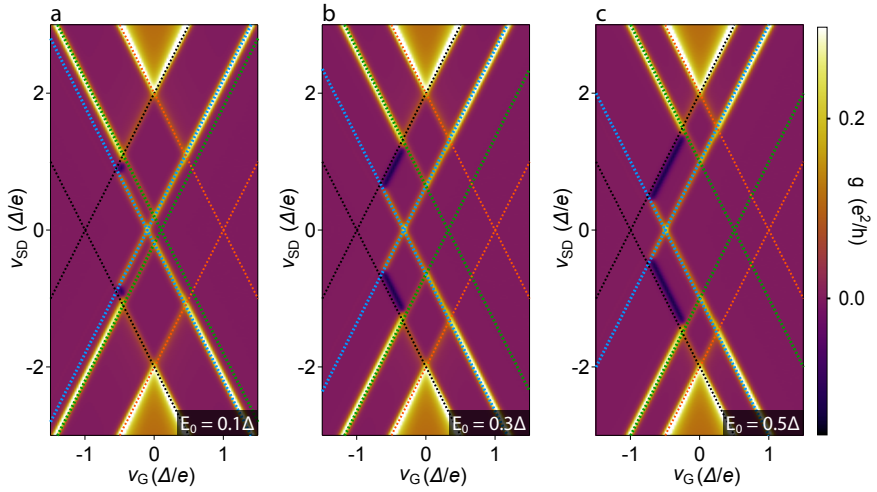

Figure 4.4: **a**, Calculated conductance g versus v_{SD} and v_G. $E_0 = 0.1\Delta$, all other model parameters same as Fig. 4.3 Dotted lines are $v_{SD}/2 = \pm(v_G + \Delta/e)$ [black], $v_{SD}/2 = \pm(v_G + E_0/e)$ [blue], $v_{SD}/2 = \pm(v_G - E_0/e)$ [green], $v_{SD}/2 = \pm(v_G - \Delta/e)$ [red]. **b**, $E_0 = 0.32\Delta$, all model parameters same as main text. **c**, $E_0 = 0.5\Delta$, all other model parameters same as main text. Color scale shared across all plots.

fast escape to the leads. When the typical time for quasiparticle relaxation is shorter than characteristic transport timescales, the NDC is predicted to disappear, as shown in Fig. 4.5. NDC thus indicates a long quasiparticle relaxation time, τ_{qp}, from the continuum to the bound state.

The depth strength of NDC is quantified by introducing the relative conductance ratio

$$R = \frac{g' + g_{NDC}}{g' - g_{NDC}} \tag{4.1}$$

where g_{NDC} is the minimum of the negative differential conductance, and g' is the maximum of the extra conductance threshold that appears when $\tau_{qp} \to 0$ (see Fig. 4.5). Figs. 4.5f-j shows example conductance traces at constant bias and the associated R-values. The traces show that $R \approx -1$ corresponds to slow quasiparticle relaxation, and $R \approx 1$ corresponds to fast quasiparticle relaxation.

The data give $R = 0.85 \pm 0.1$, found by averaging over all negative differential conductance features in Fig. 4.2. The measured R-value is consistent with $\tau_{qp} > 0.1$ µs, as shown in Fig. 4.6, giving the experimental bound on the single quasiparticle relaxation time.

Thus, using independently determined parameters, the observed NDC is only compatible with the model when $\tau_{qp} > 0.1$µs.

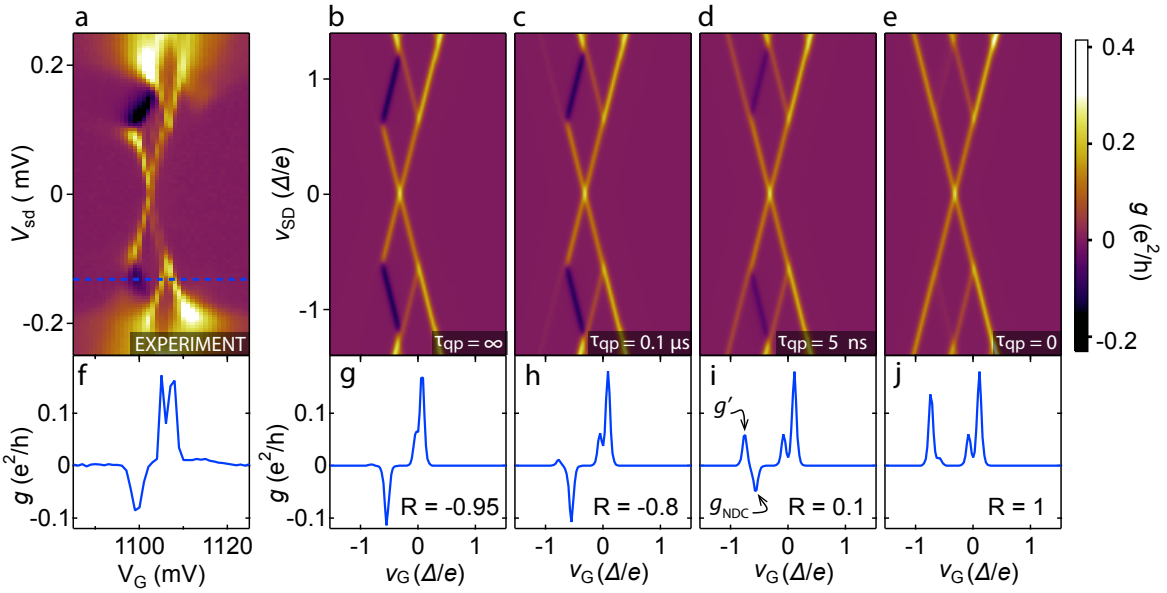

Figure 4.5: **a** Measured conductance g versus source-drain bias $V_{\rm SD}$ and gate $V_{\rm G}$. **b**, Transport model of **a**, with $\tau_{\rm qp} = \infty$. $v_{\rm G} \equiv \alpha V_{\rm G}$ up to an offset, where α is the gate lever arm. Axis units are $\Delta/e = 180\mu$V. **c-e**, Model with $\tau_{\rm qp} = 0.1\mu$s, $\tau_{\rm qp} = 5$ns, and $\tau_{\rm qp} = 0$ respectively. **f-j**, Conductance versus gate at constant bias indicated in **a**. Relative conductance ratio, $R = (g' + g_{\rm NDC})/(g' - g_{\rm NDC})$, for theory curves is labeled (see text).

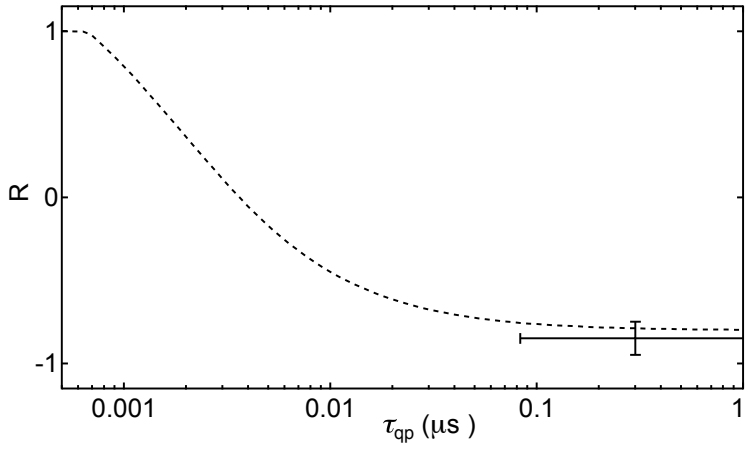

Figure 4.6: Relative conductance ratio, $R = (g' + g_{\rm NDC})/(g' - g_{\rm NDC})$, versus single quasiparticle relaxation time $\tau_{\rm qp}$. Dashed curve is theory derived as shown in Fig. S1. Data is the average over all charge transitions in Fig. 1, with vertical error the standard deviation of the mean, and horizontal error propagated from vertical.

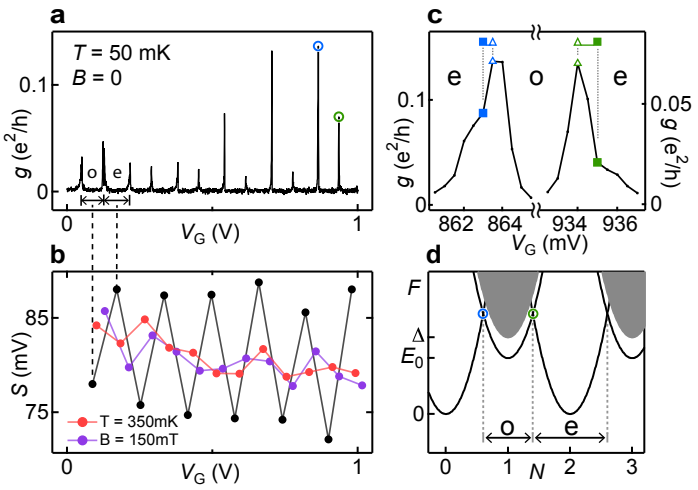

Figure 4.7: **a**, Measured zero-bias conductance, g, versus gate voltage, V_G, at temperature $T \sim 50$mK, and magnetic field $B = 0$. **b**, Peak spacing, S, versus gate voltage. Black points show spacings from **a** calculated using the peak centroid (first moment), red points $T = 350$mK and $B = 0$, purple points $B = 150$mT and $T \sim 50$mK. **c**, Right-most peaks in **a**. Peak maxima (△) and centroids (■) are marked. **d**, Free energy, F, at $T = 0$ versus gate-induced charge, N, for different HQD occupations, where $N = CV_G/e$ up to an offset and C is the gate capacitance. Parabola intersection points are indicated by circles, corresponding to Coulomb peaks. BCS continuum (shaded), shown for odd occupancy. Odd Coulomb diamonds carry an energy offset E_0 for quasiparticle occupation of the sub gap state, resulting in a difference in spacing for even and odd diamonds.

4.4 Zero-bias data

Turning our attention to the even-odd structure of zero-bias Coulomb peaks (Figs. 4.7a,b), we observed consistent large-small peak spacings, associating the larger spacings with even occupation, as expected theoretically [166, 167] and already evident in Fig. 4.2. Occasional even-odd parity reversals on the timescale of hours were observed in some devices, similar to what is seen in metallic devices [146]. Peak spacing alternation disappears at higher magnetic fields, B, consistent with the superconducting-to-normal transition, and also disappears at elevated temperature, $T > 0.4$K, significantly below the superconducting critical temperature, $T_c \sim 1$K. The temperature dependence is consistent with similar behavior seen in metallic structures [25, 165], and can be understood as the result of thermal activation of quasiparticles within the HQD with fixed total charge.

As seen in Fig. 4.7c, individual Coulomb peaks are asymmetric in shape, with their centroids (first moments) on the even sides of the peak maxima. Note that the asymmetry leads to higher near-peak conductance in *even* valleys, the opposite of the Kondo effect. The asymmetric shape is most pronounced at low temperature, $T < 0.15$K, and decreases with increasing magnetic field. The degree of asymmetry is not

predicted by the rate model, even taking into account the known small asymmetry due to spin degeneracy [22]. In the analysis below, we consider peak positions defined both by peak maxima and centroids.

A model of even-odd Coulomb peak spacing that includes thermal quasiparticle excitations follows earlier treatments [25, 165, 167], including a discrete subgap state as well as the BCS continuum [25] (Fig. 4.7d). Even-odd peak spacing difference, $S_e - S_o$, depends on the difference of free energies,

$$S_e - S_o = \frac{4}{\alpha e}\left(F_o - F_e\right), \tag{4.2}$$

where α is the (dimensionless) gate lever arm. The free energy difference, written in terms of the ratio of partition functions is,

$$F_o - F_e = -k_B T \ln\left(\frac{Z_o}{Z_e}\right). \tag{4.3}$$

For even-occupancy,

$$Z_e = 1 + \sum_{i \neq j} e^{-E_i/k_B T} e^{-E_j/k_B T} + \ldots, \tag{4.4}$$

where the first term stands for zero quasiparticles, the second for two (at energies E_i and E_j), and additional terms for four, six, etc. Z_o similarly runs over odd occupied states. Rewriting the sums of Boltzmann factors as integrals over the density of states, $D(E)$, gives

$$\frac{Z_o}{Z_e} = \int_0^\infty \mathrm{d}E\, D(E) \ln \coth[E/(2k_B T)], \tag{4.5}$$

where $D(E)$ consists of one subgap state and the continuum,

$$D(E) = \rho_{BCS}(E) + \frac{1}{2}\rho_0^+(E) + \frac{1}{2}\rho_0^-(E). \tag{4.6}$$

We take $\rho_{BCS}(E)$ to be a standard BCS density of states,

$$\rho_{BCS}(E) = \frac{\rho_{Al} V E}{\sqrt{E^2 - \Delta(B)^2}}\theta(E - \Delta) \tag{4.7}$$

(θ is the step function), and ρ_0 to be a pair of Lorentzian-broadened spinful levels symmetric about zero,

$$\rho_0^{\pm}(E) = \frac{\gamma/2\pi}{(E - E_0^{\pm})^2 + (\gamma/2)^2} + \frac{\gamma/2\pi}{(E + E_0^{\pm})^2 + (\gamma/2)^2}. \tag{4.8}$$

Zeeman splitting of the bound state and pair-breaking by the external magnetic field are modeled with the equations

$$E_0^{\pm}(B) = \frac{\Delta(B)}{\Delta} E_0 \pm \frac{1}{2} g\mu_B B, \tag{4.9}$$

$$\Delta(B) = \Delta\sqrt{1 - \left(\frac{B}{B_c}\right)^2}, \tag{4.10}$$

where E_0 is the zero-field state energy and Δ is the zero field superconducting gap. In the event that a bound state goes above the continuum, $E_s^+ > \Delta(B)$, we no longer include the state in the free energy. Equations (4.9) and (4.10) are reasonable provided the lower spin-split state remains at positive energy, $E_0^- > 0$. For sufficiently large B_c, the bound state will reach zero energy, resulting in topological superconductivity and Majorana modes, the subject of future work.

For $\Delta \gg k_B T$, the Free energy can be approximated

$$F_o - F_e \approx -k_B T \ln(N_{\text{eff}} e^{-\Delta/k_B T} + 2e^{-E_0/k_B T}), \tag{4.11}$$

where $N_{\text{eff}} = \rho_{\text{Al}} V_{\text{Al}} \sqrt{2\pi k_B T \Delta}$ is the effective number of continuum states for Al with volume V_{Al} and electron density of states ρ_{Al} [25, 165] (see Appendix B for discussion of approximations).

Based on Eq. 4.11, one can identify a characteristic temperature, $T^* \sim \Delta/[k_B \ln(N_{\text{eff}})]$, less than the gap, above which even-odd peak spacing alternation is expected to disappear. Note in this expression N_{eff} itself depends on T, and also that T^* does not depend on the bound state energy, E_0. A second (lower) characteristic temperature, $T^{**} \sim (\Delta - E_0)/[k_B \ln(N_{\text{eff}}/2)]$, which does depend on E_0, is where the even-odd alternation is affected by the bound state, leading to saturation at low temperature [25, 165]. For a spin-resolved zero-energy ($E_0 = 0$) bound state—the case for unsplit Majorana zero modes—these characteristic temperatures coincide and even-odd structure vanishes, as pointed out in Ref. [163]. In the opposite case, where the bound state reaches the continuum ($E_0 = \Delta$), the saturation temperature vanishes, $T^{**} = 0$, and

the metallic result with no bound state is recovered [25, 165].

Experimentally, the average even-odd peak spacing difference, $\langle S_e - S_o \rangle$, was determined by averaging over a set of 24 consecutive Coulomb peak spacings, including those shown in Fig. 4.7, at each temperature. Figure 4 shows even-odd peak spacing difference appearing abruptly at $T_{onset} \sim 0.4$ K, and saturating at $T_{sat} \sim 0.2$ K, with a saturation amplitude near the value expected from the measured bound state energy, $4V_0 = 4E_0/(\alpha e)$. Figure 4 shows good agreement between experiment and the numerically-integrated model, Eq. (4.2), using a density-of-states parameters determined independently from data in Fig. 4.3, with $V = 7.4 \times 10^4 \text{nm}^3$ as a fit parameter, consistent with the micrograph (Fig. 4.1a), and $\rho_{Al} = 23\text{eV}^{-1}\text{nm}^{-3}$ [146].

The asymmetric peak shape complicates measurement of even-odd spacings, as one can either use the centroids or maxima to measure spacings, the two methods giving different results. Larger peak tails on the even valley side cause the centroids to be more regularly spaced than the maxima. This is evident in Fig. 4.8, where the centroid method shows a decreasing peak spacing difference at low temperature, while with the maximum method the spacing remains flat. The thermal model of $S_e - S_o$ can also show a decrease at low temperature if broadening of the bound state is included. We do not understand at present if the low temperature decrease in the centroid data is related to the decrease seen in the model when broadening is included. It is worth noting, however, that the fit to the centroid data gives a broadening $\gamma = 50\text{neV}$, reasonably close to the value estimated from the lead couplings, $(h\Gamma_0)^2/\Delta = 20\text{neV}$.

Applied magnetic field (direction shown in Fig. 4.3b) reduces the characteristic temperatures T_{onset}, T_{sat}, and saturation amplitudes. Field dependence is modeled by including Zeeman splitting of the bound state and orbital reduction of the gap and bound state energy, taking the g-factor and critical magnetic field as two fit parameters applied to all data sets. The fit value $g = 6$ lies within the typical range for InAs nanowires [170, 171], supporting our interpretation that the bound state resides in the InAs. The fit value of critical field, $B_c = 120\text{mT}$, is typical for this geometry.

4.5 Number of quasiparticles

Agreement with the thermodynamic model suggests that ensemble averages of even-odd spacing, $S_e - S_o$, provides a measure of the equilibrium quasiparticle density, n_{qp}. Figure 4 (right axis) gives the value

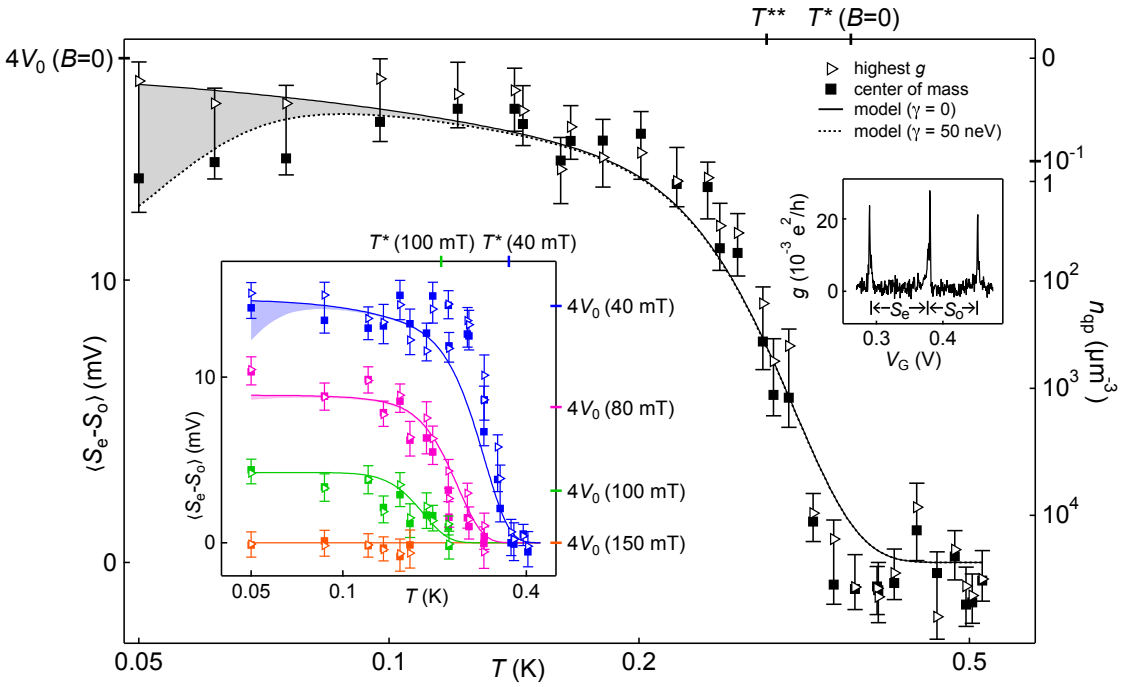

Figure 4.8: Average even-odd spacing difference, $\langle S_e - S_o \rangle$, versus temperature, T. Spacing between peak maxima (triangle) and centroids (square) are shown. Spacing expected from lower Zeeman-split bound state, $4V_0(B) = 4E_0(B)/(\alpha e)$ indicated. Quasiparticle activation temperature, T^*, and crossover temperature, T^{**}, indicated on top axis. Right axis shows calculated aluminum quasiparticle density, n_{qp} (see text). Solid curve is Eq. (4.2) with a HQD density of states measured from Fig. 4.3 ($\Delta = 180\mu eV$, $E_0 = 58\mu eV$, $\alpha = 0.013$), and the fitted aluminum volume, $V_{Al} = 7.4 \times 10^4 nm^3$. Dotted curve includes a discrete state broadening, $\gamma = 50neV$, fit to the centroid data. *Left inset:* Same as main, but at $B = 40, 80, 100, 150mT$, from top to bottom and $4V_0$ appearing on the right-hand axis. Curves are fit to two shared parameters: g-factor, $g = 6$, and superconducting critical field, $B_c = 120mT$, with other parameters fixed from main figure. *Right inset:* Representative Coulomb peaks showing even (S_e) and odd (S_o) spacings.

$n_{qp}(T) = V_{Al}^{-1} N_{eff}^2 e^{-2\Delta/k_B T}$, an expression valid for large charging energy [172] (see Appendix A). Note the factor of 2Δ in the exponent occurs because of of the strong Coulomb blockade limit $E_C > \Delta$; it reflects the fact that single quasiparticles are at energy $E_C + \Delta$ and thus "freeze out" before double-quasiparticle excitations at 2Δ

Below $T_{sat} \sim 0.2K$, even-odd spacing saturates at the bound-state value $4V_0$, as expected, making it difficult to infer a quasiparticle density in this low-temperature range. Instead, we conservatively take $n_{qp}(T_{sat}) \sim 0.1\mu m^{-3}$ as an upper bound for the quasiparticle density at low temperature. This value is within the range from the recent literature, $0.03 - 30\mu m^{-3}$ [135–138, 145]. Because the volume of Al is small in this device geometry, the upper bound on the number of quasiparticles, $n_{qp} V_{Al} < 10^{-5}$, is, correspondingly, quite small.

4.5.1 Discussion

Using the results of this chapter, we determine a lower bound on the poisoning time, τ_p, of the bound state. The physical mechanism for this poisoning is relaxation of a quasiparticle into the InAs from the Al, a process that preserves the overall parity of the isolated island (InAs plus Al) but changes the parity of the bound state. The process is intrinsic to the superconductor-semiconductor system, and is expected to set the fundamental limit on parity lifetime [140]. The poisoning rate, $1/\tau_p$, is given by the product of the relaxation rate of a single quasiparticle from the Al, $1/\tau_{qp}$, and the number of quasiparticles in the Al [140], which, from above, is bounded by $n_{qp}V_{Al} < 10^{-5}$. Quantitative comparison of transport data to the numerical model —in particular, the relative strength of negative differential conductivity at finite bias, which vanishes for fast quasiparticle relaxation—provides a lower bound on the quasiparticle relaxation time, $\tau_{qp} > 0.1\mu s$ (see Sec.4.3.1). Together, these values give a conservative lower bound on the poisoning time of the bound state, $\tau_p = \tau_{qp}/(n_{qp}V_{Al}) > 10ms$.

Quasiparticle density depends sensitively on device geometry, filtering, and shielding, resulting in a wide range of experimental values ($0.03 - 30\mu m^{-3}$), and thus poisoning times. We note that recent work in transmon qubits [145] found $n_{qp} = 0.04\mu m^{-3}$, corresponding to state-poisoning times well above 10ms. We also note that the Coulomb blockade geometry effectively enforces quasiparticles from the Al shell to be created only in pairs, which is different from non-charging device geometries.

Based on previous work, τ_{qp}, hence τ_p, is expected to depend weakly on the bound-state energy for low-energy bound states [143, 173, 174], including zero-energy Majorana modes with $E_0 = 0$. The long poisoning time found here, $\tau_p > 10ms$, is auspicious for application of this system to topological quantum computing, suggesting that a large number of braiding operations of Majorana modes could be performed before the parity of the bound state is poisoned by the proximitizing Al. Chapter 5 investigates the emergence of Majorana modes in this system.

5

Majorana quantum dot

This chapter presents magnetic field dependence of Coulomb peak spacings and heights in an Al-InAs quantum dot. It is a continuation of the study in Chapter 4, and most of the content will appear in a manuscript, currently in preparation. The devices were fabricated by Sven Albrecht, and measured in collaboration with him under the supervision of Charles Marcus. Morten Madsen, Willy Chang, Ferdinand Kuemmeth, and Thomas Jespersen assisted with the experiments. The nanowires were grown by Peter Krogstrup.

5.1 Introduction

Majorana modes are predicted to possess nonabelian braiding statistics, making them appealing for topological quantum computing [13, 175]. Braids are protected by pinning of the ground state to zero energy, which is ensured exponentially as the separation between Majorana modes is increased [176]. Following proposals [16, 177], several experiments have found signatures of Majorana modes at the ends of super-

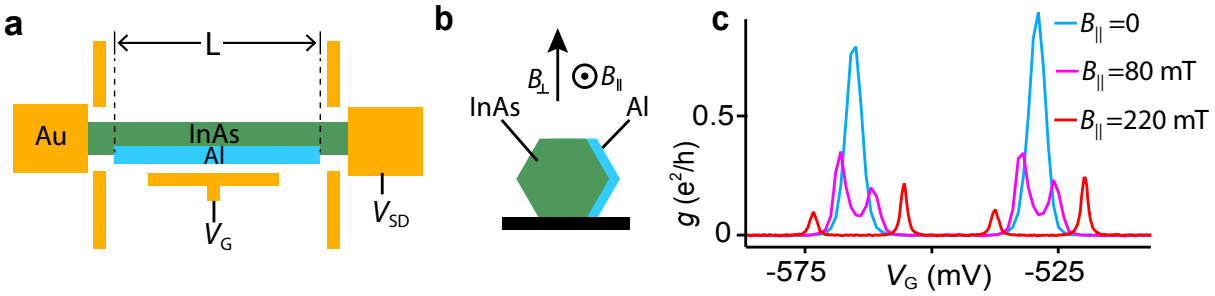

Figure 5.1: **a**, Diagram of device concept. Devices of different shell length, L, are measured. **b**, Schematic of nanowire cross-section showing high-critical-field directions $B_{||}$ and $B_\perp$. **c**, Measured conductance, g, versus gate voltage V_G at magnetic field $B_{||} = 0, 80, 220$ mT.

conducting nanowires [18, 155, 178–180] and atomic chains [181], with small mode-splitting potentially explained by hybridization of the Majoranas [182, 183]. Exponential robustness with increasing separation, corresponding to the disappearance of hybridization for distantly separated Majoranas, has yet to be experimentally tested.

This chapter reports the observation of exponentially suppressed energy splittings for zero-energy states in an isolated Majorana island. State energies are inferred from Coulomb peak spacings. For short devices, Coulomb peaks oscillate strongly, as expected for hybridized Majorana fermions. The amplitude of the oscillations decrease exponentially with device length, as expected for the exponential pinning of Majorana modes to zero energy. Coulomb peak heights increase when the putative Majorana state emerges, consistent with so-called electron teleportation by Majorana fermions [163].

The devices reported in this chapter are fabricated and measured using the same techniques as Chapter 4 [Fig. 5.1(a,b)]. The two salient differences are that the Al shell length, L is varied between 320 nm and 1.5 μm, and that the magnetic field is aligned to be in a direction giving large critical fields, in excess of 500 mT.

5.2 Experiment

Sweeping gate while measuring conductance reveals Coulomb peaks (Fig. 5.1c, $L = 790$ nm device). At zero field, the peaks are $2e$-periodic, which is a limiting case of the even-odd alternations in Chapter. 4. This regime is expected to occur when all single-particle states have sufficiently large energy, $\Delta > E_C$, causing the odd Coulomb valleys to shrink to zero width. Above a characteristic applied magnetic field B^*

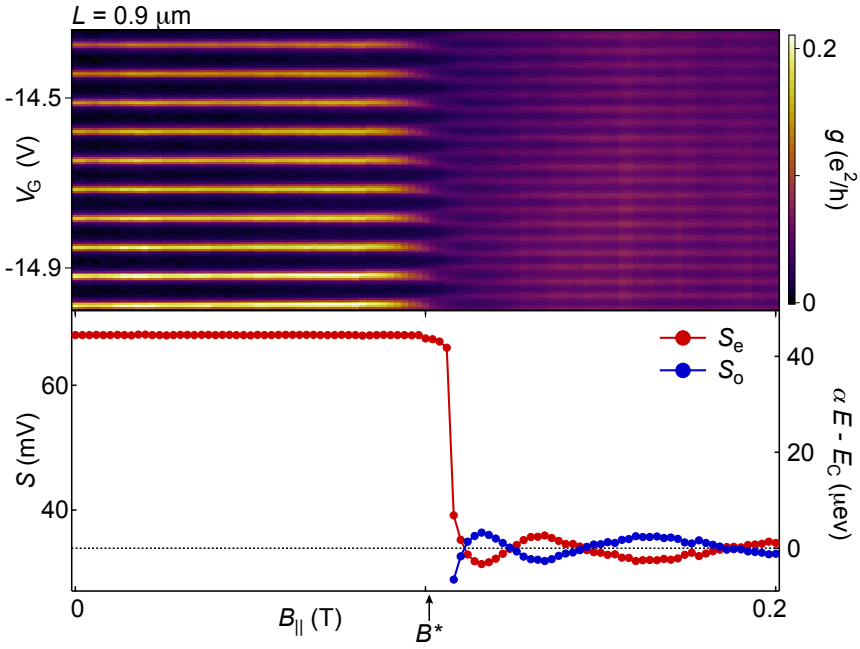

Figure 5.2: **a,** Conductance, g, as a function of gate voltage, V_G and magnetic field, $B_{||}$. **b,** Even valley width, S_e, and odd valley width, S_o versus magnetic field, extracted from **a**. Characteristic field, B^*, where peaks cross over from 2-electron to 1-electron charging, labeled.

the Coulomb peaks split, resulting in a pronounced even-odd structure ($B_{||} = 80$ mT, Fig. 5.1c). Splitting Coulomb peaks indicate the emergence of a new charge state, presumably due to the presence of at least one single-electron state satisfying $E_0 < E_C$. Further increasing magnetic field, the odd Coulomb valley continues to grow until the peaks are evenly spaced at a second characteristic field $B = B^{**}$. Under general considerations, evenly spaced peaks indicate that at least one state with zero single-particle energy is present. The simplest interpretation of these data is that a single-particle state emerges in finite field and moves to zero energy, which is consistent with the emergence of Majorana modes.

Sweeping gate and field while measuring conductance reveals more detailed behavior of the Coulomb peaks as a function of field (Fig. 5.2a, 900 nm device). At low field, when the peaks are $2e$-periodic there is essentially no field dependence. After splitting near $B^* = 100$ mT, the peaks become roughly $1e$ periodic. In the $1e$-regime, the Coulomb valleys exhibit a characteristic breathing fine-structure, where the width of odd and even valleys oscillates as a function of field. The oscillations are better resolved by extracting valley widths and averaging over even and odd valleys separately, as shown in Fig. 5.2b. The Coulomb valleys oscillate with a characteristic amplitude of a 4.5 mV in gate voltage, corresponding to an energy-oscillation of 7 μeV. It is worth emphasizing that the $2e$ to $1e$ transition and the Coulomb valley oscillations occur far

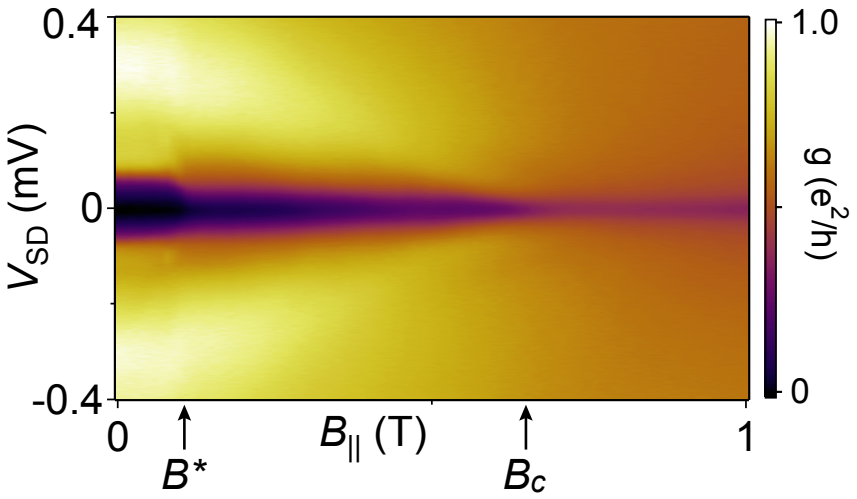

Figure 5.3: Conductance, g, as a function of source-drain bias, voltage V_{SD}, and magnetic field, $B_{||}$. Characteristic field B^* (cf. Fig. 5.2), and superconducting critical field, B_C labeled. Note that $B^* \ll B_C$.

before the normal-state transition, as shown in Fig. 5.3

In the Majorana picture, oscillations with magnetic field – due to residual overlap of Majorana wavefunctions – are expected to be exponentially suppressed as wire length increases. To test this prediction, we measure Coulomb peak oscillations in devices of five different lengths, shown in Fig. 5.4. In every measured device, Coulomb peaks are $2e$-periodic at $B = 0$ — even-odd for $L = 320$ nm, 400 nm and $2e$-charging for $L = 790$ nm, 0.9 μm, 1.5 μm — reflecting the fact that the superconductor distinguishes between even and odd total parity. At a device-dependent B^{**}, between 100 mT and 300 mT, Coulomb peaks become $1e$ periodic. For larger fields, $B > B*$, even and odd valley width oscillate as a function of field, as already discussed for the $L = 0.9$ nm device.

From Fig. 5.4 it is already clear that the energy associated with even-odd valley oscillations *decreases* as *L increases*, qualitatively agreeing with the Majorana expectation. To quantify the dependence of oscillation amplitude, A, on device length we measure the characteristic oscillation amplitude for each device, as indicated in Fig. 5.4d. [*]

The measured oscillation amplitudes, A, shown in Fig. 5.5, are consistent with the exponential dependence on length, $A_0 e^{-L/\xi}$. The fit Majorana coherence length, $\xi = 250$ nm, is reasonable given known InAs material parameters [155]. Thus, the data are consistent with modes localized on the wire ends. The

[*]For $L = 320$ nm, Coulomb peak fluctuations became uncorrelated after several peaks. In that case, fluctuations were averaged over five sets of Coulomb peaks taken in different device tunings, and Fig. 5.4a shows data from a single set of peaks. For all other device lengths, A is extracted directly from Fig.'s 5.4(b-e).

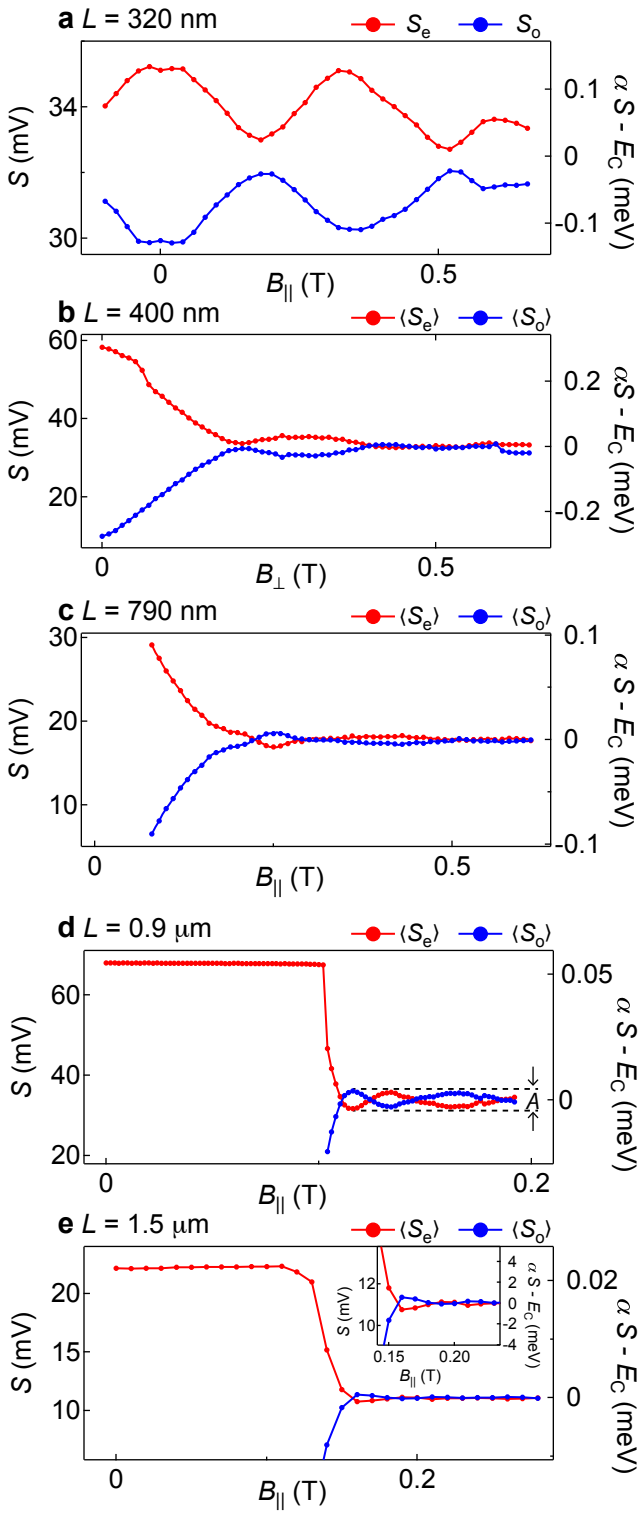

Figure 5.4: Even valley width, S_e, and odd valley width, S_o versus magnetic field, extracted from Coulomb peaks similar to Fig. 5.2, for device lengths **a**, $L = 320$ nm **b**, $L = 400$ nm **c**, $L = 790$ nm **d**, $L = 0.9$ μm **e**, $L = 1.5$ μm. Characteristic oscillation amplitude A labeled in **d**.

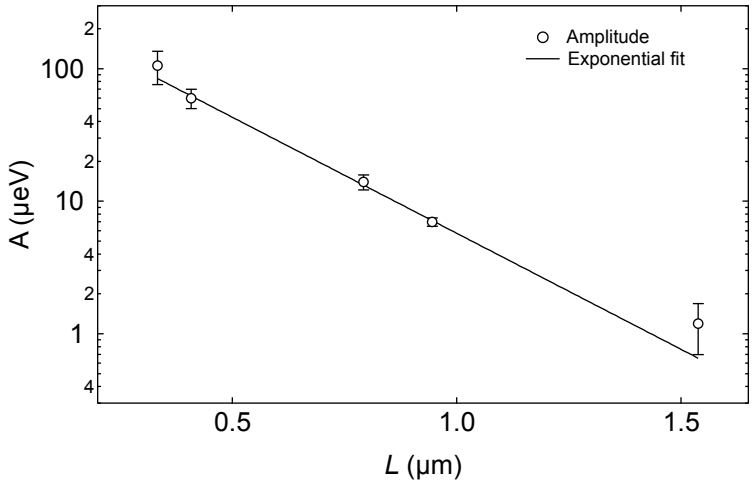

Figure 5.5: Oscillation amplitude, A, versus device length L. Fit is to the exponential form $A_0 e^{-L/\xi}$ with $A_0 = 310$ μeV, $\xi = 250$ nm.

observed exponential suppression constitutes an experimental test of the robustness; B-field perturbations are exponentially suppressed as the wire length is increased. It should be noted, however, that the smallest splitting measured here, $A \sim 1\,\mu\text{eV} = h \cdot 250$ MHz, is still very large as far as time-domain braiding experiments are concerned.

We conclude our discussion of Coulomb peak spacings, and turn attention to Coulomb peak heights. As discussed in Chapter 1, Coulomb peak heights are proportional to wavefunction norms at both leads [22, 24], and therefore some indication of wavefunction shape. Comparing Coulomb peak heights for different device lengths (Fig. 5.6) shows that a region of strongly suppressed peak height develops in long devices at intermediate fields $B^* < B < B^{**}$, with weak peak height fluctuations at higher field. We found that this effect occurs only in the weak-coupling regime; indeed, the data in Fig. 5.2 do not display this effect and are with stronger coupling to the leads. The onset of suppressed conductance at B^* coincides with the crossover from Cooper pair to single-electron charging, suggesting that single-electron states are decoupled from the leads below B^{**}. Strong brightening of peaks at B^{**}, coincident with the onset of $1e$-periodicity, is consistent with the emergence of a zero-energy state with enhanced wavefunction weight at the leads, as predicted by the Majorana teleportation picture [163]. Brightening would also be observed, however, if localized, zero-energy, single-particles states were present on each end [184]; numerical simulations of the system may help distinguish the two cases.

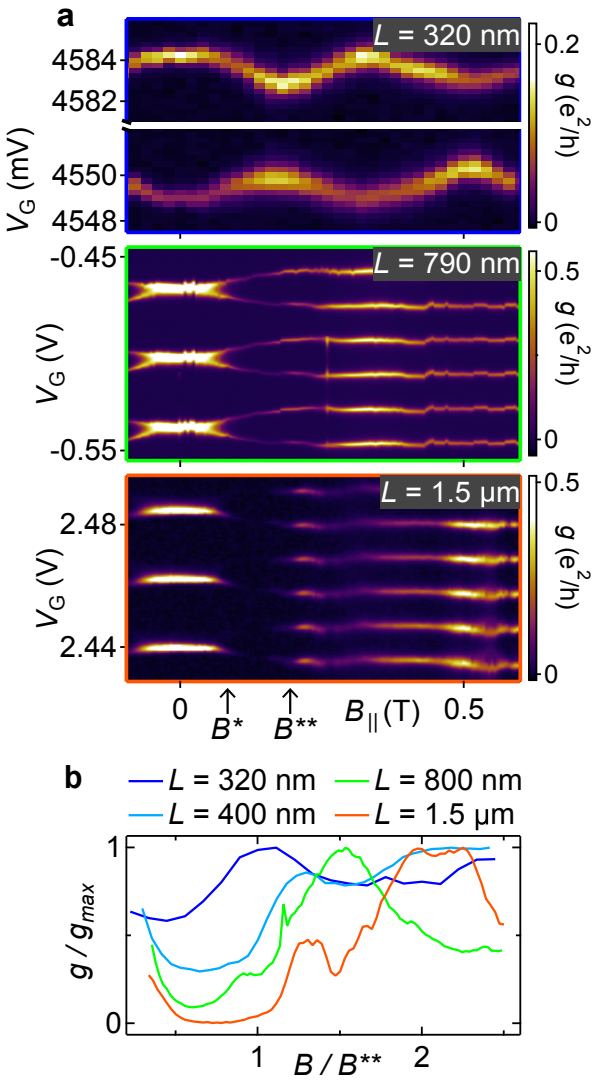

Figure 5.6: **a,** Conductance, g, as a function of gate voltage, V_{G} and magnetic field, $B_{||}$ in the weak-coupling regime for $L = 320\ \mathrm{nm}, 790\ \mathrm{nm}, 1.5\ \mu\mathrm{m}$. **b,** Normalized, average peak conductance, g/g_{max} versus normalized field, B/B^{**}. For $L = 1.5\ \mu\mathrm{m}$, peaks dim at B^{*} and brighten at B^{**}.

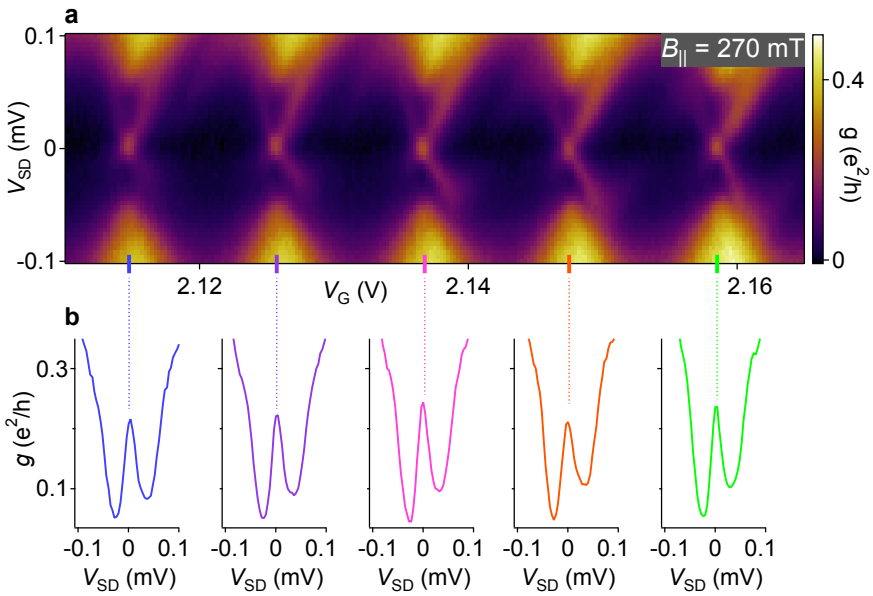

Figure 5.7: **a,** Conductance, g, versus source-drain bias voltage, V_{SD}, and gate voltage, V_G for $L = 1.5$ µm device. **b,** Conductance versus source-drain bias at the indicated diamond closing points.

All data presented so far in this chapter have been zero-bias, and therefore do not contain any information about excited states. In particular, for identifying Majorana modes, the presence of an excitation gap is a key feature. Coulomb diamonds in the 1e-periodic (Majorana) regime are shown for an $L = 1.5$ µm device in Fig. 5.7a. Conductance is gapped at the closing point of the Coulomb diamonds, indicating the presence of an excitation gap in the quantum dot. Bias spectroscopy at the diamond closing points, shown in Fig. 5.7b, reveals a repeatable Majorana zero-bias peak.

5.3 Discusion

This chapter reported a length study of Majorana islands composed of InAs nanowires with epitaxial Al half-shells, extending the study in Chapter 4 to long wire lengths. Oscillating energy splittings, measured using Coulomb peak spacings, are exponentially suppressed in wire length, with the characteristic Majorana coherence length $\xi = 250$ nm. This constitutes an explicit demonstration of exponential protection from external perturbations. Brightening of Coulomb peaks for longer devices suggests the presence of a robust, delocalized state connecting the leads, and provides the first experimental support for electron teleportation by Majorana fermions. Finally, Coulomb diamonds show that the zero-energy state is gapped.

6

Majorana fusion rules proposal

This chapter sketches a proposal for realizing Majorana-parity qubit initialization and readout that uses techniques similar to spin qubits (Chap.'s 3-2). This proposal, if implements, would also serve as a test of the robustness of Majorana modes, as discussed in Sec. 6.2. Many of the ideas in this proposal are already present in many places in the literatures, especially [185], which showed that charging energy is a resource for computation and [17] which discusses fusion rule demonstration. A full proposal is being prepared by, in addition to myself, David Aasen, Michael Hell, Ryan Mishmash, Jeroen Danon, Martin Leijnse, Jason Alicea, Thomas Jespersen, Joshua Folk, Karsten Flensberg, and Charles Marcus.

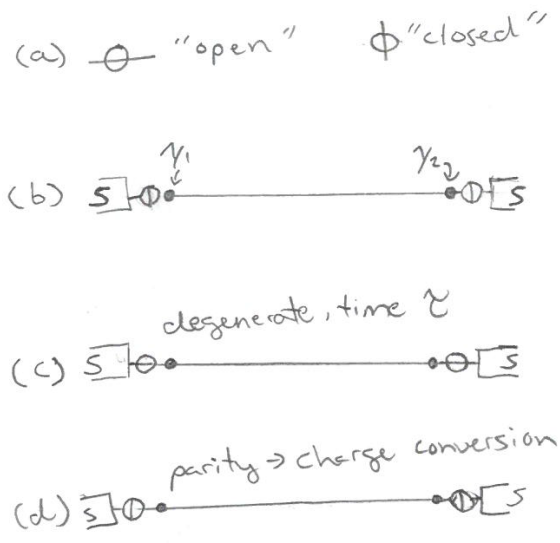

Figure 6.1: **a**, Diagrams for open (high-conductance) and closed (zero conductance) tunnel barriers. **b**, A dot with closed barriers and Majorana modes γ_1, γ_2. The parity eigenstates $|\pm\rangle_{12}$ are split by the charging energy. **c**, Adiabatically opening left and right barriers results in degenerate parity eigenstates. This configuration can be held for a time τ. **d**, Closing the tunnel barriers maps parity back onto charge, to be detected by a proximal sensor quantum dot.

6.1 Fusion rule setup

Imagine a superconductor/semiconductor nanowire with to Majorana modes at its ends. The two Majorana modes, γ_1 and γ_2, which obey the relations

$$\gamma_i = \gamma_i^\dagger, \tag{6.1}$$

$$\gamma_i\gamma_j + \gamma_j\gamma_i = 2\delta_{ij}, \tag{6.2}$$

together form a single regular fermion $c_{12} = \frac{1}{2}(\gamma_1 + i\gamma_2)$. In the presence of more than two Majoranas, the decision of which modes to pair into regular fermions is called choosing a basis. The regular-fermion parity is a well defined observable

$$\hat{P}_{12} = i\gamma_1\gamma_2 = 2\hat{n}_{12} - 1, \tag{6.3}$$

where $\hat{n}_{12} = c_{12}^\dagger c_{12}$ is the number operator. Parity, $\hat{P}_{12}$ can have eigenvalues ± 1, with eigenstates $|\pm\rangle_{12}$.

Imagine that the Majorana modes are present in a quantum dot, as potentially already realized in Chap. 5.

When the dot is isolated from the leads, it has a charging energy, which splits the parity eigenstates (Fig. 6.1a). For example, if the dot is tuned to the $n = 0$ charge state, the parity state $|-\rangle_{12}$ is the ground state, and $|+\rangle_{12}$ has energy of order E_C. The charging energy is quenched if the leads are set to unity transmission, making the parity states $|-\rangle_{12}$, $|+\rangle_{12}$ degenerate. In this open configuration it becomes important that the device has superconducting leads, so that parity is conserved even in the absence of charging energy.

The single dot geometry already allows for some interesting experiments, as outlined in Fig. 6.1. The Majorana modes can be initialized into a fixed parity state, made degenerate for a time τ, then mapped back onto charge for readout [see Fig. 6.1(a-d)]. The charge readout can be performed with a nearby sensor dot, similar to spin qubits (Chap. 3). Note that this parity readout mechanism is sensitive only to overall parity of the dot, but is insensitive "internal" poisoning events where a quasiparticle enters enters the continuum and another one flips the Majorana parity, which were discussed in Chap. 4. The entire pulse sequence constitutes a time-domain parity lifetime measurement of the Majorana parity qubit, and reminiscient of the prepare-separate-measure cycle for measuring T_2^* in Chap. 4

Moving to a double quantum dot would allow even more sophisticated experiments. Now there are four Majorana modes — γ_1, γ_2, γ_3, and γ_4 — to work with, where the two central modes, γ_2 and γ_3, are split in the presence of finite inter-dot tunneling. Charging energy can be used to couple γ_1 and γ_4 over long distance, while tunneling couples γ_2 and γ_3 locally.

The double dot geometry can be used to test Majorana fusion rules. Borrowing the first few steps from Fig. 6.1, we can initialized into an eigenstate of P_{14}, then open the leads to make $|\pm\rangle_{14}$ degenerate (Fig. 6.2a,b). Next, the central tunnel barrier is closed adiabatically, which initializes Majoranas γ_2 and γ_3 into one of the degenerate eigenstates $|\pm\rangle_{23}$ (Fig. 6.2c). The system is now initialized into an eigenstate of $\hat{P}_{14} \otimes \hat{P}_{23}$ (outer $\otimes$ inner). The left and right parities, $\hat{P}_{12}$ and $\hat{P}_{34}$, are then read out by closing tunnel barriers to the leads, as shown in Fig. 6.2d. The read out process can be considered a fusion of the left (γ_1,γ_2) and right (γ_3, γ_4). The Majorana fusion rule is that $\langle P_{12} \rangle = \langle P_{34} \rangle = 0$ with individual $\hat{P}_{12}$ and $\hat{P}_{34}$ eigenvalues perfectly anti-correlated.

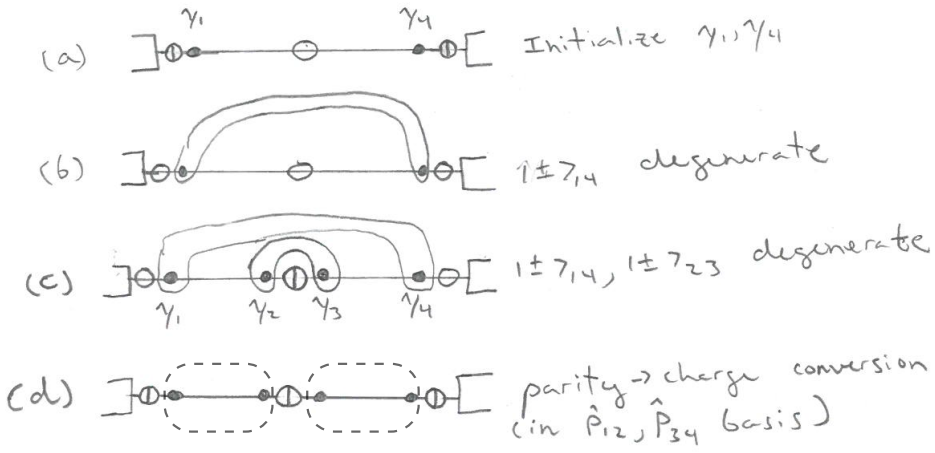

Figure 6.2: **a**, Left/right barriers closed with middle barrier open, initializing an eigenstate of P_{14}. **b**, Opening all barriers makes the parity eigenstates $|\pm\rangle_{14}$ degenerate. Central modes γ_2 and γ_3 are still split by tunnel coupling. **c**, Closing the central tunnel barriers results in four degenerate parity eigenstates, $|\pm\rangle_{14}$ and $|\pm\rangle_{23}$. Barrier should be closed adiabatically with respect to gap, but diabatically with respect to the exponentially small hybridization between γ_1 and γ_2. **d**,

6.2 Discussion

The fusion rule demonstration discussed above could serve as an experimental test of "how zero" the Majorana zero modes are. In the realistic case of some finite hybridization between γ_1 and γ_2, a truly adiabatic "separate" pulse, which generates the central Majoranas (Fig. 6.2b $\rightarrow$ c), would always initialize into an eigenstate of $\hat{P}_{12}$. For fusion rules, the separate pulse therefore needs to be diabatic with respect to the residual splitting between γ_1 and γ_2, which is exponentially small in theory. So far Majorana modes have only been identified in bias spectroscopy and addition energy, limited to energy resolution $\approx kT$. The fusion rule demonstration would be a zero-energy test with resolution h/t_{separate}, where t_{separate} can be of order the poisoning time. Putting in $t_{separate} \sim 1$ ms gives an anticipated energy resolution $h/t_{\text{separate}} = 10^{-8} \cdot k_{\text{b}}T$, eight orders of magnitude better than bias spectroscopy.

Even more progress can be made if a controlled coupling between γ_2 and γ_3 is possible. Then a parity gate, similar to the exchange gate implemented in Chap. 3 should be possible. One could initialize in the P_{12}, P_{34} basis (by waiting at Fig. 6.2d), then coherently rotate into a P_{14}, P_{23} eigenstate. Demonstrating coherent oscillations would show that the Majorana mode is a well-behaved qubit. Turning off all couplings part-way through the coherent rotation would constitute demonstration of a Majorana mode quantum memory.

Finally, its interesting to note that the sequence in Fig. 6.2 could be run in reverse, demonstrating initialization in the $\hat{P}_{12}$ and $\hat{P}_{34}$ eigenbasis, followed by readout of $\hat{P}_{14}$. A potential problem with the reverse sequence is that a quasiparticle generated from (γ_2, γ_3) fusion could poison the (γ_1, γ_4) system. Still, the reverse sequence would demonstrate the unusual property that two zero-energy fermionic states (c_{12}, c_{34}) always combine to form another zero-energy fermionic state (c_{14}), rather than "anticrossing" away from zero.

A

Thermodynamics of even-odd effect

This appendix gives a full derivation of the thermodynamic approach to the even-odd effect of Chapter 4, including the number of quasiparticles on the island. Section A.1 was led by Gediminas Kiršanskas and Karsten Flensberg, with small inputs from me.

A.1 General thermodynamics

The parity of the number of quasiparticles has to be equal to the parity of the number of electrons N on the island. The free energy difference δF between the odd and even occupation is expressed as [25, 165]

$$\delta F = F_{\mathrm{o}} - F_{\mathrm{e}} = -\frac{1}{\beta} \ln \left(\frac{Z_{\mathrm{o}}}{Z_{\mathrm{e}}} \right), \tag{A.1}$$

in terms of the partition functions for different parities

$$2Z_{\mathrm{o/e}} = \prod_{n,s} (1 + e^{-\beta E_n}) \mp \prod_{n,s} (1 - e^{-\beta E_n}). \tag{A.2}$$

where $\beta = 1/k_B T$ denotes the inverse temperature of the island. For a sufficiently large island the single particle spectrum can be described by the spectrum of a grounded superconductor where the single particle spectrum is $E_n = \sqrt{\varepsilon_n^2 + \Delta^2}$, for electron dispersion ε_n.

Without a subgap state the free energy difference Eq. (A.1) is expressed as

$$\delta F_{\mathrm{BCS}} = -k_B T \ln \tanh \left[\frac{1}{2} \sum_{n,s} \ln \coth \left(\frac{\beta E_n}{2} \right) \right] = -\frac{1}{\beta} \ln \tanh \int_{\Delta}^{+\infty} \mathrm{d}E \, \rho_{\mathrm{BCS}}(E) \ln \coth \left(\frac{\beta E}{2} \right), \quad \text{(A.3)}$$

where $\rho_{\mathrm{BCS}}(E)$ is the BCS density of states for quasiparticles on the island given by

$$\rho_{\mathrm{BCS}}(E) = \frac{\rho_{\mathrm{D}} E}{\sqrt{E^2 - \Delta^2}}, \quad \text{(A.4)}$$

with $\rho_{\mathrm{D}} = \rho_{\mathrm{Al}} V$ denoting the normal state density of states, including spin, and ρ_{Al} is aluminum density of states per volume, and V is the volume of the island. For small temperatures $\beta\Delta \gg 1$, the free energy difference (A.3) can be approximated as

$$\delta F_{\mathrm{BCS}} \approx -k_B T \ln \tanh \left[2 \int_{\Delta}^{+\infty} \mathrm{d}E \, \rho_{\mathrm{BCS}}(E) e^{-\beta E} \right] = -k_B T \ln \tanh \left[N_{\mathrm{eff}} e^{-\beta \Delta} \right] \approx \Delta - k_B T \ln(N_{\mathrm{eff}}), \quad \text{(A.5)}$$

where an effective number of quasiparticle states N_{eff} is given by

$$N_{\mathrm{eff}} = 2 \int_{\Delta}^{+\infty} \mathrm{d}E \, \rho_{\mathrm{BCS}}(E) e^{-\beta(E-\Delta)} = 2\rho_{\mathrm{D}} \Delta e^{\beta\Delta} K_1(\beta\Delta) \approx \rho_{\mathrm{D}} \sqrt{2\pi k_B T \Delta} \quad \text{(A.6)}$$

and $K_\nu(x)$ denotes the modified Bessel function of the second kind.

With a subgap state the free energy difference Eq. (A.1) acquires an additional term and one gets

$$\delta F_{\mathrm{ABS}} = -k_B T \ln \tanh \left[\int_{\Delta}^{+\infty} \mathrm{d}E \, \rho_{\mathrm{BCS}}(E) \ln \coth \left(\frac{\beta E}{2} \right) + \ln \coth(\beta E_0/2) \right]. \quad \text{(A.7)}$$

See also Eq. (B.1) where the approximate expression for the first term in used.

In Chapter 4 we discuss how the low-temperature data deviates from the above Andreev-bound-state model in terms of a life-time broadening of the subgap state. This is done by including a phenomenological

broadening with width γ into the subgap density of states, which then gives the free energy difference

$$\delta F_{\mathrm{ABS-LB}} = -k_{\mathrm{B}}T \ln \tanh \left[\int_{\Delta}^{+\infty} \mathrm{d}E\, \rho_{\mathrm{BCS}}(E) \ln \coth \left(\frac{\beta E}{2} \right) + \frac{1}{2} \sum_{\substack{\tau=\pm 1 \\ s=\uparrow,\downarrow}} \int_{0}^{+\infty} \frac{\mathrm{d}\omega}{2\pi} \frac{\gamma \ln \coth \left(\frac{\beta\omega}{2} \right)}{(\omega - \tau E_0)^2 + (\gamma/2)^2} \right]. \tag{A.8}$$

In the kinetic equation calculation presented below, the equilibrium distributions of quasiparticle in the continuum with an even or odd number of quasiparticles are needed. Since we will assume that the particles occupying the continuum are effectively equilibrated, we find the distribution functions by modifying the usual Fermi-Dirac distribution function as

$$f_P(E) = \frac{1}{e^{\beta E}(Z_P/Z_{\bar{P}}) + 1} \quad \rightarrow \quad \begin{cases} f_{\mathrm{e}}(E) = \dfrac{1}{e^{\beta(E+\delta F_{\mathrm{BCS}})} + 1}, \\ f_{\mathrm{o}}(E) = \dfrac{1}{e^{\beta(E-\delta F_{\mathrm{BCS}})} + 1}, \end{cases} \tag{A.9}$$

where $P \in \{\mathrm{e}, \mathrm{o}\}$, and $\bar{P}$ represents the opposite of P.

A.2 Number of quasiparticles

Using the above results, we derive a simple expression for the number of quasiparticles in the absence of a bound state. At low temperature, when $\delta F_{\mathrm{BCS}} = \Delta - k_{\mathrm{B}}T \ln(N_{\mathrm{eff}})$, the distribution functions take the form

$$f_{\mathrm{e}} = N_{\mathrm{eff}} e^{-\beta(E+\Delta)}, \tag{A.10}$$

$$f_{\mathrm{o}} = \frac{1}{N_{\mathrm{eff}}} e^{-\beta(E-\Delta)}, \tag{A.11}$$

where N_{eff} is given by Eq. (A.6).

The number of quasiparticles in each parity state can then be calculated using

$$N_P = 2 \int_{\Delta}^{+\infty} \mathrm{d}E\, \rho_{\mathrm{BCS}}(E) f_P(E). \tag{A.12}$$

Substituting the above expression for f_{o} gives $N_{\mathrm{o}} = 1$, as expected. Substituting f_{e} gives the quasiparticle

number

$$\begin{aligned} N_{\mathrm{e}} &= 2\int_{\Delta}^{+\infty} \mathrm{d}E\, \rho_{\mathrm{BCS}}(E) N_{\mathrm{eff}} e^{-\beta(E+\Delta)} \\ &= N_{\mathrm{eff}} e^{-2\beta\Delta} \int_{\Delta}^{+\infty} \mathrm{d}E\, 2\rho_{\mathrm{BCS}}(E) e^{-\beta(E-\Delta)} \\ &= \left(N_{\mathrm{eff}} e^{-\beta\Delta}\right)^2. \end{aligned} \tag{A.13}$$

Because of the large charging energy N_{e} is the square of the bulk value $N_{\mathrm{eff}}e^{-\beta\Delta}$, indicating that quasiparticles must be created in pairs.

Dividing the above expression for N_e by the Al volume, V_{Al}, gives the quasiparticle density

$$n_{\mathrm{qp}} = V_{\mathrm{Al}}^{-1} N_{\mathrm{eff}}^2 e^{-2\beta\Delta} \tag{A.14}$$

consistent with Chapter 4. It is worth noting that the formula for n_{qp} is volume dependent, ultimately a result of the fact that the derivation is performed in the large charging energy limit. In the bulk limit $E_C \to 0$, this equation would cease to be valid, with a crossover to the bulk result $N_{\mathrm{eff}}/Ve^{-\beta\Delta}$ when $E_C < kT$.

To understand the crossover, consider the full partition function as written by Lafarge [25]

$$Z = \sum_n e^{-\beta E_C (n-N_g)^2} Z_n, \tag{A.15}$$

where n denotes the charge on the island. For odd n, Z_n corresponds to the previously defined Z_o; likewise for even n it corresponds to Z_e. In the low temperature limit ($k_{\mathrm{B}}T \ll \Delta, E_C$) and for the gate voltage $N_g \in [-1/2, 1/2]$ being in the region of the even diamond $n = 0$, it is enough to take into account the odd particle states $n = \pm 1$. The single particle distribution function is given by

$$\begin{aligned} f(E) &\approx \frac{p_o e^{-\beta E} Z_e + p_e e^{-\beta E} Z_o}{p_o e^{-\beta E} Z_e + p_e e^{-\beta E} Z_o + p_e Z_e + p_o Z_o} \\ &= \frac{1 + p_o/p_e e^{\beta\delta F_{\mathrm{BCS}}}}{e^{\beta(E+\delta F_{\mathrm{BCS}})} + 1 + p_o/p_e (e^{\beta E} + e^{\beta\delta F_{\mathrm{BCS}}})} \\ &\approx N_{\mathrm{eff}} e^{-\beta(E+\Delta)} \left[1 - \left(\frac{p_o}{p_e}\right)^2\right] + \frac{p_o}{p_e} e^{-\beta E} \left[1 - \frac{p_o}{p_e} e^{-\beta E}\right], \\ &\text{with} \quad p_o = e^{-\beta(1-N_g)^2 E_C} + e^{-\beta(1+N_g)^2 E_C}, \quad p_e = e^{-\beta N_g^2}. \end{aligned} \tag{A.16}$$

Here we again used the low temperature limit ($k_B T \ll \Delta, E_C$) and $Z_e/Z_o = e^{\beta \delta F_{\rm BCS}} \approx e^{\beta\Delta}/N_{\rm eff}$. Using the above distribution (A.16) the total number of quasiparticles becomes

$$N_{\rm qp} = 2\int_{\Delta}^{+\infty} {\rm d}E\, \rho_{\rm BCS}(E) f(E) \approx N_{\rm eff}^2 e^{-2\beta\Delta}\left[1-\left(\frac{p_o}{p_e}\right)^2\right] + \frac{p_o}{p_e} N_{\rm eff} e^{-\beta\Delta}\left[1-\frac{p_o}{\sqrt{2}p_e}e^{-\beta\Delta}\right]. \tag{A.17}$$

The number of quasiparticles in the even Coulomb valley is then found by setting $N_g = 0$, which yields

$$N_{\rm e} = N_{\rm qp}(N_g = 0) \approx 2N_{\rm eff} e^{-\beta(\Delta+E_C)} + N_{\rm eff}^2 e^{-2\beta\Delta}. \tag{A.18}$$

For our system, which has $E_C > \Delta$, the first term is 10^{-22} times smaller than the second at $T = 200$mK, so

$$N_{\rm e} \approx N_{\rm eff}^2 e^{-2\beta\Delta} \tag{A.19}$$

is an excellent approximation, in agreement with Eq. (A.13). In the small charging energy limit, $E_C \ll k_B T$, from Eq. (A.15) one arrives at the bulk result $N_{\rm eff} e^{-\beta\Delta}$, as expected. It is important to note that the number of quasiparticles is gate, N_g, dependent. For example, at $N_g = 1/2$ there is effectively no charging energy and the bulk result is recovered.

To further emphasize that the $e^{-2\beta\Delta}$ result is generic for large E_C, we take the simple limit where there are N quasiparticle states at Δ. Then we can binomial expand $Z_e \approx 1 + N^2 e^{-2\beta\Delta}$ and $Z_o \approx N e^{-\beta\Delta}$. Substituting into Eq. (A.15), the overall partition function takes the intuitive form

$$Z = 1 + 2N e^{-\beta(\Delta+E_C)} + N^2 e^{-\beta(2\Delta)}. \tag{A.20}$$

The first term corresponds to zero quasiparticles, the second to one quasiparticle, and the third to two quasiparticles. The energy of single quasiparticles is $\Delta + E_C$, indicating that the total charge on the dot must change, whereas the energy of two quasiparticles is 2Δ, indicating that a Cooper pair can be broken at fixed total charge. In the limit $E_C > \Delta$, the single quasiparticle term is negligible, leaving only an $e^{-2\beta\Delta}$ term.

B

Approximations in Chapter 4

This appendix discusses various approximations made in the treatment of the even-odd effect of Chapter 4.

B.1 Comparison of free energy approximations

This section gives examples of the free energy difference, $F_o - F_e$, calculated under different approximations, considering the case without broadening $\gamma = 0$ and without an applied field $B = 0$. Under these conditions the free energy difference is given by Eq. (A.7). When $\beta\Delta > 1$ the approximation $\ln\coth(\beta E/2) \approx 2e^{-\beta E}$ can be used for the first term. Applying the identity $\int_\Delta^{+\infty} \mathrm{d}E\, \rho_{\mathrm{BCS}}(E) e^{-\beta E} = \rho_{\mathrm{Al}} V_{\mathrm{Al}} \Delta K_1(\beta\Delta)$ then gives

$$F_o - F_e \approx -k_B T \ln\tanh\left[2\rho_{\mathrm{Al}} V_{\mathrm{Al}} \Delta K_1(\beta\Delta) + \ln\coth\left(\frac{\beta E_0}{2}\right)\right], \tag{B.1}$$

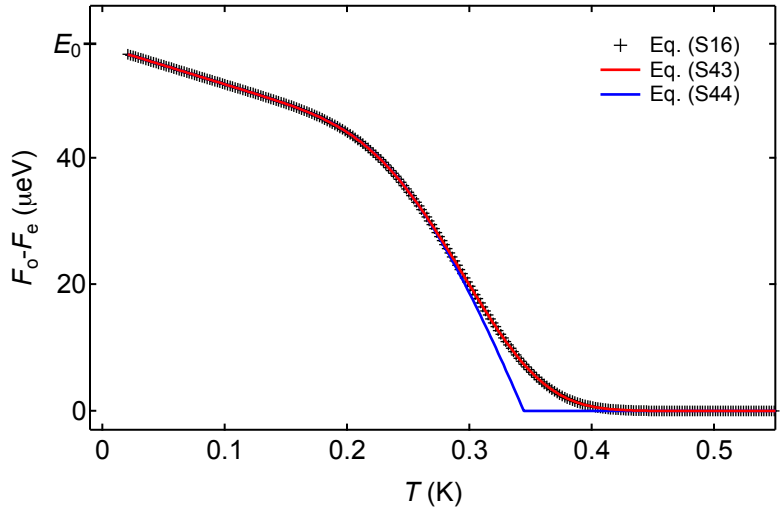

Figure B.1: Free energy difference $F_o - F_e$ versus temperature T for three different expressions for the free energy. All parameters same as Chapter 4 ($\Delta = 180\mu eV$, $E_0 = 58\mu eV$, $\gamma = 0$, $B = 0$). Black crosses are numerically exact values from Eq. (A.7), red line is Eq. (B.1), blue line is Eq. (B.2).

where $K_1(x)$ is a Bessel function of the second kind. In the very low temperature limit $\beta\Delta \gg 1$, $\beta E_0 > 1$ the approximations $K_1(\beta\Delta) \approx \sqrt{\pi/(2\beta\Delta)}e^{-\beta\Delta}$, $\ln\coth(\beta E_0/2) \approx 2e^{-\beta E_0}$, and $\tanh(x) \approx x$ can be used, giving

$$F_o - F_e \approx k_B T \ln\left[N_{eff}e^{-\beta\Delta} + 2e^{-\beta E_0}\right], \tag{B.2}$$

where $N_{eff} = \rho_{Al}V_{Al}\sqrt{2\pi k_B T\Delta}$.

Equations (B.1) and (B.2) constitute two levels of accuracy at which Eq. (A.7) can be evaluated. Figure S4 compares the methods. Equation (B.1) is an excellent approximation to Eq. (A.7) over the experimentally relevant temperature range. Equation (B.2) is poor approximation at intermediate temperatures.

B.2 Effect of the bound state on the free energy

Figure S5 shows a comparison of the free energy difference, $F_o - F$, with and without the subgap bound state. As the lowest energy unoccupied state, the bound state causes the free energy to saturate at $F_o - F_e = E_0$ at low temperature. It should be noted that the free energy difference with a subgap bound state was also shown in Fig. 5 of Lafarge et al.[25].

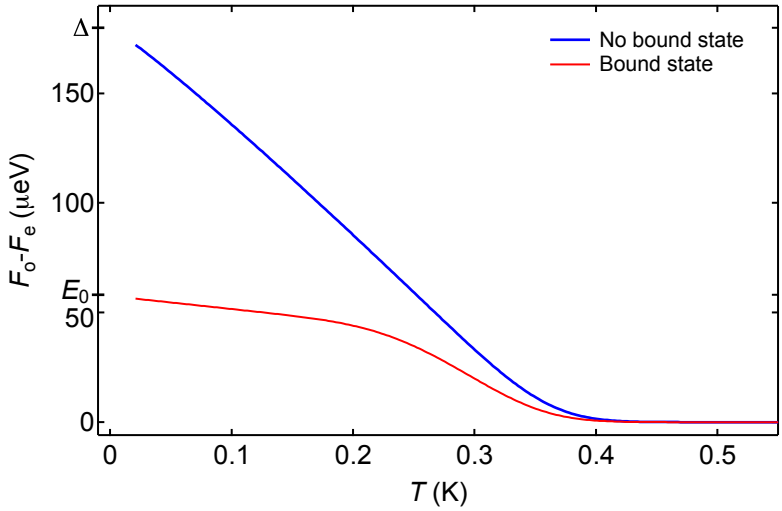

Figure B.2: Free energy difference $F_o - F_e$ versus temperature T with and without the semiconductor bound state. All parameters the same as Chapter 4 ($\Delta = 180\mu eV$, $E_0 = 58\mu eV$, $\gamma = 0$, $B = 0$). Blue trace includes the BCS density of states only, red trace includes the BCS density of states and the discrete state.

B.3 Comparison of thermodynamic and rate models

The thermodynamic and rate models can both be used to calculate Coulomb peak spacings. The thermodynamic model assumes equilibrium conditions, and hypothesizes that Coulomb peaks are at free energy degeneracies. The rate model takes into account thermodynamics, and also includes the differential bias used for conductance measurement. It is worth emphasizing that the rate model is fully consistent with thermodynamics; when used to calculate equilibrium quantities such as charge it exactly reproduces the thermodynamic results [167].

Figure. S7 shows the even-odd peak spacing data along with predictions of the thermodynamic and rate approaches. The rate model gives the better fit of the two with a slightly different best-fit Al volume, although the improvement is at a level comparable to experimental error. A theoretical description of the difference between these two models, physically related to differential versus direct measurements of the chemical potential, will be developed in future theoretical work.

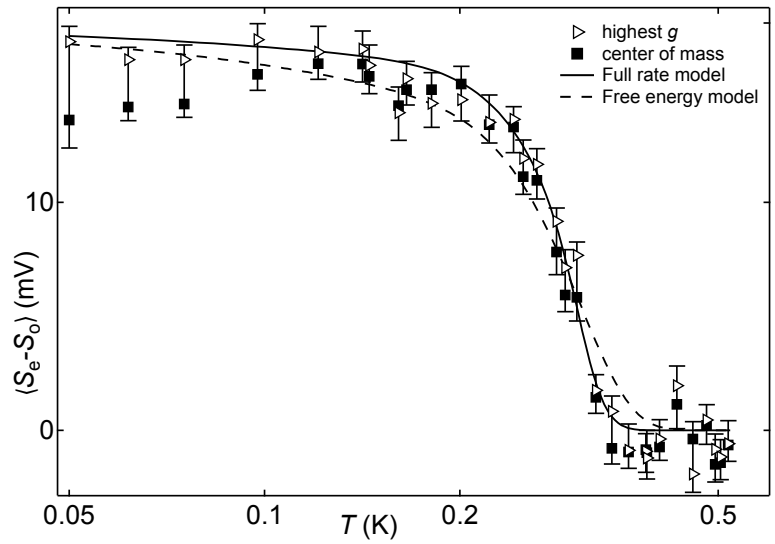

Figure B.3: Average even-odd spacing difference, $\langle S_e - S_o \rangle$, versus temperature, T. Spacing between peak maxima (triangle) and centroids (square) are shown. Solid curve is found by numerically solving Eq.'s (S38-S42) and finding peak maxima. Parameters are same as Chapter 4, except the fit Al volume $V_{Al} = 1.9 \times 10^5 \mathrm{nm}^3$. Dashed curve is thermodynamic model, Eq. (S16), identical to Fig. 4.1.

References

[1] L. P. Kouwenhoven, C. M. Marcus, P. L. McEuen, S. Tarucha, R. M. Westervelt, and N. S. Wingreen, in *Mesoscopic Electron Transport* (Springer Netherlands, Dordrecht, 1997) pp. 105–214.

[2] L. J. Klein, K. A. Slinker, J. L. Truitt, S. Goswami, K. L. M. Lewis, S. N. Coppersmith, D. W. van der Weide, M. Friesen, R. H. Blick, D. E. Savage, M. G. Lagally, C. Tahan, R. Joynt, M. A. Eriksson, J. O. Chu, J. A. Ott, and P. M. Mooney, Applied Physics Letters **84**, 4047 (2004).

[3] L. A. Ponomarenko, F. Schedin, M. I. Katsnelson, R. Yang, E. W. Hill, K. S. Novoselov, and A. K. Geim, Science **320**, 356 (2008).

[4] D. H. Cobden and J. Nygård, Physical Review Letters **89**, 046803 (2002).

[5] M. T. Björk, C. Thelander, A. E. Hansen, L. E. Jensen, M. W. Larsson, L. R. Wallenberg, and L. Samuelson, Nano Letters **4**, 1621 (2004).

[6] J. R. Petta, A. C. Johnson, J. M. Taylor, E. A. Laird, A. Yacoby, M. D. Lukin, C. M. Marcus, M. P. Hanson, and A. C. Gossard, Science **309**, 2180 (2005).

[7] F. H. L. Koppens, Science **309**, 1346 (2005).

[8] H. O. H. Churchill, F. Kuemmeth, J. W. Harlow, A. J. Bestwick, E. I. Rashba, K. Flensberg, C. H. Stwertka, T. Taychatanapat, S. K. Watson, and C. M. Marcus, Physical Review Letters **102**, 166802 (2009).

[9] S. Nadj-Perge, S. M. Frolov, E. P. A. M. Bakkers, and L. P. Kouwenhoven, Nature **468**, 1084 (2010).

[10] B. M. Maune, M. G. Borselli, B. Huang, T. D. Ladd, P. W. Deelman, K. S. Holabird, A. A. Kiselev, I. Alvarado-Rodriguez, R. S. Ross, A. E. Schmitz, M. Sokolich, C. A. Watson, M. F. Gyure, and A. T. Hunter, Nature **481**, 344 (2012).

[11] M. A. Nielsen and I. L. Chuang, *Quantum Computation and Quantum Information* (Cambridge University Press, 2010).

[12] A. G. Fowler, M. Mariantoni, J. M. Martinis, and A. N. Cleland, Physical Review A **86**, 032324 (2012).

[13] C. Nayak, S. H. Simon, A. Stern, M. Freedman, and S. Das Sarma, Reviews of Modern Physics **80**, 1083 (2008).

[14] F. Wilczek and A. Zee, Physical Review Letters **52**, 2111 (1984).

[15] R. M. Lutchyn, J. D. Sau, and S. Das Sarma, Physical Review Letters **105**, 077001 (2010).

[16] Y. Oreg, G. Refael, and F. von Oppen, Physical Review Letters **105**, 177002 (2010).

[17] J. Alicea, Y. Oreg, G. Refael, F. von Oppen, and M. P. A. Fisher, Nature Physics **7**, 412 (2011).

[18] V. Mourik, K. Zuo, S. M. Frolov, S. R. Plissard, E. P. A. M. Bakkers, and L. P. Kouwenhoven, Science **336**, 1003 (2012).

[19] M. Leijnse and K. Flensberg, arXiv.org (2012), 1206.1736v2 .

[20] F. L. Pedrocchi and D. P. Divincenzo, arXiv (2015), 1505.03712 .

[21] T. Ihn, *Semiconductor Nanostructures*, Quantum states and electronic transport (OUP Oxford, 2009).

[22] I. L. Aleiner, P. W. Brouwer, and L. I. Glazman, Physics Reports **358**, 309 (2002).

[23] S. R. Patel, S. M. Cronenwett, D. R. Stewart, A. G. Huibers, C. M. Marcus, C. I. Duruöz, J. S. Harris, Jr, K. Campman, and A. C. Gossard, Physical Review Letters **80**, 4522 (1998).

[24] J. A. Folk, S. R. Patel, S. F. Godijn, A. G. Huibers, S. M. Cronenwett, C. M. Marcus, K. Campman, and A. C. Gossard, Physical Review Letters **76**, 1699 (1996).

[25] P. Lafarge, P. Joyez, D. Esteve, C. Urbina, and M. H. Devoret, Physical Review Letters **70**, 994 (1993).

[26] S. Tarucha, D. G. Austing, T. Honda, R. J. van der Hage, and L. P. Kouwenhoven, Physical Review Letters **77**, 3613 (1996).

[27] A. P. Higginbotham, F. Kuemmeth, T. W. Larsen, M. Fitzpatrick, J. Yao, H. Yan, C. M. Lieber, and C. M. Marcus, Physical Review Letters **112**, 216806 (2014).

[28] S. Hikami, A. I. Larkin, and Y. Nagaoka, Progress of Theoretical Physics **63**, 707 (1980).

[29] G. Bergmann, Solid State Communications **42**, 815 (1982).

[30] G. Bergmann, Physics Reports **107**, 1 (1984).

[31] J. Moyle, J. Cheung, and N. Ong, Physical Review B **35**, 5639 (1987).

[32] P. Dresselhaus, C. Papavassiliou, R. Wheeler, and R. Sacks, Physical Review Letters **68**, 106 (1992).

[33] W. Knap, C. Skierbiszewski, A. Zduniak, E. Litwin-Staszewska, D. Bertho, F. Kobbi, J. Robert, G. Pikus, F. Pikus, S. Iordanskii, V. Mosser, K. Zekentes, and Y. Lyanda-Geller, Physical Review B **53**, 3912 (1996).

[34] R. L. Kallaher, J. J. Heremans, N. Goel, S. J. Chung, and M. B. Santos, Physical Review B **81**, 075303 (2010).

[35] H.-T. He, G. Wang, T. Zhang, I.-K. Sou, G. K. L. Wong, J.-N. Wang, H.-Z. Lu, S.-Q. Shen, and F.-C. Zhang, Physical Review Letters **106**, 166805 (2011).

[36] D. Loss and D. P. Divincenzo, Physical Review A **57**, 120 (1998).

[37] I. Žutić and S. Das Sarma, Reviews of Modern Physics **76**, 323 (2004).

[38] C. Beenakker and H. van Houten, Physical Review B **38**, 3232 (1988).

[39] Ç. Kurdak, A. Chang, A. Chin, and T. Chang, Physical Review B **46**, 6846 (1992).

[40] S. Kettemann, Physical Review Letters **98**, 176808 (2007).

[41] A. Hansen, M. Björk, C. Fasth, C. Thelander, and L. Samuelson, Physical Review B **71**, 205328 (2005).

[42] P. Lehnen, T. Schäpers, N. Kaluza, N. Thillosen, and H. Hardtdegen, Physical Review B **76**, 205307 (2007).

[43] S. Estévez Hernández, M. Akabori, K. Sladek, C. Volk, S. Alagha, H. Hardtdegen, M. G. Pala, N. Demarina, D. Grützmacher, and T. Schäpers, Physical Review B **82**, 235303 (2010).

[44] R. L. Kallaher, J. J. Heremans, N. Goel, S. J. Chung, and M. B. Santos, Physical Review B **81**, 035335 (2010).

[45] I. Aleiner and V. Fal'ko, Physical Review Letters **87**, 256801 (2001).

[46] Y. Ahmadian and I. L. Aleiner, Physical Review B **73**, 073312 (2006).

[47] D. M. Zumbühl, J. B. Miller, C. M. Marcus, K. Campman, and A. C. Gossard, Physical Review Letters **89**, 276803 (2002).

[48] B. Hackens, C. Gustin, V. Bayot, and M. Shayegan, Physica E: Low-dimensional Systems and Nanostructures **12**, 833 (2002).

[49] W. Lu, J. Xiang, B. P. Timko, Y. Wu, and C. M. Lieber, Proceedings of the National Academy of Sciences of the United States of America **102**, 10046 (2005).

[50] Y. Hu, H. O. H. Churchill, D. J. Reilly, J. Xiang, C. M. Lieber, and C. M. Marcus, Nature Nanotechnology **2**, 622 (2007).

[51] S. Roddaro, A. Fuhrer, P. Brusheim, C. Fasth, H. Q. Xu, L. Samuelson, J. Xiang, and C. M. Lieber, Physical Review Letters **101**, 186802 (2008).

[52] X.-J. Hao, T. Tu, G. Cao, C. Zhou, H.-O. Li, G.-C. Guo, W. Y. Fung, Z. Ji, G.-P. Guo, and W. Lu, Nano Letters **10**, 2956 (2010).

[53] C. Kloeffel, M. Trif, and D. Loss, Physical Review B **84**, 195314 (2011).

[54] K. B. Efetov, Adv. Phys. **32**, 53 (1983).

[55] R. A. Jalabert, A. D. Stone, and Y. Alhassid, Physical Review Letters;(United States) **68** (1992).

[56] A. M. Chang, H. U. Baranger, L. N. Pfeiffer, K. W. West, and T. Y. Chang, Phys. Rev. Lett. **76**, 1695 (1996).

[57] C. W. J. Beenakker, Physical Review B **44**, 1646 (1991).

[58] Y. Alhassid, M. Gökçedağ, and A. Stone, Physical Review B **58**, R7524 (1998).

[59] S. Patel, D. Stewart, C. Marcus, M. Gökçedağ, Y. Alhassid, A. Stone, C. Duruöz, and J. Harris, Physical Review Letters **81**, 5900 (1998).

[60] Y. Alhassid, Reviews of Modern Physics **72**, 895 (2000).

[61] F. Kuemmeth, K. I. Bolotin, S.-F. Shi, and D. C. Ralph, Nano Letters **8**, 4506 (2008).

[62] D. Wang, Q. Wang, A. Javey, R. Tu, H. Dai, H. Kim, P. C. McIntyre, T. Krishnamohan, and K. C. Saraswat, Applied Physics Letters **83**, 2432 (2003).

[63] Y. C. Cheng and E. A. Sullivan, Surface Science , 717 (1973).

[64] S. Mori and T. Ando, Physical Review B **19**, 6433 (1979).

[65] R. L. Kallaher, J. J. Heremans, N. Goel, S. J. Chung, and M. B. Santos, Physica E: Low-dimensional Systems and Nanostructures **42**, 971 (2010).

[66] R. B. Dingle, Proceedings of the Royal Society A: Mathematical, Physical and Engineering Sciences **201**, 545 (1950).

[67] A. P. Higginbotham, T. W. Larsen, J. Yao, H. Yan, C. M. Lieber, C. M. Marcus, and F. Kuemmeth, Nano Letters **14**, 3582 (2014).

[68] F. Koppens, C. Buizert, K.-J. Tielrooij, I. T. Vink, K. C. Nowack, T. Meunier, L. P. Kouwenhoven, and L. Vandersypen, Nature **442**, 766 (2006).

[69] R. Hanson, L. P. Kouwenhoven, J. R. Petta, S. Tarucha, and L. Vandersypen, Reviews of Modern Physics **79**, 1217 (2007).

[70] H. Bluhm, S. Foletti, I. Neder, M. Rudner, D. Mahalu, V. Umansky, and A. Yacoby, Nature Physics **7**, 109 (2011).

[71] J. Medford, Ł. Cywiński, C. Barthel, C. M. Marcus, M. P. Hanson, and A. C. Gossard, Physical Review Letters **108**, 086802 (2012).

[72] H. Bluhm, S. Foletti, D. Mahalu, V. Umansky, and A. Yacoby, Physical Review Letters **105**, 216803 (2010).

[73] H. O. H. Churchill, A. J. Bestwick, J. W. Harlow, F. Kuemmeth, D. Marcos, C. H. Stwertka, S. K. Watson, and C. M. Marcus, Nature Physics **5**, 321 (2009).

[74] F. Pei, E. A. Laird, G. A. Steele, and L. P. Kouwenhoven, Nature Nanotechnology **7**, 630 (2012).

[75] E. A. Laird, F. Pei, and L. P. Kouwenhoven, Nature Nanotechnology **8**, 565 (2013).

[76] S. Goswami, K. A. Slinker, M. Friesen, L. M. McGuire, J. L. Truitt, C. Tahan, L. J. Klein, J. O. Chu, P. M. Mooney, and D. W. Van Der Weide, Nature Physics **3**, 41 (2007).

[77] N. Shaji, C. B. Simmons, M. Thalakulam, L. J. Klein, H. Qin, H. Luo, D. E. Savage, M. G. Lagally, A. J. Rimberg, R. Joynt, M. Friesen, R. H. Blick, S. N. Coppersmith, and M. A. Eriksson, Nature Physics **4**, 540 (2008).

[78] Z. Shi, C. B. Simmons, D. R. Ward, J. R. Prance, X. Wu, T. S. Koh, J. K. Gamble, D. E. Savage, M. G. Lagally, and M. Friesen, Nature Communications **5**, 3020 (2014).

[79] J. J. Pla, K. Y. Tan, J. P. Dehollain, W. H. Lim, J. J. L. Morton, D. N. Jamieson, A. S. Dzurak, and A. Morello, Nature **489**, 541 (2012).

[80] J. J. Pla, K. Y. Tan, J. P. Dehollain, W. H. Lim, J. J. L. Morton, F. A. Zwanenburg, D. N. Jamieson, A. S. Dzurak, and A. Morello, Nature **496**, 334 (2013).

[81] J. P. Dehollain, J. T. Muhonen, K. Y. Tan, D. N. Jamieson, A. S. Dzurak, and A. Morello, arXiv.org (2014), 1402.7148v1 .

[82] J. T. Muhonen, J. P. Dehollain, A. Laucht, F. E. Hudson, T. Sekiguchi, K. M. Itoh, D. N. Jamieson, J. C. McCallum, A. S. Dzurak, and A. Morello, arXiv.org (2014), 1402.7140v1 .

[83] J. Xiang, W. Lu, Y. Hu, Y. Wu, H. Yan, and C. M. Lieber, Nature **441**, 489 (2006).

[84] H. Yan, H. S. Choe, S. Nam, Y. Hu, S. Das, J. F. Klemic, J. C. Ellenbogen, and C. M. Lieber, Nature **470**, 240 (2011).

[85] J. Yao, H. Yan, and C. M. Lieber, Nature Nanotechnology **8**, 329 (2013).

[86] J. Yao, H. Yan, S. Das, J. F. Klemic, J. C. Ellenbogen, and C. M. Lieber, Proceedings of the National Academy of Sciences of the United States of America , 201323818 (2014).

[87] K. C. Nowack, F. H. L. Koppens, Y. V. Nazarov, and L. M. K. Vandersypen, Science **318**, 1430 (2007).

[88] K. C. Nowack, M. Shafiei, M. Laforest, G. E. D. K. Prawiroatmodjo, L. R. Schreiber, C. Reichl, W. Wegscheider, and L. M. K. Vandersypen, Science **333**, 1269 (2011).

[89] J. W. G. van den Berg, S. Nadj-Perge, V. S. Pribiag, S. R. Plissard, E. P. A. M. Bakkers, S. M. Frolov, and L. P. Kouwenhoven, Physical Review Letters **110**, 066806 (2013).

[90] J. Fischer, W. A. Coish, D. V. Bulaev, and D. Loss, Physical Review B **78**, 155329 (2008).

[91] V. S. Pribiag, S. Nadj-Perge, S. M. Frolov, J. W. G. van den Berg, I. van Weperen, S. R. Plissard, E. P. A. M. Bakkers, and L. P. Kouwenhoven, Nature Nanotechnology **8**, 170 (2013).

[92] C. Kloeffel, M. Trif, P. Stano, and D. Loss, Physical Review B **88**, 241405 (2013).

[93] C. Barthel, D. J. Reilly, C. M. Marcus, M. P. Hanson, and A. C. Gossard, Physical Review Letters **103**, 160503 (2009).

[94] J. Medford, J. Beil, J. M. Taylor, S. D. Bartlett, A. C. Doherty, E. I. Rashba, D. P. DiVincenzo, H. Lu, A. C. Gossard, and C. M. Marcus, Nature Nanotechnology **8**, 654 (2013).

[95] E. Clementi and D. L. Raimondi, The Journal of Chemical Physics **38**, 2686 (1963).

[96] E. A. Chekhovich, Krysa, AB, M. S. Skolnick, and A. I. Tartakovskii, Physical Review Letters **106**, 027402 (2011).

[97] Y. Hu, F. Kuemmeth, C. M. Lieber, and C. M. Marcus, Nature Nanotechnology **7**, 47 (2012).

[98] K. D. Petersson, C. G. Smith, D. Anderson, P. Atkinson, G. Jones, and D. A. Ritchie, Nano Letters **10**, 2789 (2010).

[99] M. Jung, M. D. Schroer, K. D. Petersson, and J. R. Petta, Applied Physics Letters **100**, 253508 (2012).

[100] W. van der Wiel, S. De Franceschi, J. Elzerman, T. Fujisawa, S. Tarucha, and L. Kouwenhoven, Reviews of Modern Physics **75**, 1 (2002).

[101] A. P. Higginbotham, F. Kuemmeth, M. P. Hanson, A. C. Gossard, and C. M. Marcus, Physical Review Letters **112**, 026801 (2014).

[102] S. Vorojtsov, E. R. Mucciolo, and H. U. Baranger, Physical Review B **69**, 115329 (2004).

[103] A. C. Johnson, J. R. Petta, C. M. Marcus, M. P. Hanson, and A. C. Gossard, Physical Review B **72**, 165308 (2005).

[104] J. Danon and Y. V. Nazarov, Physical Review B **80**, 041301 (2009).

[105] A. C. Johnson, J. R. Petta, J. M. Taylor, A. Yacoby, M. D. Lukin, C. M. Marcus, M. P. Hanson, and A. C. Gossard, Nature **435**, 925 (2005).

[106] K. D. Petersson, L. W. McFaul, M. D. Schroer, M. Jung, J. M. Taylor, A. A. Houck, and J. R. Petta, Nature **490**, 380 (2012).

[107] F. Maier, C. Kloeffel, and D. Loss, Physical Review B **87**, 161305 (2013).

[108] W. A. Coish and D. Loss, Physical Review B **72**, 125337 (2005).

[109] Ł. Cywiński, R. Lutchyn, C. Nave, and S. Das Sarma, Physical Review B 77, 174509 (2008).

[110] F. Beaudoin and W. A. Coish, Physical Review B **88**, 085320 (2013).

[111] P. Huang and X. Hu, arXiv.org (2013), 1308.0352v2 .

[112] K. Schulten and P. G. Wolynes, The Journal of Chemical Physics **68**, 3292 (1978).

[113] I. A. Merkulov, A. L. Efros, and M. Rosen, Physical Review B **65**, 205309 (2002).

[114] W. Zhang, V. V. Dobrovitski, K. A. Al-Hassanieh, E. Dagotto, and B. N. Harmon, Physical Review B **74**, 205313 (2006).

[115] L. Trifunovic, O. Dial, M. Trif, J. R. Wootton, R. Abebe, A. Yacoby, and D. Loss, Physical Review X **2**, 011006 (2012).

[116] M. D. Shulman, O. E. Dial, S. P. Harvey, H. Bluhm, V. Umansky, and A. Yacoby, Science **336**, 202 (2012).

[117] E. A. Laird, F. Pei, and L. P. Kouwenhoven, Nature Nanotechnology Advanced Online Publication (2013).

[118] P. Brouwer, Y. Oreg, and B. Halperin, Physical Review B **60**, R13977 (1999).

[119] X. Hu and S. Das Sarma, Physical Review A **64**, 042312 (2001).

[120] S. Amaha, T. Kodera, T. Hatano, K. Ono, Y. Tokura, S. Tarucha, J. A. Gupta, and D. G. Austing, Journal of the Physical Society of Japan **80**, 023701 (2011).

[121] M. Buitelaar, J. Fransson, A. Cantone, C. Smith, D. Anderson, G. Jones, A. Ardavan, A. Khlobystov, A. Watt, K. Porfyrakis, and G. Briggs, Physical Review B 77, 245439 (2008).

[122] G. Yamahata, T. Kodera, H. Churchill, K. Uchida, C. Marcus, and S. Oda, Physical Review B **86**, 115322 (2012).

[123] D. J. Reilly, J. M. Taylor, E. A. Laird, J. R. Petta, C. M. Marcus, M. P. Hanson, and A. C. Gossard, Physical Review Letters **101**, 236803 (2008).

[124] K. D. Petersson, J. R. Petta, H. Lu, and A. C. Gossard, Physical Review Letters **105**, 246804 (2010).

[125] O. E. Dial, M. D. Shulman, S. P. Harvey, H. Bluhm, V. Umansky, and A. Yacoby, Physical Review Letters **110**, 146804 (2013).

[126] E. Barnes, J. Kestner, N. T. Nguyen, and S. Das Sarma, Physical Review B **84**, 235309 (2011).

[127] E. Nielsen, E. Barnes, J. P. Kestner, and S. D. Sarma, arXiv.org (2013).

[128] S. Mehl and D. P. Divincenzo, arXiv.org (2013), 1305.0749v1 .

[129] J.-T. Hung, Ł. Cywiński, X. Hu, and S. Das Sarma, Physical Review B **88**, 085314 (2013).

[130] C. Barthel, M. Kjærgaard, J. Medford, M. Stopa, C. M. Marcus, M. P. Hanson, and A. C. Gossard, Physical Review B **81**, 161308 (2010).

[131] D. J. Reilly, C. M. Marcus, M. P. Hanson, and A. C. Gossard, Applied Physics Letters **91**, 162101 (2007).

[132] A. P. Higginbotham, S. M. Albrecht, G. Kirsanskas, W. Chang, F. Kuemmeth, P. Krogstrup, T. S. Jespersen, J. Nygård, K. Flensberg, and C. M. Marcus, arXiv.org , 1501.05155 (2015).

[133] K. M. Lang, S. Nam, J. Aumentado, C. Urbina, and J. M. Martinis, Applied Superconductivity, IEEE Transactions on **13**, 989 (2003).

[134] J. Aumentado, M. W. Keller, J. M. Martinis, and M. H. Devoret, Physical Review Letters **92**, 066802 (2004).

[135] J. M. Martinis, M. Ansmann, and J. Aumentado, Physical Review Letters **103**, 097002 (2009).

[136] P. J. De Visser, J. J. A. Baselmans, P. Diener, S. J. C. Yates, A. Endo, and T. M. Klapwijk, Physical Review Letters **106** (2011).

[137] O. P. Saira, A. Kemppinen, V. F. Maisi, and J. P. Pekola, Physical Review B **85**, 012504 (2012).

[138] I. M. Pop, K. Geerlings, G. Catelani, R. J. Schoelkopf, L. I. Glazman, and M. H. Devoret, Nature **508**, 369 (2014).

[139] M. Leijnse and K. Flensberg, Physical Review B **84**, 140501 (2011).

[140] D. Rainis and D. Loss, Physical Review B **85**, 174533 (2012).

[141] M. Cheng, R. M. Lutchyn, and S. Das Sarma, Physical Review B **85**, 165124 (2012).

[142] A. Ferguson, N. Court, F. Hudson, and R. Clark, Physical Review Letters **97**, 106603 (2006).

[143] M. Zgirski, L. Bretheau, Q. Le Masne, H. Pothier, D. Esteve, and C. Urbina, Physical Review Letters **106**, 257003 (2011).

[144] L. Sun, L. DiCarlo, M. D. Reed, G. Catelani, L. S. Bishop, D. I. Schuster, B. R. Johnson, G. A. Yang, L. Frunzio, L. Glazman, M. H. Devoret, and R. J. Schoelkopf, Physical Review Letters **108**, 230509 (2012).

[145] D. Ristè, C. C. Bultink, M. J. Tiggelman, R. N. Schouten, K. W. Lehnert, and L. DiCarlo, Nature Communications **4**, 1913 (2013).

[146] V. F. Maisi, S. V. Lotkhov, A. Kemppinen, A. Heimes, J. T. Muhonen, and J. P. Pekola, Physical Review Letters **111**, 147001 (2013).

[147] Y. J. Doh, J. A. van Dam, A. L. Roest, E. Bakkers, L. P. Kouwenhoven, and S. De Franceschi, Science **309**, 272 (2005).

[148] L. Hofstetter, S. Csonka, J. Nygård, and C. Schönenberger, Nature **461**, 960 (2009).

[149] J.-D. Pillet, C. H. L. Quay, P. Morfin, C. Bena, A. L. Yeyati, and P. Joyez, Nature Physics **6**, 965 (2010).

[150] S. De Franceschi, L. Kouwenhoven, C. Schoenenberger, and W. Wernsdorfer, Nature Nanotechnology **5**, 703 (2010).

[151] F. Giazotto, P. Spathis, S. Roddaro, S. Biswas, F. Taddei, M. Governale, and L. Sorba, Nature Physics **7**, 857 (2011).

[152] J. D. Sau, R. M. Lutchyn, S. Tewari, and S. Das Sarma, Physical Review Letters **104**, 040502 (2010).

[153] C. Padurariu and Y. V. Nazarov, Physical Review B **81**, 144519 (2010).

[154] M. Leijnse and K. Flensberg, Physical Review Letters **111**, 060501 (2013).

[155] A. Das, Y. Ronen, Y. Most, Y. Oreg, M. Heiblum, and H. Shtrikman, Nature Physics **8**, 887 (2012).

[156] R. S. Deacon, Y. Tanaka, A. Oiwa, R. Sakano, K. Yoshida, K. Shibata, K. Hirakawa, and S. Tarucha, Physical Review Letters **104**, 076805 (2010).

[157] E. J. H. Lee, X. Jiang, R. Aguado, G. Katsaros, C. M. Lieber, and S. De Franceschi, Physical Review Letters **109**, 186802 (2012).

[158] E. J. H. Lee, X. Jiang, M. Houzet, R. Aguado, C. M. Lieber, and S. De Franceschi, Nature Nanotechnology **9**, 79 (2014).

[159] W. Chang, V. E. Manucharyan, T. S. Jespersen, J. Nygård, and C. M. Marcus, Physical Review Letters **110**, 217005 (2013).

[160] J. D. Sau and S. Das Sarma, Nature Communications **3**, 964 (2012).

[161] M. Leijnse and K. Flensberg, Physical Review B **86**, 134528 (2012).

[162] I. C. Fulga, A. Haim, A. R. Akhmerov, and Y. Oreg, New Journal of Physics **15**, 045020 (2013).

[163] L. Fu, Physical Review Letters **104**, 056402 (2010).

[164] R. Hützen, A. Zazunov, B. Braunecker, A. L. Yeyati, and R. Egger, Physical Review Letters **109**, 166403 (2012).

[165] M. T. Tuominen, J. M. Hergenrother, T. S. Tighe, and M. Tinkham, Physical Review Letters **69**, 1997 (1992).

[166] D. V. Averin and Y. V. Nazarov, Physical Review Letters **69**, 1993 (1992).

[167] M. Tinkham, *Introduction to Superconductivity; 2nd ed.*, Dover books on physics (Dover, Mineola, NY, 2004).

[168] F. W. J. Hekking, L. I. Glazman, K. A. Matveev, and R. I. Shekhter, Physical Review Letters **70**, 4138 (1993).

[169] J. M. Hergenrother, M. T. Tuominen, and M. Tinkham, Physical Review Letters **72**, 1742 (1994).

[170] M. T. Björk, A. Fuhrer, A. Hansen, M. Larsson, L. Fröberg, and L. Samuelson, Physical Review B **72**, 201307 (2005).

[171] S. Csonka, L. Hofstetter, F. Freitag, S. Oberholzer, C. Schönenberger, T. S. Jespersen, M. Aagesen, and J. Nygård, Nano Letters **8**, 3932 (2008).

[172] K. A. Matveev, L. I. Glazman, and R. I. Shekhter, Modern Physics Letters **08**, 1007 (1994).

[173] D. G. Olivares, A. L. Yeyati, L. Bretheau, Ç. Ö. Girit, H. Pothier, and C. Urbina, Physical Review B **89**, 104504 (2014).

[174] A. Zazunov, A. Brunetti, A. L. Yeyati, and R. Egger, Physical Review B **90**, 104508 (2014).

[175] M. Freedman, A. Kitaev, M. Larsen, and Z. Wang, Bulletin of the American Mathematical Society **40**, 31 (2003).

[176] A. Y. Kitaev, Phys.Usp. **44**, 131 (2001).

[177] R. M. Lutchyn, J. D. Sau, and S. Das Sarma, Physical Review Letters **105** (2010).

[178] L. P. Rokhinson, X. Liu, and J. K. Furdyna, Nature Physics **8**, 795 (2012).

[179] M. T. Deng, C. L. Yu, G. Y. Huang, M. Larsson, P. Caroff, and H. Q. Xu, Nano Letters **12**, 6414 (2012).

[180] H. O. H. Churchill, V. Fatemi, K. Grove-Rasmussen, M. T. Deng, P. Caroff, H. Q. Xu, and C. M. Marcus, Physical Review B **87**, 241401 (2013).

[181] S. Nadj-Perge, I. K. Drozdov, J. Li, H. Chen, S. Jeon, J. Seo, A. H. MacDonald, B. A. Bernevig, and A. Yazdani, Science **346**, 602 (2014).

[182] S. Das Sarma, J. D. Sau, and T. D. Stanescu, Physical Review B **86**, 220506 (2012).

[183] T. Stanescu, R. Lutchyn, and S. Das Sarma, Physical Review B **87**, 094518 (2013).

[184] J. D. Sau, B. Swingle, and S. Tewari, arXiv.org **cond-mat.mes-hall** (2012).

[185] B. van Heck, A. R. Akhmerov, F. Hassler, M. Burrello, and C. W. J. Beenakker, New Journal of Physics **14** (2012)